POLYPUBLIE
Polytechnique Montréal

POLYTECHNIQUE MONTRÉAL
UNIVERSITÉ D'INGÉNIERIE

Titre: Title:	Wide-Field Fluorescence Hyperspectral Imaging to Quantify Cell Populations in Spheroids Formed and Cultured in Microfluidic Chips
Auteur: Author:	Amélie St-Georges-Robillard
Date:	2018
Type:	Mémoire ou thèse / Dissertation or Thesis
Référence: Citation:	St-Georges-Robillard, A. (2018). Wide-Field Fluorescence Hyperspectral Imaging to Quantify Cell Populations in Spheroids Formed and Cultured in Microfluidic Chips [Ph.D. thesis, École Polytechnique de Montréal]. PolyPublie. https://publications.polymtl.ca/3741/

Document en libre accès dans PolyPublie
Open Access document in PolyPublie

URL de PolyPublie: PolyPublie URL:	https://publications.polymtl.ca/3741/
Directeurs de recherche: Advisors:	Thomas Gervais, & Frédéric Leblond
Programme: Program:	Génie biomédical

UNIVERSITÉ DE MONTRÉAL

WIDE-FIELD FLUORESCENCE HYPERSPECTRAL IMAGING TO QUANTIFY CELL POPULATIONS IN SPHEROIDS FORMED AND CULTURED IN MICROFLUIDIC CHIPS

AMÉLIE ST-GEORGES-ROBILLARD

INSTITUT DE GÉNIE BIOMÉDICAL

ÉCOLE POLYTECHNIQUE DE MONTRÉAL

THÈSE PRÉSENTÉE EN VUE DE L'OBTENTION

DU DIPLÔME DE PHILOSOPHIAE DOCTOR

(GÉNIE BIOMÉDICAL)

NOVEMBRE 2018

UNIVERSITÉ DE MONTRÉAL

ÉCOLE POLYTECHNIQUE DE MONTRÉAL

Cette thèse intitulée:

WIDE-FIELD FLUORESCENCE HYPERSPECTRAL IMAGING TO QUANTIFY CELL POPULATIONS IN SPHEROIDS FORMED AND CULTURED IN MICROFLUIDIC CHIPS

présentée par : ST-GEORGES-ROBILLARD Amélie

en vue de l'obtention du diplôme de : Philosophiae Doctor

a été dûment acceptée par le jury d'examen constitué de :

Mme BOUDOUX Caroline, Ph. D, présidente

M. GERVAIS Thomas, Ph. D, membre et directeur de recherche

M. LEBLOND Frédéric, Ph. D, membre et codirecteur de recherche

M. LAVERTU Marc, Ph. D, membre

M. MORAES Christopher, Ph. D, membre externe

ACKNOWLEDGEMENTS

I would also like to thank all my friends for believing in me. Kathy, you made me cry during your Ph.D. defence, so it's your turn now! Thank you so much for being my best friend for the past decade (!). Your achievements throughout the years inspire me every day to push myself. Talking with about everything and anything, serious or fun, immensely helped me throughout the years and especially now. You are the best confidant. Laurent, Alex, Karine, JP, Sunny, Dany, Pat, FM, Jess, Aubin, and all the Ahuntsic crew, thanks for keeping me sane outside of work. Boardgames and camping with all of you is the best.

A very special thank you to my parents and my family. I would not be here with you. Thanks for enthusiastically trying to explain my project to everyone you know, your support means a lot to me!

Finally, Benoît, your unwavering support during the last 12 years has been vital to me. I cannot thank you enough. You challenge me in every aspect (did I really try mountain biking?). Having you by my side always reassures me and I cannot wait to discover what the future holds for us!

RÉSUMÉ

Le cancer de l'ovaire a le taux de mortalité le plus élevé de tous les cancers gynécologiques. Malgré les avancements en techniques de chirurgie et les développements en chimiothérapie au cours de la dernière décennie, son taux de survie après cinq ans demeure inférieur à 45%, en raison du diagnostic tardif de ce cancer et du phénomène de résistance aux médicaments. Les patients présentant un cancer épithélial de l'ovaire (CÉO), la forme la plus courante de la maladie, répondent généralement bien au traitement de chimiothérapie standard à base de platine et de taxane. Cependant, une forte proportion de patients rechute et cette récurrence se révèle souvent résistante au traitement standard. Une des hypothèses de cette résistance chez le CÉO est que son instabilité génétique élevée se traduit par une hétérogénéité clonale dans les tumeurs, où le nombre de clones (populations de cellules identiques) dans les tumeurs augmente avec le temps, créant de nouvelles mutations présentant différents niveaux de sensibilité aux traitements. Par exemple, le premier traitement de chimiothérapie d'une patiente peut tuer les clones sensibles et laisser une faible population de cellules résistantes qui finiront par croître et provoquer une rechute du cancer. Il est donc nécessaire d'étudier l'hétérogénéité clonale et ses effets sur la résistance aux médicaments.

Divers modèles de cancer *in vitro* ont été développés pour la recherche en laboratoire. Le modèle le plus simple et le plus courant est la culture en monocouches bi-dimensionnelles (2D), pour laquelle les cellules cancéreuses adhèrent à une surface, comme les boîtes de pétri, et croissent en monocouche. Le modèle le plus réaliste consiste à utiliser directement les tumeurs de patients, car elles incluent le microenvironnement complet du cancer en trois dimensions (3D). Cependant, comme le tissu du patient est souvent disponible en quantités limitées, le nombre d'expériences qu'il est possible de faire est aussi limité. Les sphéroïdes sont des agrégats de cellules 3D formés *in vitro* et représentent un compromis idéal entre la simplicité, leur composition cellulaire étant connue et contrôlée, et le réalisme, car ils imitent mieux la nature 3D des tumeurs humaines que la culture en monocouches 2D. Les sphéroïdes peuvent facilement être utilisés pour étudier l'hétérogénéité clonale car plusieurs lignées cellulaires peuvent être mélangées à des ratios précis pour former des sphéroïdes de coculture.

La communauté microfluidique a mis au point des puces microfluidiques qui peuvent facilement former et traiter des centaines de sphéroïdes. Dans ce projet, les puces microfluidiques sont utilisées pour réduire le travail en laboratoire en formant des dizaines de sphéroïdes en une seule étape et

en les piégeant en place, de sorte que les changements de milieu de culture et de médicaments peuvent être rapidement effectués.

L'un des principaux avantages de l'utilisation de sphéroïdes comme modèle de cancer *in vitro* est que des centaines de sphéroïdes de coculture identiques peuvent être utilisés pour étudier facilement diverses conditions. Cependant, l'analyse de la réponse dynamique de chacune des populations de cellules composant ce grand nombre de sphéroïdes reste un défi. Les études utilisent souvent la morphologie cellulaire, les marqueurs immunologiques ou les marqueurs fluorescents pour identifier les populations cellulaires. Mais beaucoup de ces techniques reposent sur l'observation directe de chaque cellule composant le sphéroïde et nécessitent soit une digestion du sphéroïde en une suspension cellulaire, soit une coupe du sphéroïde en fines tranches. Pour analyser des échantillons 3D intacts, des techniques de microscopie telles que la microscopie confocale, multiphotonique et à feuilles de lumière (*light sheet microscopy*) ont été développées. Bien qu'elles présentent de nombreux avantages, ces techniques ne sont pas adaptées pour analyser un haut nombre de sphéroïdes en une seule acquisition ou ne peuvent pas analyser les sphéroïdes de diamètres supérieurs à 70-100 µm.

Au cours de ce doctorat, un système d'imagerie hyperspectrale (HSI) en fluorescence à large champ a été conçu, construit et validé pour l'étude de sphéroïdes en coculture. Le système HSI a été spécifiquement conçu pour imager plusieurs sphéroïdes en une seule acquisition et pour l'imagerie *in situ* de sphéroïdes dans des puces microfluidiques. La conception du système HSI, présentée dans l'article 1, repose sur l'utilisation d'un filtre accordable à cristaux liquides et d'une caméra à dispositif à transfert de charges à multiplication d'électrons (EMCCD) pour l'imagerie des sphéroïdes dans un champ de vision de 7,25 mm de diamètre. Un algorithme d'analyse d'image a également été développé pour compenser toute réponse du système influençant l'intensité de fluorescence mesurée pour chaque sphéroïde présent dans l'image. Une étape finale de quantification pour compenser les propriétés optiques de l'échantillon a également été développée et validée à l'aide de fantômes optiques.

L'article 2 présente une méthodologie pour étudier l'hétérogénéité clonale et sa relation avec la réponse au traitement. Deux lignées cellulaires fluorescentes ont été dérivées de la même lignée cellulaire du cancer de l'ovaire et ont été utilisées pour former des sphéroïdes de coculture avec différents ratios d'ensemencement cellulaire initiaux. Les résultats montrent que le système HSI

permet de suivre la croissance de chaque population cellulaire et sa réponse aux médicaments en fonction du temps, y compris pour les populations occupant seulement 10% des sphéroïdes. L'accaparement d'un clone par rapport à l'autre dans les sphéroïdes a également été observé lorsqu'une forte dose de chimiothérapie était utilisée pour traiter les sphéroïdes. Le système HSI a également pu mettre en évidence différentes dynamiques de réponse au médicament entre les deux populations de cellules.

L'imagerie hyperspectrale en fluorescence à champ large est une technique idéale pour l'imagerie de plusieurs sphéroïdes en une seule acquisition. Sa résolution spectrale permet de quantifier un plus grand nombre de fluorophores que les cubes de filtres de microscopie standards. L'imagerie hyperspectrale pourrait également être utilisée pour étudier les sphéroïdes de coculture constitués de différents types de cellules, tels que les cellules épithéliales et stromales ou les cellules cancéreuses et immunitaires.

ABSTRACT

Ovarian cancer has the highest mortality rate of all gynecological cancers. Despite advancement in surgery and chemotherapy over the past decade, its five-year survival rate is still less than 45%, due to late diagnosis and drug resistance. Patients presenting epithelial ovarian cancer (EOC), the most common form of the disease, usually respond well to the standard platinum- and taxane-based chemotherapy treatment. However, a high proportion of patient relapses, and this recurring cancer is often found to be resistant to the standard treatment. One hypothesis for this drug resistance in EOC is that its known high genetic instability translates into clonal heterogeneity in tumours, where the number of clones (i.e. populations of identical cells) in tumours increases over time as new mutations create new clones of various drug sensitivity levels. A patient's first chemotherapy treatment can kill the sensitive clones and leave a small population of resistant cells that will eventually grow and cause a cancer relapse. There is a need to study clonal heterogeneity and its effect on drug resistance.

Various *in vitro* cancer models were developed to research cancer treatments. The simplest and more common model is the 2D monolayer culture, where cancer cells adhere to a surface, such as petri dishes, and grow in a monolayer. The most realistic model involves using actual patient tumours, as they include the complete cancer microenvironment in three dimensions (3D). However, limited patient tissue is usually available to perform large experiment repetitions. Spheroids are 3D cell aggregated formed *in vitro* and represent an ideal compromise between simplicity, as the cell composition is known and controlled, and realism, as they better mimic the 3D nature of human tumours compared to monolayer 2D culture. Spheroids can easily be used to study clonal heterogeneity as multiple cell lines can be mixed at specific ratios to form co-culture spheroids.

The microfluidic community has developed microfluidic chips that can easily form and treat hundreds of spheroids. Here, microfluidic chips are used to reduce laboratory work by forming 120 spheroids in a single step and trap the spheroids in place so that medium and drug changes can be quickly done.

One of the main advantages of using spheroid as an *in vitro* cancer model is that hundreds of identical co-culture spheroids can be made to easily study various conditions. However, analyzing the dynamic response of individual cell populations of this large number of spheroids is still a

challenge. Researchers often use cell morphology, immunostains or fluorescent markers to identify cell populations. But many of these techniques rely on the direct observation of each cell in the spheroid and require either spheroid digestion into a single cell suspension or spheroid slicing into thin tissue slices. To analyze intact 3D samples, microscopy techniques such as confocal, multiphoton, and light sheet microscopy were developed. While they present many advantages, these techniques are either not adapted to analyze many spheroids in a single acquisition or cannot analyze up to the centre spheroids larger than 70-100 μm in diameter.

In this dissertation, a wide-field fluorescence hyperspectral imaging (HSI) system was designed, build and validated for co-culture spheroid research. The HSI system was specifically designed to image multiple spheroids in a single acquisition and for *in situ* imaging of spheroids in microfluidic chips. The HSI system design, presented in Article 1, is based on the use of a liquid crystal tunable filter and an electron-multiplying charged-coupled device camera to image spheroids in a 7.25 mm-in diameter field of view. An image analysis algorithm was also developed to compensate for any system response influencing the measured fluorescence intensity from each spheroid present in the image. A final quantification step to compensate for the optical properties of the sample was also developed and validated using optical phantoms.

Article 2 presents a methodology to study clonal heterogeneity and its relation to treatment response. Two fluorescent cell lines were derived from the same ovarian cancer cell line and used to form co-culture spheroids with various initial cell seeding ratios. Results show that the HSI system was able to follow each cell population growth and response to drugs over time, including for populations occupying only 10% of the spheroid. The onset of a clonal takeover was also observed when a high dose of chemotherapy drug was used to treat the spheroids. The HSI system was also able to highlight different response rates to the drug between the two cell populations.

Wide-field fluorescence hyperspectral imaging is an ideal technique to images multiple spheroids in a single acquisition. Its spectral resolution can quantify a larger number of fluorophores than standard microscopy filter sets. Hyperspectral imaging could also be used to study co-culture spheroids made of different cell types, such as epithelial and stromal cells, or cancer and immune cells.

TABLE OF CONTENTS

LIST OF TABLES

LIST OF FIGURES

LIST OF SYMBOLS AND ABBREVIATIONS

2D	Two-dimensional
3D	Three-dimensional
ADP	Adenosine diphosphate
ALA	5-aminolevulinic acid
BER	Base excision repair
BRCA	Human genes (BRCA1 and BRCA2)
CÉO	Cancer épithélial de l'ovaire
CI	Confocal imaging
CHUM	*Centre hospitalier de l'Université de Montréal*, University of Montreal Health Centre
CNC	Computer numerical control
CRCHUM	*Centre de recherche du CHUM*, CHUM research centre
CTG	CellTracker^{TM} Green
CTO	CellTracker^{TM} Orange
DMSO	Dimethyl sulfoxide
DNA	Deoxyribonucleic acid
DPSS	Diode-pumped solid-state
EDTA	Ethylenediaminetetraacetic acid
eGFP	enhanced Green Fluorescence Protein
EMCCD	Electron multiplying charge-coupled device
EOC	Epithelial ovarian cancer
FACS	Fluorescence activated cell-sorting
FBS	Fetal bovine serum

GFP	Green Fluorescence Protein
HBSS	Hank's balanced salt solution
HSI	Hyperspectral imaging
HR	Homologous recombination
IC_{50}	Concentration at which 50% of colony formation is inhibited
IHC	Immunohistochemistry
LCTF	Liquid crystal tunable filter
LLTF	Laser line tunable filter
LSFM	Light sheet fluorescence microscopy
MCTS	Multicellular tumor spheroid
NSERC	Natural science and engineering research council
OSE	Name of culture medium for ovarian cancer cells
OV1946	Ovarian cancer cell line
OV90	Ovarian cancer cell line
PARP	Poly(ADP-ribose) polymerase
PBS	Phosphate-buffered saline
PDX	Patient derived xenograft
PI	Propidium iodide
PDMS	Polydimethylsiloxane
PMMA	Poly(methyl methacrylate)
PpIX	Protoporphyrin IX
ROI	Region of interest
SIMSS	Single inlet multi-size spheroid
SPIM	Single plane illumination microscopy

STS117   Sarcoma cell line

TRIS-HCl   Tris(hydroxymethyl)aminomethane hydrochloride

USAF   United States air force

LIST OF APPENDICES

CHAPTER 1   INTRODUCTION

1.1 Motivation

Ovarian cancer is the deadliest gynecological cancer among women. Its five-year survival rate is less than 50%: an estimated 1 800 Canadian women will succumb to this cancer in 2018 [1]. While most patients initially respond well to the standard chemotherapy treatment, the majority will see their disease recur and experience drug resistance, a situation where a previously responding tumour will not respond to the same treatment [2], [3]. There is a need to study this treatment resistance phenomenon to understand its mechanisms. Several *in vitro* cancer models are available to researchers to study cancer. Two-dimensional (2D) monolayer cultures has been the gold standard over the past decades. However, there is now evidence that three-dimensional (3D) cultures are more relevant for *in vitro* research. Contrary to 2D cultures, they integrate cell-cell and cell-matrix interactions and better mimic *in vivo* tumours [4]–[8]. While many types of 3D culture exist, spheroids, 3D aggregates of known cell composition, represent an ideal compromise between the simplicity of monolayer cell lines and the realism of patient tumours. Many cancer cell lines have the ability to form spheroids in low attachment conditions, i.e. when cells are prevented from adhering to the surrounding surfaces. Clonal heterogeneity is a hallmark of ovarian cancer and is thought to be implicated in treatment resistance [9]. A tumour will typically develop from a single cell that underwent a genetic mutation allowing it to divide itself without limitations. Such cells can then acquire other genetic mutations, and so on, yielding a tumour composed of similar cells presenting different mutations, called subclones. One subclone could respond to a treatment, while a second could resist [10]. To study this phenomenon, spheroids can be made with more than one cell type, resistant and sensitive for example, to study the interaction between these cell populations.

Spheroids have been formed and studied using standard laboratory techniques. Using the hanging droplet method [11], for example, spheroids can be made by placing droplets of cell suspension on the cover of a petri dish. The cover is then flipped and placed on the bottom of the petri dish. Droplets then hang from the cover and cells aggregate at the bottom of the droplet and form a spheroid. Formed spheroids are then harvested in a suspension. One of the main challenges associated with this kind of formation method is that all spheroids are in the same suspension. To

study multiple conditions (drug type, drug concentration, exposure time), spheroids need to be manually pipetted into the wells of a 96-well plate. Then, medium changes and drug addition are also manually done by removing old medium and adding new medium in each well. In addition to being a time-consuming technique, as each well is addressed individually, spheroids can stick to the micropipette and be removed from the well. Other techniques used to form spheroids, such as commercial well plates designed for this, also suffer from these drawbacks [12]. To facilitate spheroid formation and handling, the microfluidic community has developed microfluidic chips that can easily form and treat hundreds of spheroids in a few experimental steps. Formation and culture of spheroids on-chip offer many advantages over traditional *in vitro* culture techniques [13]. Briefly, hundreds of spheroids can easily be formed using a single cell suspension. Medium and drug changes can be done in a single step without the risk of spheroids sticking to a micropipette tip. Other advantages are listed in section 2.2. Therefore, microfluidic chips were used throughout this work to form and treat spheroids.

However, analysis techniques commonly used to study cell populations in *in vitro* 2D cultures are not readily adaptable to 3D cultures in general or 3D culture in microfluidic chips [14]. When imaging fluorescent cell populations in spheroids with a traditional fluorescence microscope, the number of cells from each population cannot be counted as individual cells are not visible in the microscopy image, contrary to monolayer cultures imaging. Methods were developed over the years to take into account the 3D nature of spheroids. Some rely on the digestion of the spheroids into single cells to further analyze them using the traditional 2D techniques. Others use cryosections or paraffin embedding to slice the spheroids into thin layers that can also be analyzed using traditional techniques. Finally, microscopy techniques adapted for 3D culture have been used, such as confocal microscopy, multiphoton microscopy and light sheet microscopy. Each technique has its advantages and drawbacks depending on the type of study performed. Typical drawbacks are a lack of light penetration up to the spheroid centre [14], objectives with limited working distance [15], or difficulty to implement high-throughput imaging [16].

In this thesis work, a wide-field hyperspectral imaging (HSI) system capable of fluorescence quantification was designed and validated. The system was specifically designed to image spheroids while they are still trapped in microfluidic chips. Hyperspectral imaging is an imaging technique in which the measurement of the full spectrum (reflectance, transmittance, or fluorescence) of the sample is done for each pixel of the image, resulting in a hyperspectral

datacube. The system was first validated using flow cytometry, optical phantoms, and preliminary Monte Carlo light transport simulations. Spheroid imaging was then done on ovarian cancer co-culture spheroids over time in response to two types of chemotherapy, carboplatin and poly(ADP-ribose) polymerase (PARP) inhibitors to illustrate how HSI can be used to study clonal heterogeneity and its relation to treatment resistance in ovarian cancer.

1.2 Research objectives

The aim of this dissertation is to provide a versatile and high-throughput analysis instrument to measure the fluorescence of 3D samples cultured in microfluidic chips. The first objective was to determine if hyperspectral images of spheroids in a field of view of a few millimetres in diameter could be acquired. A tunable filter was selected to scan the fluorescence emission spectrum of the spheroids and to acquire one image per interrogated wavelength. Also, a low numerical aperture objective was used to image the large field of view wanted. Since both design choices, i.e. the tunable filter and the low numerical aperture objective, limit the fluorescence intensity reaching the camera, a highly sensitive electron multiplying charged-coupled device (EMCCD) camera was selected to allow the detection of the fluorescence.

Objective 1: Design and build a wide-field hyperspectral imaging system to measure non-destructively the fluorescence emitted by co-culture spheroids cultured in microfluidic chips.

Hypothesis 1: High-throughput hyperspectral images of 300 µm-diameter fluorescent spheroids can be achieved using a highly sensitive EMCCD camera to compensate for the low transmission of the tunable filter and objective numerical aperture.

The second aim of the thesis work is to validate that the HSI system can, first, quantify fluorescence and compensate for the imaging system response and the optical properties of the sample. 3D cultures optical properties can change according to the compactness of the culture and the measured fluorescence intensity will be affected by this. As the sample optical properties can prevent light propagation up to the centre, the second validation is to evaluate if HSI can image up to the spheroid centre in order to study the whole spheroid response to external stimuli and not only the outer layers response. Finally, the HSI system will be compared to a gold standard to verify

that fluorescence intensity can be used to calculate the proportions occupied by each cell population in the spheroid.

Objective 2: Validate the hyperspectral imaging system and evaluate the ability of image analysis algorithms to quantify fluorescence, sampling up to the spheroid centre, and measure spheroid composition in co-culture spheroids.

Hypothesis 1: The sample transmittance spectrum can be used to quantify the sample fluorescence from its optical properties in an empirically based equation.

Hypothesis 2: Elastic scattering and absorption properties of spheroids are low and do not prevent measuring the fluorescence at the spheroid centre using hyperspectral imaging.

Hypothesis 3: Hyperspectral fluorescence intensity directly relates to the number of cells and can be used to measure the composition (% of spheroid) in fluorescent cell populations of co-culture spheroids

---

The third and final objective of this work is to use HSI to study the response to external stimuli (medium changes, drug types, drug concentrations) of co-culture spheroids over time and non-destructively. A treatment response study was performed to determine how drugs affect the spheroid composition over time as well as determine if dose-dependent responses can be observed.

Objective 3: Study clonal heterogeneity in ovarian cancer by forming co-culture spheroids and follow their response to chemotherapy treatments on-chip over time.

Hypothesis 1: By measuring spheroid composition over time, hyperspectral imaging can measure the drug response of each cell population and identify distinct behaviours.

1.3 Dissertation organisation

This project is the result of the collaboration between three laboratories, each bringing their own expertise:

1. Microfluidics for Oncology Laboratory, lead by Thomas Gervais, expertise in microfluidic and 3D culture;

2. Laboratory of Radiological Optics, lead by Frédéric Leblond, expertise in imaging systems and fluorescence quantification;

3. Anne-Marie Mes-Masson laboratory situated at the *Centre hospitalier de l'Université de Montréal* (CHUM) research centre, expertise in ovarian cancer and 3D culture.

Researchers from each laboratory participated in the research and in the two articles presented in this dissertation. Before each article, a paragraph introduces the context of the work and details each co-author's contribution. Also, work done by students Alexandre Chabot and Didier Blach-Laflèche, by then-master's student Catherine St-Pierre [17], and by post-doctoral fellows Mohana Marimuthu and Ehsan Edjlali are described in the appendices.

Chapter 1 presents the dissertation aim and research objectives. It also presents the dissertation organization. The literature review is presented in Chapter 2 and details what is treatment resistance and its relation to ovarian cancer, how microfluidics can be used for spheroid-based research, how cell populations in a 3D culture can be measured individually, and how fluorescence quantification is done. Chapter 3 presents the general methodology used through this work. The first article written on work from this dissertation is reproduced in Chapter 4. It was published in *Analyst* and presents the HSI system and the first hyperspectral images of fluorescent co-culture spheroids in microfluidic chips. The second article is submitted to *Integrative Biology* and showcase proliferation and treatment response assays performed with the HSI system is presented in Chapter 5. Chapter 6 presents a general discussion on hyperspectral imaging for spheroid-based research and Chapter 7 presents the conclusion. Appendix A showcases the preliminary work on spherical optical phantoms. Preliminary results of Monte Carlo light propagation simulations are shown in Appendix B. Appendix C presents a modification to a statistical test that I proposed to analyze Mohana Marimuthu's results in her article. Appendix D details the image analysis algorithm developed for this work. Finally, Appendix E lists my contributions in terms of articles, oral presentations, and scientific posters based on this work.

CHAPTER 2   LITTERATURE REVIEW

2.1 Ovarian cancer

In Canada in 2017, they were 2 800 estimated new cases and 1 800 estimated deaths due to ovarian cancer [1]. Ovarian cancer has the highest mortality rate among gynecological cancers and the most common form is epithelial ovarian cancer (EOC) [18]. Despite advances in surgery and chemotherapy over the last few decades, the 5-year survival rate of patients with EOC in the United States from 2007 to 2013 is still less than 50 % [19]. Ovarian cancer also has the particularity of presenting ascites, i.e. excess peritoneal fluid containing cancer cells [20], [21]. The disease is usually discovered in late stages due to its asymptomatic nature and because no efficient screening methodology as been demonstrated yet [19]. Also, a high proportion of patients who initially respond to the standard chemotherapy treatment of taxanes combined with platinum agents will then develop resistance to this treatment [2], [3]. By the time healthcare professionals observe if a patient is resistant to the chemotherapy treatment, the patient has undergone a high morbidity associated to an unnecessary treatment. Healthcare resources are also wasted.

The standard chemotherapy treatment for ovarian cancer consists of a combination of two chemotherapy drugs: taxanes and platinum agents. Both types of drugs target dividing cells, whether cancerous or not. Since cancer cells divide faster than normal cells in the body, they will be more sensitive to chemotherapy drugs. Taxanes, such as paclitaxel, cause microtubule assembly and stability during cell division, blocking the cell cycle in the mitosis. Platinum agents target cancer cells by creating crosslinking in and between DNA strands, which prevent the cell from synthesizing DNA to divide [22].

Other treatments have been developed to improve patient survival and circumvent resistance to the standard chemotherapeutic treatment. Normal and cancer cells rely on various mechanisms to repair DNA damages naturally occurring during cell division or inflicted by their environment (using chemotherapy drugs, for example). PARP inhibitors are a recent class of drugs that are used to treat ovarian cancer in addition to chemotherapy. Their mechanism of action is based on inhibiting PARP1 and PARP2, enzymes implicated in the base excision repair (BER) pathway, and trapping PARP 1 on damaged DNA, rendering its repair impossible. Cells where other DNA repair pathways are compromised will accumulate DNA damages leading to cell death. This idea where

two DNA damage repair pathways are dysfunctional is called synthetic lethality [23]–[25]. In the case of EOC, a second deficient DNA repair pathway is often found in tumours presenting mutations in the BRCA 1 and BRCA 2 genes, leading to the presence of synthetic lethality [26]. PARP inhibitor Olaparib is now approved by Health Canada for ovarian cancer treatment since August 2016 [27]. While PARP inhibitors can improve patient response to chemotherapy treatments, there is still a need to better understand the mechanisms behind this resistance phenomenon.

2.1.1 *In vitro* cancer models

To study cancer *in vitro*, several types of cancer models were developed, ranging from the simplest to the most realistic [28]. Figure 2-1 lists several types of *in vitro* cancer models in terms of their realism and their complexity of use. The following sections will detail ovarian *in vitro* cancer models, but the same models are used for other types of cancer.
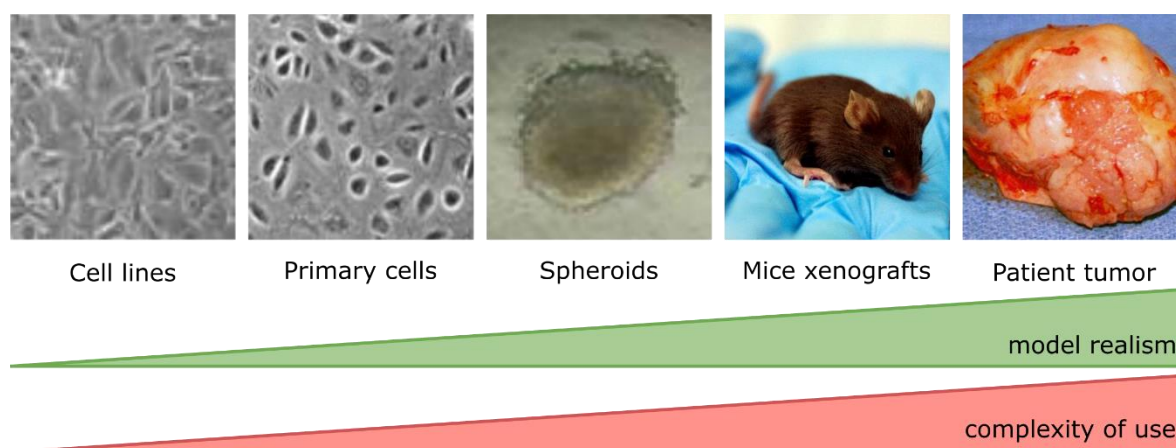
Figure 2-1 : *In vitro* ovarian cancer models as a function of realism and complexity of use. Images from [29]–[33].

2.1.1.1   Cell lines

Cell lines cultured in monolayers represent the simplest *in vitro* tumour model. Immortalized human cell lines are a population of cells that can divide indefinitely, contrary to normal cells, due to a natural or induced mutation. They can be cultured for long periods of time *in vitro* and simplify studies of cells that would otherwise have limited proliferation and survival. Cell lines can be established from patient tumours or ascites, retaining the various genetic mutation of the

patient [34]. For example, two cell lines used throughout this study are OV1946 [35] and OV90 [36], derived from patient ascites in 2008 and 2000. While cell lines are easy to use, they are the furthest in terms of model realism to a patient tumour *in vivo*.

2.1.1.2   Primary cells

Primary cells are patient cells cultured *in vitro* for short periods of time, before any immortalization occurs. This type of cell can divide a few times when cultured in 2D monolayer culture. They are closer to the original tumour, but their usually low division rate and their short survival rate in culture render them more complicated to use compared to cell lines. Since patient cells are often available in limited supply, experiments requiring large numbers of cells are impossible to perform using this type of cells.

2.1.1.3   Spheroids

To increase the realism of *in vitro* cancer models, cell lines or primary cells can be cultured in 3D, in aggregates of cells called spheroids. These aggregates better represent the 3D complexity of tumours, while still being easier to handle compared to patient tumours. Spheroids display cell-cell and cell-matrix interactions that are present in tumours, increasing their relevance for *in vitro* cancer research [4]–[8]. Because of their 3D structure, molecular exchange gradients will be established between the centre and the outer layer, such as oxygen, nutrients, and waste (lactate) gradients. These gradients, illustrated in Figure 2-2, will first affect how spheroids grow. Spheroids will undergo an exponential growth when few cells are present. Then, contrary to cells cultured in monolayers, spheroid volume will reach a plateau after extended periods of culture [14]. Also, if spheroids are larger than a critical volume, oxygen will be consumed by the outer layers before having the time to diffuse up to the spheroid centre, creating a hypoxic core often encountered in tumours without vascularization [37]. Furthermore, the genetic expression of cells grown in 3D is different from those grown in 2D. Because cancer is caused by genetic disruption of the cell, this difference strongly influences *in vitro* studies [4], [38]. Studies have also found that treatments ineffective on 2D cultures of cancer cells can be effective against the same cells cultured in 3D [37]. 3D culture was also found to be generally more resistant to chemotherapy treatments than their 2D counterparts [37], [39].
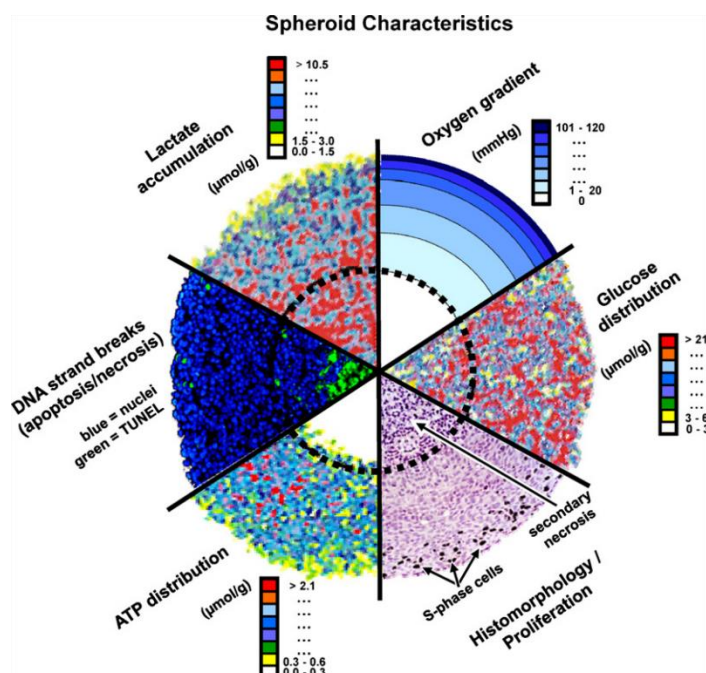
Figure 2-2: Spheroids gradients from the centre to the outer layers. Reproduced with permission from [40].

In summary, spheroids are 3D aggregates that are more realistic than 2D culture but are still easy to use because of their known cell composition and controlled size. It is also simple to form large quantities of identical spheroids to study the effect of a stimulus on identical samples. More complex 3D structures can also be formed, called organoids, with properties and function similar to the organ of origin [41], [42].

2.1.1.4 Xenografts

Xenografts are formed by injecting human tumour cells into a host, typically a mouse with a defective immune system [43]. Cells can be injected under the skin or into the organ of interest and tumour growth can last a few weeks or months. Tumour response to treatment is typically assessed by injecting the drug of interest subcutaneously or systemically and measuring the affected growth of the tumour. Grown tumours can also be harvested once they reached a specific size and then studied *in vitro*. Xenografts can be made using cancer cell lines or using cells extracted from patients (patient-derived xenografts, PDX). Xenografts are more representative of a real tumour than spheroids because they incorporate a more complete tumour microenvironment than spheroids

cultured in liquid medium. However, they are more complex to study as the specific cell composition is not known: human non-cancer cells or host cells can infiltrate the tumour [43].

2.1.1.5   Tumours and biopsies

Finally, the most realistic cancer model to study *in vitro* is the tumour itself, in the form of surgery-resected tissue or a biopsy sample. However, maintaining tumour tissue alive outside the body and *in vitro* is difficult. Since oxygenating large tumour fragments requires vascularization, the tumour often needs to be cut down to submillimetre sizes to allow oxygen and nutrients diffusion through the tissue [44], [45]. Furthermore, the tumour cell composition is not known, as stromal, epithelial, and immune cells, as well as the extracellular matrix and proteins will be present in the tumour, which can complicate some types of *in vitro* research [46], [47]. In drug discovery, the main drawback of using patient tissue is the low number of available cells and the fact that repeated analysis over weeks cannot be done.

In summary, each *in vitro* cancer model has its own advantages and disadvantages and selecting the most appropriate one for a specific study is crucial. In this project, spheroids were selected as the most appropriate model to study because of their known cellular composition and the fact that they can be made from cell lines.

2.1.2   Including clonal heterogeneity in *in vitro* cancer models

Similar to Darwin's theory of evolution, tumours are believed to be cell populations evolving under the constraints of the microenvironment [48], [49]. Cancer usually develops from a single cell that underwent a genetic mutation making it proliferate uncontrollably, forming a mass of cells called a tumour. While the tumour grows, its cells can mutate and transfer their mutations to their daughter cells, as illustrated in the left part of Figure 2-3. As the number of cancer cells increases, combined with the constant acquisition of genetic mutations, tumours will often be composed of multiple clonal populations, or subclones, by the time the cancer is diagnosed [50].

Traditionally, treatment resistance was thought to be either intrinsic (already present at the beginning of the tumour growth) or acquired (developed after the initial treatment) [10]. Now, our understanding of clonal heterogeneity has led to the hypothesis that giving a treatment to a patient changes the dynamics of clone mutations and survival, as shown in the right part of Figure 2-3. Treatment sensitive subclones die as resistant subclones survive. These resistant subclones can then

repopulate the tumour over time and lead to a cancer relapse. If the same treatment is given to the patient, it will fail [10].
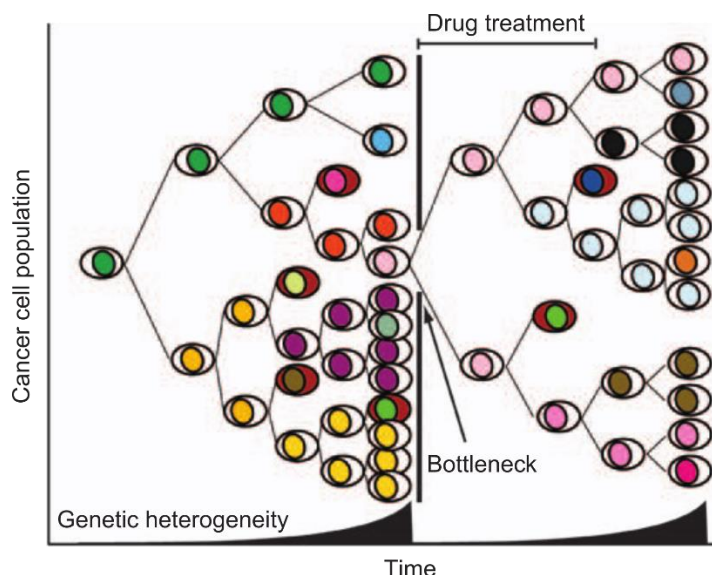
Figure 2-3: Evolution of clonal heterogeneity over time and in response to a treatment. Reproduced with permission from [50].

Moreover, there is evidence that two subclones can cooperate and increase tumour progression and metastasis potential [9], [51], [52]. For example, mesenchymal-like cells that were co-transplanted in mice with tumours initiating cells (TICs) promoted their tumour initiating capability, even if the mesenchymal-like population represented a minor population [53].

As explained in section 2.1, ovarian cancer presents a high rate of cancer relapses that were revealed to be resistant to the treatment that was previously effective. High grade serous EOC presents a high level of genetic instability over time and spatially, because of mutations in the TP53 gene and deficiencies in the DNA repair pathway homologous recombination (HR). Clonal survival to treatment could explain these high levels of treatment resistance [9]. Caswell and Swanton [51] wrote in their research paper:

> "[…] to more effectively treat heterogeneous tumours, we must first understand the dynamics between different populations within a tumour, and how targeted treatment changes these interactions".

By mixing two or more carefully chosen cell types or subclones in *in vitro* cancer models, the effect of each subclone on the other or their respective response to treatment can be studied. **This**

dissertation focuses on the need to develop a versatile method to quantify cell populations over time in co-culture 3D cultures.

2.2 Spheroids formation and microfluidic chips

In this project, spheroids were chosen as a 3D *in vitro* cancer model because of their known cellular composition and the fact that hundreds of identical samples can be made in a reproducible manner. Standard laboratory techniques were developed and used to form large numbers of spheroids [12], [54]–[56]. These different methods are illustrated in Figure 2-4 and are mainly based on a simple idea: cells cultured on low-attachment surfaces will aggregate and form cell-cell interactions. Not all cell lines can adapt to low-attachment conditions, but many cancer cell lines are known to be. For example, ovarian cancer cell lines OV1946 [35] and OV90 [36] will spontaneously form spheroids when cultured in low attachment conditions. In this work, the hanging droplet method (Figure 2-4A) was used [11]. Briefly, droplets of cell suspension are carefully deposited on the inside of a petri dish cover. Between 100 and 120 droplets can be formed using a 150 mm petri dish. The cover is then placed back on the dish bottom. Cells sediments to the droplet bottom and form spheroids in 4 to 7 days, depending on the cell line used. Another method often used is represented in Figure 2-4B. Cells are deposited on top of low-attachment coatings, such as Matrigel^{TM}, agarose, or hydrophobic coatings [57]. However, this method does not control spheroid diameter and spheroids of various sizes will be formed.

An emerging method to form spheroids uses microfluidic chips. Microfluidics is the manipulation of liquids confined at the microscale level where fluid behaviour can be very different from that at the macroscale level. It can offer many advantages over standard spheroid formation techniques, as standard laboratory techniques can be cumbersome to use [13], [58], [59]. Briefly, in microfluidics, viscous and capillary forces become the dominant forces and the flow in microchannels is laminar. By exploiting this laminar flow, fluids and particles in the fluid can be precisely controlled [60]. In this project, these microfluidics advantages are utilized to:

1. precisely control how many cells will form a spheroid;

2. efficiently trap spheroids in place once they are formed, in order to change the medium or exposed them to external stimuli easily;

3. reduce laboratory work by forming large number of spheroids and doing medium changes a single step;

4. optimize cell culture conditions by mathematically modelling parameters affecting cell viability, such as nutrients and oxygen diffusion, and shear stress.
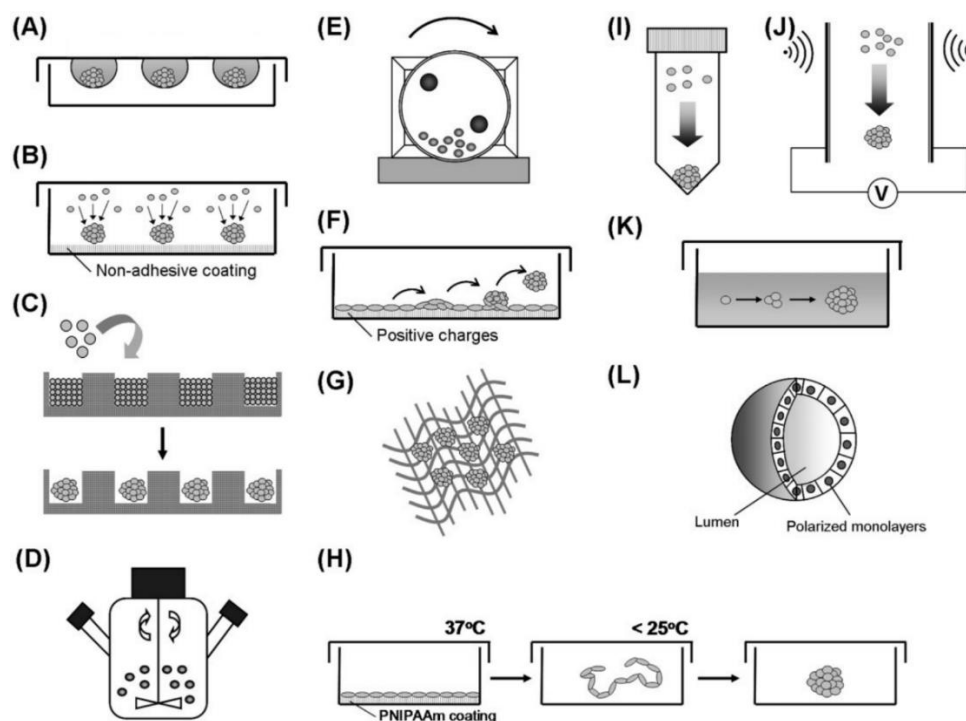
Figure 2-4: Methods for multicellular spheroid generation. (A) Hanging-drop culture. (B) Single cell culture on non-adhesive surface. (C) Micromolding techniques. (D) Spinner flask culture. (E) Rotary cell culture systems. (F) Hepatocyte self assembly on Primaria dishes. (G) Porous 3-D scaffolds. (H) The use of PNIPAAm-based cell sheets. (I) Centrifugation pellet culture. (J) Electric, magnetic or acoustic force cell aggregation enhancement. (K) Monoclonal growth of tumour spheroids. (L) Polarized epithelial cysts. Reproduced with permission from [57].

Microfluidic chips are often made of polydimethylsiloxane (PDMS), a flexible polymer that is also optically transparent in the visible region, making fluorescence microscopy through the chip possible. PDMS is also gas-permeable to oxygen, necessary for cell viability, and biocompatible because of its inert nature [60]. The first step in fabricating a chip is to make a master mould. Moulds were traditionally done using photosensitive resin deposited on silicon wafers and lithography. In recent years, advances in spatial resolution made 3D printing and plastic

micromachining appropriate techniques to make a negative of the desired channel geometries on a master mould. Figure 2-5 illustrates the different steps to make a PDMS chip. First, liquid PDMS is poured on the master mould and cured in an oven. The PDMS is then peeled off the mould and inlets and outlets are punched if necessary. A plasma treatment containing oxygen is then applied on two layers (PDMS + PDMS, or PDMS + glass) that are then pressed together to bond and form the finished chip.
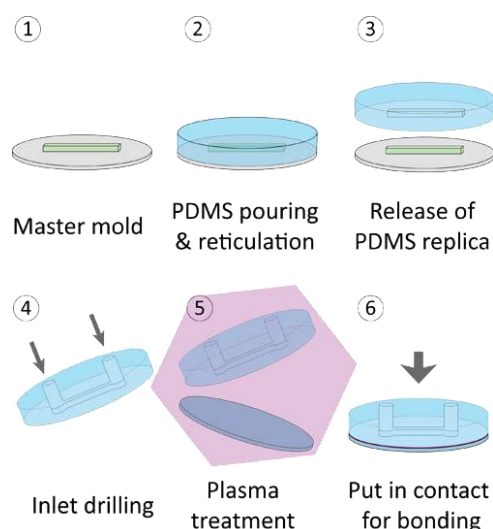
Figure 2-5 : Microfluidic chip fabrication from a master mould [61].

Because of the advantages offered by microfluidic chip, many research groups have developed chip designs to form and culture spheroids on-chip. All designs achieve a similar goal: concentrating single cells in a small volume so that they aggregate together and form spheroids [13], [58], [59], [62]–[67].

A first design utilizes U-shaped traps inline with the main channel (Figure 2-6A) to aggregate cells. U-shaped traps can be fixed [68] or active [69]. Active traps are mainly used to extract the spheroids from the chip by deactivating them.

Many research groups, including ours, uses passivated microwells to trap cells (Figure 2-6B) [70]–[74]. The PDMS is first passivated to prevent cell adhesion to the wells and promote cell-cell interaction instead. A cell suspension is introduced in the chip and cells sediment in the wells and aggregate to form spheroids. By optimizing the geometry and flow rates used to change medium, spheroids can be efficiently trapped in the well to minimize unwanted ejection [45].
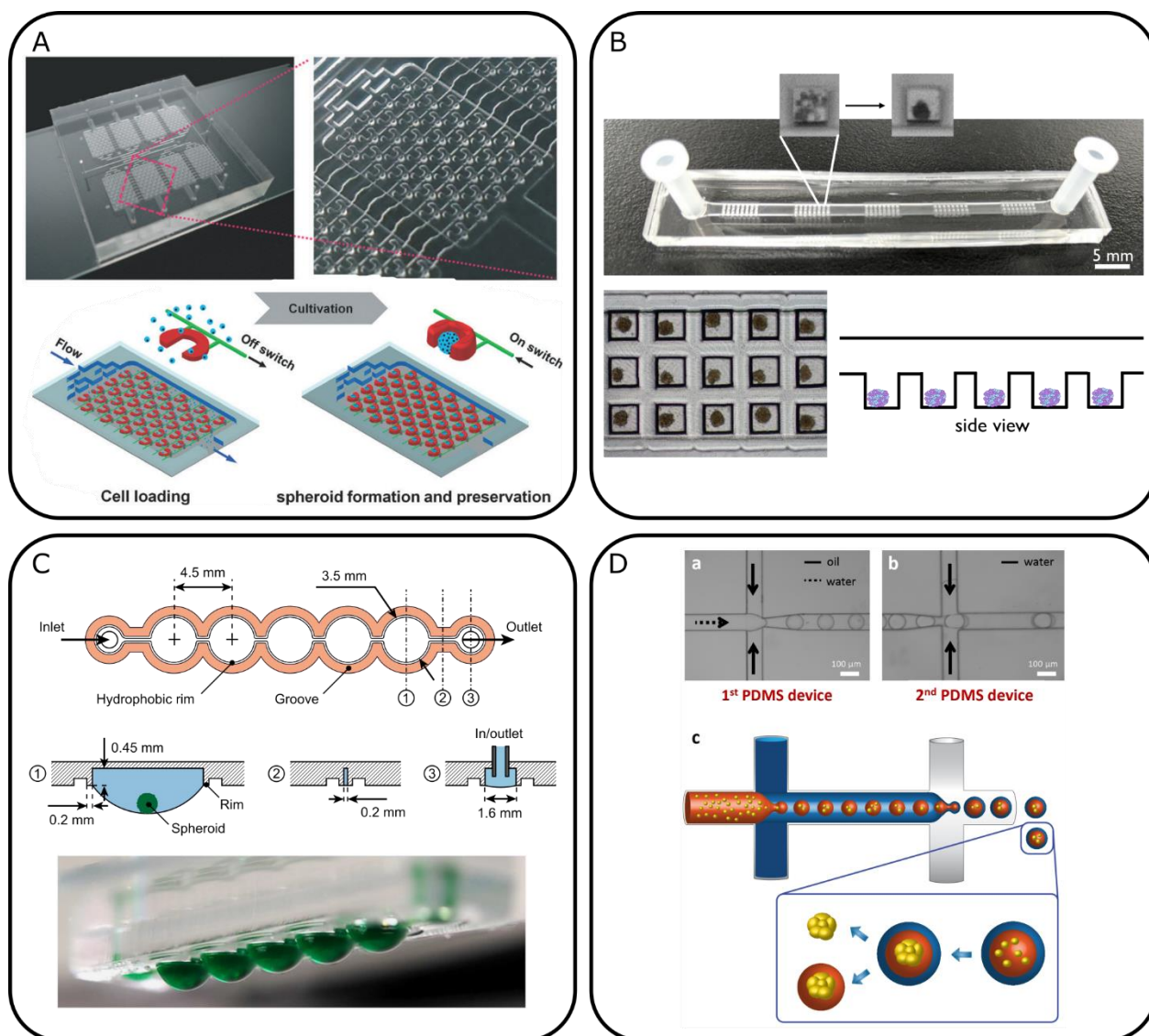
Figure 2-6: Microfluidic-based spheroid formation methods. A) U-shaped cell trapping, reproduced from [69] with permission from The Royal Society of Chemistry. B) Microwell cell trapping, our work [75]. C) Hanging droplets on-chip, reproduced from [76] with permission. D) Droplet-based cell trapping, reproduced from [77] (CC BY-NC-ND 3.0).

A third design was inspired by the standard hanging droplet method: connected droplets are formed using an open microfluidic chip (Figure 2-6C) [76], [78]. Cells sediment to the droplet bottom and form spheroids, as in the standard hanging droplet method. The microfluidic version offers the advantage of easily allowing and controlling fluid changes in the droplets, which is impossible with the standard technique.

Finally, as droplet formation on-chip is an established field in the microfluidic community [79], its techniques were applied to form spheroids on-chip [77], [80], [81]. Droplets of cell suspension are formed in an immiscible carrier (such as oil) and as cells cannot adhere to the water-oil interface, they instead aggregate together (Figure 2-6D).

Depending on the spheroid formation design used, some microfluidic chip can also culture spheroid over time to expose them to external stimuli. Other designs require the use of a second chamber or chip to immobilize the spheroids and culture them [13]. The microfluidic community has also developed guidelines to form and culture on-chip [45], [82].

2.3 Measuring cell populations in 3D cultures

Section 2.1.2 highlighted how including clonal heterogeneity by mixing multiple cell types or populations in spheroids increases the relevance of this *in vitro* cancer model for ovarian cancer studies. However, the main challenge associated with studying heterogeneous spheroids is developing techniques that can analyze each cell population individually [83]. For example, measuring the diameters after a certain treatment of spheroids made from two cell lines will not discriminate if one cell line responded more than the second to the treatment. It will only assess the response of the whole spheroid. Over the years, researchers have developed such techniques to discriminate subpopulations of cells.

2.3.1 Cell population discrimination techniques

2.3.1.1 Cell morphology

Cellular morphology can be used to identify cell types based on their shape and size when cultured on adherent surfaces such as petri dishes. Jones *et al.* [84] employed cell segmentation to calculate several parameters per imaged cell, such as the area, the roundness, and the width of both the nucleus and the cell, and used those parameters to identify cell populations. Garvey *et al.* [85] and Caicedo *et al.* [86] used supervised and unsupervised classifiers to further automate the classification of each cell to a specific population. But to analyze spheroid composition using the previous methods, spheroids need to be digested into single cells that are then plated in 2D monolayer culture since cellular morphology cannot be distinguished in 3D culture. This spheroid digestion adds experimental steps to the study and is also a destructive technique that cannot

analyze the same spheroid over time. Finally, Härmä *et al*. [87] developed a software to automatically analyze the morphology of whole spheroids, but this technique cannot distinguish individual population in a spheroid.

2.3.1.2   Immunostaining

Others have used immunostains to identify cell populations by their expressed proteins profile. In a simplified explanation, an antibody that is coupled with a chromophore or a fluorophore binds to specific part (epitope) of a protein of interest. Using absorption (chromophore) or fluorescence (fluorophore), the presence and localization of this protein can be measured. In the case of 3D spheroid analysis, this method is performed on thin spheroid slices, either paraffin-embedded slices or cryosections. Immunostains can also be used to stain digested spheroids that are then analyzed by flow cytometry (described in section 2.3.2.1). Kilani *et al*. [88] used epithelial- and fibroblast-specific immunostains to observe each cell type response to treatment. Finally, Ahonen *et al*. [89] identified mouse and human cell in spheroids formed from a digested mouse xenograft using fluorescent antibodies specific for mouse and human proteins.

2.3.1.3   Fluorescent trackers

Two types of fluorescent markers can be used to identify cell populations. The first utilizes fluorescent trackers on initially distinct and separate populations. Each population is first stained using different fluorescent molecules that are then retained inside the cells. This technique is mostly used for medium-term monitoring, as the number of fluorescent trackers in each cell will decrease as cells divide and fluorescent molecules are divided between the mother and daughter cells. Because of this, fluorescence quantification to count the number of cells from each population cannot be done using trackers [90], [91]. Still, this method can identify the presence of a specific cell population in a spheroid or be used to observe if spheroid populations are completely mixed or if populations aggregated in distinct regions of the spheroid. For example, Go *et al*. [92] used two fluorescent trackers to stain cancerous and normal cells and observe how tumour spheroids invade into normal rat brain aggregates.

2.3.1.4   Fluorescent proteins

Finally, cell lines can be genetically modified to express fluorescent proteins. This technique cannot be used if patient cells are studied, as modified cells will typically not express the proteins

at the same intensity level, rendering any quantification impossible. However, this technique is especially useful to study spheroids made from cell lines [90]. Cell lines can be transfected using a plasmid integrating the genetic code of one of the many fluorescent proteins available since the discovery of the Green Fluorescent Protein (GFP) [93], [94]. Once transfected, a limiting dilution in well plates can be done to isolate single cells from which clonal populations can be derived. For a specific subclone, the fluorescence intensity emitted by the cells will be at the same level, allowing fluorescence quantification to count cells. Hsiao *et al.* [95] followed the proliferation of DsRed-transfected prostate cancer cells inside a spheroid made from osteoblast and endothelial cells.

2.3.2 Instrumentation for fluorescence-based discrimination methods

Since fluorescence-based techniques such as genetically modifying a cell to express fluorescent proteins can be quantitative (where cells express about the same amount of proteins for a specific population, for example), the next sections focus on detailing fluorescence-based techniques used in the literature to measure cell populations.

2.3.2.1 Flow cytometry

Flow cytometry and the more specific fluorescence-activated cell sorting (FACS) are considered the gold standard along with immunohistochemistry on tissue sections (section 2.3.1.2) in evaluating cell populations. During flow cytometry measurements, single cells are passed through a flow cell with a width similar to the size of the cells. Around the flow cell is an optical system with various excitation lights and detection channels. One by one, cells are analyzed for their light scattering properties (forward and side scattering) and their fluorescence [96]. Cells are separated into different populations according to these measurement values. Flow cytometers are highly versatile in terms of how many fluorophores can be measured. The system used during this dissertation can analyze up to 18 different fluorophores using 7 lasers. In this case, the number of cells marked by each fluorophore studied can be counted to measure cell populations. Flow cytometry has also been adapted to large particle analysis, such as whole organism (C. Elegans), embryoid bodies, and spheroids [97], [98]. There is also a large part of the microfluidic community that specialize in developing flow cytometry on-chip, as flow cytometry's simplest form is a microfluidic channel [99]–[101]. Finally, image cytometers are starting to be available

commercially [56], [102], [103]. While flow cytometry is a precise and versatile technique to analyze cell populations, repeated analysis over time cannot be achieved as spheroids often need to be digested into single cells to be analyzed using standard flow cytometers. Also, image cytometers often lack the depth of field necessary to image thick samples in a single acquisition and are not adapted for *in situ* imaging of microfluidic chips [103].

Nonetheless, researchers have used flow cytometry to analyze digested spheroids. Patra *et al*. [104] developed a microfluidic chip capable of forming and perform drug testing on 5 000 spheroids easily. Spheroids were then harvested from the chip, digested, and analyzed through flow cytometry using apoptosis stains to assess the average spheroid response to drugs. Ivanov *et al*. [105] used fluorescent live stains prior to forming co-culture spheroids. The analysis was then performed on fixed spheroids using multiphoton microscopy and on digested spheroids using standard and imaging flow cytometry.

2.3.2.2 Tissue sections

To preserve their morphology and the localization of each cell population, spheroids can be sliced in sections or a few micrometres-thin and immunostains are used to reveal the location of their corresponding antigens and targeted proteins. The slicing can be done on frozen spheroids to generate cryosections. Spheroids can also be fixed and embedded in paraffin before the slicing procedure to preserve them indefinitely. Several groups have studied spheroids using immunofluorescence. Ivanov *et al*. [106] developed a technique to form spheroid arrays facilitating their immunohistochemistry (IHC) staining. Fang *et al*. [107] first established stable fluorescent cell lines and then co-cultured them in a 3D construct based on cells surrounding a mouse tumour xenograft. Confocal microscopy and cryosections were then used to quantify cell populations over time. Dorst *et al*. [108] later stained each cell line using live cell fluorescent stains prior to forming co-culture spheroids. Analysis was performed on spheroid cryosections and compared with FACS measurement of digested spheroids. Apart from the fact that slicing fixed or frozen spheroids is a destructive technique, it also present drawbacks such as sample damage due to the sectioning technique and presence of ice crystals during spheroid freezing that also can distort the sample morphology [14]. Weiswald *et al*. [109] and later Smyrek *et al*. [110] developed a technique to stain whole spheroids. The researchers then used confocal and light sheet microscopy (detailed in sections 2.3.2.3.2 and 2.3.2.3.4) to image the spheroids.

2.3.2.3 Microscopy techniques

Various microscopy techniques can be used to observe and measure the cell population fluorescence on two types of samples, either single cells from digested spheroids or whole spheroids.

2.3.2.3.1 *Fluorescence microscopy*

A single cell suspension obtained from digested spheroids can be plated in petri dishes to let cells adhere and the number of fluorescent cells from each population can be counted using an optical fluorescence microscope. Garvey *et al*. [85] developed a technique to analyze automatically the cell morphology and cell fluorescence of monolayers of cells cultured after spheroid digestion. While this technique leads to precise results because it analyzes each the parameters of each cell individually, it is again a destructive technique. Following each cell population response dynamics over time to external stimuli can reveal more information than using only end-point assays, as cancer is a dynamic process [48]. Thus, the next sections will focus on imaging techniques to measure whole spheroids.

Optical fluorescence microscopy can visualize cells marked with fluorescent markers, whether in 2D, as described before, or in 3D. When a 2D sample is imaged, fluorescent cells from each cell population can be directly counted. However, when a 3D sample is imaged, the same fluorescent cells cannot be counted as fluorescence from before and after the focal plane is superposed, resulting in an out of focus image where individual cells are not seen. However, the total intensity from all superposing layers can be used to quantify cell populations. Achilli *et al*. [111] measured the kinetics and the extend of self sorting when two populations are mixed to form spheroids using conventional epi-fluorescence microscopy. However, in their work, spatial fluorescent intensities of a spheroid were normalized to the total intensity of the imaged spheroid, since the goal of the research was to observe the spatial position of both subpopulations. To quantify exactly the spheroid composition, more precise and absolute fluorescence quantification of each subpopulation is needed. Still, conventional optical fluorescence microscopy can be used to semi-quantify fluorescence. If acquisition parameters are constant between samples, fluorescence intensity will be directly related to the amount of each fluorophore. Acquisition parameters are generally related to sample preparation, fluorescence excitation, magnification, focus, and camera acquisition time and gain [112]. A typical limitation of conventional optical microscope is that they are designed to

image cell monolayers and have thin depths of field, thinner than the spheroids imaged [113]. Where the focus will be made (on the top or bottom of the spheroid) will have an impact on the measured fluorescence, rendering absolute fluorescence quantification from sample to sample difficult [114], [115].

Ortiz de Solorzano *et al.* [116] developed a miniaturized fluorescence microscope to image spheroids. Lens free fluorescence microscopy [117] also offer advantages to image spheroids with large fields of view and using simpler field portable devices. While their imaging systems have a reduced footprint, the use of fixed excitation filters to remove the excitation light limit the number of fluorophores imaged.

2.3.2.3.2 *Confocal imaging*

Confocal microscopy is the solution to the fluorescence superposition from cells before and after the focal plane. Pinholes are placed in front of the source and the detector to image only the focal plane. Photons coming from other planes of the sample are blocked by the pinhole of the detector and a virtual slice of the sample is imaged, called an optical section. By varying the position of this focal plane, it is possible to sweep the sample over its height and acquire an image at each height, measuring the spatial distribution of fluorescent markers [118], [119].

However, confocal microscopy cannot image up to the centre of larger spheroids because of low signal intensity from the centre. Only the first 70 to 100 µm can be imaged, as illustrated in Figure 2-7 [44], [120]–[124]. When samples larger than 100 µm are imaged, the use of the pinholes to create optical sections of the sample greatly limits the light intensity reaching the detector. This is the compromise that confocal imaging dictates: lower detected intensity for optical sections [118]. Despite light detection problems, many research groups used confocal imaging to study spheroids, by either using smaller spheroids, or measuring only the outer layers response to external stimuli [107], [125], [126]. Also, some have developed methods to compensate this problem. Barbier *et al.* [127] developed a method to identify spheroids large enough to present this light penetration problem and remove them from the subsequent analysis. Stoddart *et al.* [53] designed a technique to rotate the sample to image it from different angles. Ahonen *et al.* [128] achieved whole spheroid imaging by fixing the spheroid in a matching refractive index medium, increasing the amount of detected light. While these last techniques can compensate for confocal imaging's

difficulty to image thick sample, it remains challenging to quickly analyze subpopulations in larger co-culture spheroids over time.
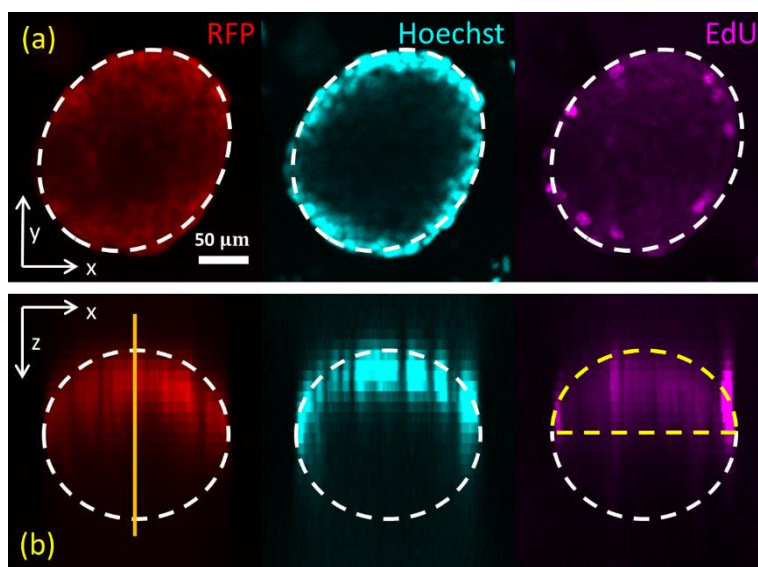
Figure 2-7: A) Top view of spheroids stained with three fluorophores and imaged using confocal microscopy. B) Side view of the same spheroids, showing different imaging depth. Reproduced with permission from [127] (CC BY 4.0).

2.3.2.3.3 *Multiphoton imaging*

Multiphoton microscopy takes advantage of longer excitation wavelengths to image deeper in thick samples. Briefly, in two- or three-photon microscopy, two or three photons of lower energy are used to excite a fluorophore in a single event. Since multiphoton excitation cross section is usually small, only the fluorophores located at the focal spot of the microscope will be excited, creating an optical sectioning similar to confocal microscopy [129]. Ivanov *et al.* [105] used two photon microscopy to image whole spheroids to identify the location of two subpopulations in spheroids, observing their self-sorting into distinct aggregates. While multiphoton microscopy can offer great results, objectives typically used have higher numerical apertures and shorter working distances to increase the excitation laser intensity at the focal spot [15]. This can be a problem to image spheroids while they are still trapped in a microfluidic chip, since the PDMS layers surrounding the spheroid can be thicker than the objective working distance.

2.3.2.3.4   Light sheet microscopy

Also called orthogonal plane fluorescence optical sectioning microscopy and selective/single plane illumination microscopy (SPIM), light sheet fluorescence microscopy (LSFM) is a technique to image 3D samples where a single plane of the sample is illuminated at a time [130], [131]. The illumination axis is also at 90° of the detection axis, as illustrated in Figure 2-8, resulting in optical sectioning, similar to confocal microscopy [132]. LSFM has shown that, with the proper post-imaging analysis, it can provide a higher spatial resolution than confocal imaging [133]. However, a special mounting for the sample is necessary [132]. Lorenzo *et al*. [134] first showed how live spheroids expressing fluorescent proteins can be imaged over time to observe live cell division inside spheroids. Patra *et al.* [135] used LSFM to observe the formation of lumen-like structures in spheroids made of endothelial and hepatocellular carcinoma cells. Finally, Smyrek *et al*. [110] used LSFM to verify the immunostaining of whole spheroids. A clear advantage of light sheet fluorescence microscopy is the fact that, contrary to confocal microscopy, the image of one optical section done in a single acquisition (no spatial scanning of the surface is necessary). This leads to faster acquisition time. However, the required special mounting of the sample and the necessary optical quality of the illumination plane limit the field of view size under 1 mm^2, limiting the number of samples that can be imaged in a single acquisition [16].
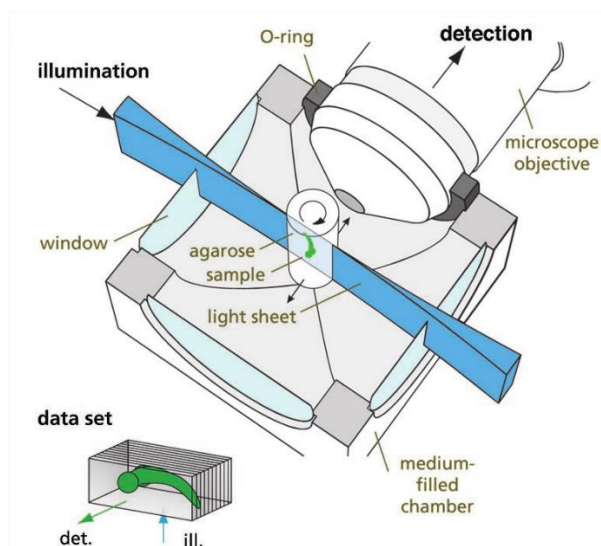
Figure 2-8: Orthogonal single plane illumination and detection in light sheet microscopy. Reproduced with permission from [131].

2.3.2.3.5 Hyperspectral imaging

Hyperspectral imaging is a technique where spectral information is also acquired at each pixel of the image. It has been extensively used in the field of remote sensing [136] and food safety [137], but is relatively new in biological sciences [138]. Hyperspectral imaging can be distinguished from multispectral imaging by the number and position of the spectral bands acquired. In multispectral imaging, only select bands are acquired, while hyperspectral imaging has the goal of measuring the full sample spectrum at specific wavelength-interval. By acquiring the spectral information of the sample studied, a spectral unmixing can be done to separate the contribution of the spectral entities present in the sample, such as fluorescent markers, endogenous fluorophores, tissue absorbers (hemoglobin, melanin) and scatterers (cell membrane, subcellular organelles) [139]. Figure 2-9 illustrate a hyperspectral datacube acquired on a single layer of fluorescent beads and the corresponding spectral unmixing.
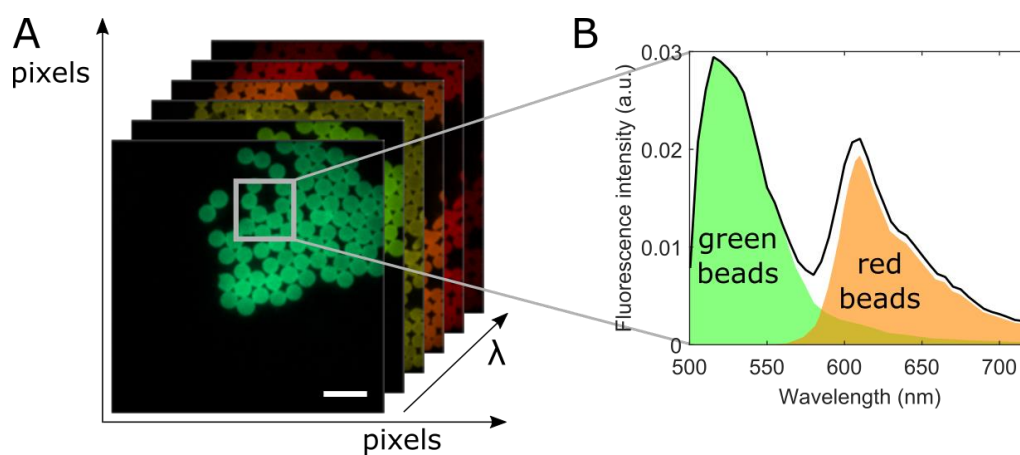
Figure 2-9: Fluorescence hyperspectral imaging. A) Datacube acquisition of two types of fluorescent beads in a single layer. B) Average fluorescence spectrum from the pixels located in the gray square. Linear unmixing can be used to separate the green and red beads.

Different acquisition mode can be used to perform HSI: wavelength scanning, spatial scanning (point or line), and snapshot acquisition (no scanning), as illustrated in Figure 2-10. Each mode has its advantages over the spectral resolution possible and the acquisition speed. For example, a point-scanning HSI system can use a highly spectrally resolved spectrometer to analyze the light dispersed from a single pixel of the image using a diffraction grating. While scanning each point of the sample can be long, the measured spectrum is highly resolved. In this dissertation, the HSI

system built uses a wavelength scanning mode, to simplify the imaging system setup, as no sample-scanning motors are necessary.
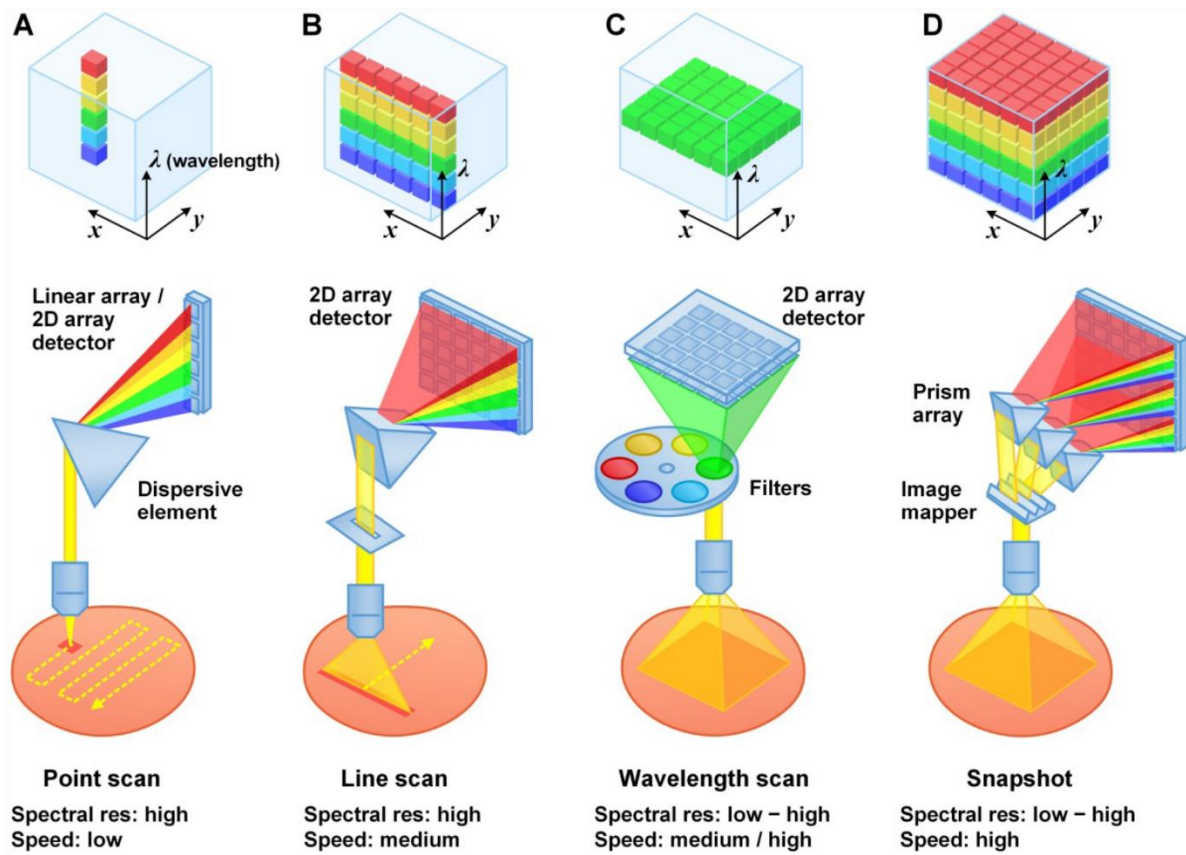
Figure 2-10: Hyperspectral imaging approaches: A) Point scan; B) line scan; C) wavelength scan; D) snapshot. Reproduced with permission from [140] (CC BY-NC 4.0).

HSI has been used for many applications. Lu *et al*. [139] published an excellent review in 2014 detailing many of the contrast used to study various diseases with HSI. Briefly, HSI systems can be separated into two main categories: reflectance- and transmittance-based. Each category can be further separated by the contrast method used: intrinsic or external absorbers and scatterers or intrinsic or external fluorophores. Pichette *et al*. [141] used a snapshot camera through a surgical microscope to image reflectance-based changes in oxygenated hemoglobin (intrinsic absorber) at the surface of the brain. Renkoski *et al*. [142] imaged the autofluorescence (intrinsic fluorophore) of resected human ovaries to identify cancerous regions. Finally, Bravo *et al*. [143] described the advantages of using HSI to guide surgical resection using aminolevulinic-acid (ALA) induced protoporphyrin IX (PpIX) fluorescence (external fluorophore). ALA-based fluorescence guided surgery is explained in more details in section 2.4.1. Transmittance-based methods are currently

more applied to food safety and imaging of thin tissue slices. HSI can be used to identify defects or contaminants inside food, as Huang *et al*. [144] showed in their study designed to identify insect-damaged soybeans (intrinsic absorbers and scatterers). Guan *et al*. [145] used transmittance measurements (intrinsic absorbers and scatterers) to segment pathological leucocytes from other cells. Many studies also used transmittance HSI to image histology slides containing tissue slices (circa 4 µm-thick). For example, Bautista *et al*. [146] used HSI to image Hematoxylin and eosin stained slides (external absorber) to calculate and simulate other types of staining, such as Masson's trichrome staining.

The trade-off for acquiring spectral data during image acquisition is usually longer acquisition times, due to the necessary scanning. Therefore, snapshot hyperspectral cameras are ideal to do video-rate acquisition in real-time. Also, filters used to perform wavelength-scanning can have low transmission rates and require longer acquisition times. This can make acquiring fluorescence spectra of small samples or wide fields of view difficult [138].

Few research groups used HSI to study whole spheroids and none of spheroids in microfluidic chips and in a high-throughput manner. Jena *et al*. [147] imaged live spheroids with near-infrared hyperspectral imaging to study the permeability of tumour spheroids in well plates to photoluminescent carbon nanotubes. HSI was also performed on single cells in microfluidic channels by Caprio *et al*. [148] and Horton *et al*. [149]. Jahr *et al*. [150] modified a light sheet fluorescence microscope to acquire hyperspectral images of zebrafish and fruit fly embryos.

2.4 Fluorescence quantification

In the previously described imaging modalities, the detected fluorescence intensity is a function of the fluorophore concentration in the sample. However, it is also a function of the sample optical properties [151]. Taking optical properties into account is one of the challenges associated with 3D sample imaging. During the observation of a 2D culture, for example, the excitation light arrives directly to the cell monolayer and the emitted fluorescence exits the cells and reaches the detector without passing through other cells. In the case of 3D cultures, a fluorophore placed inside the sample will see its excitation light absorbed and scattered by the peripheral cells as well as for the fluorescence that it emits. Optical properties must be taken into account to correctly measure amount of each fluorophores in the sample. The properties to consider are absorption, μ_a, and

scattering, μ_s', at the excitation and emission wavelengths of the fluorophore. As an example, Figure 2-11 presents the measured fluorescence intensity of 9 cylindrical samples. Each sample contains the same number of fluorophores but varying optical properties. From sample C to sample G, a four-fold intensity decrease was measured by Kim *et al*. [152]. For these samples and their optical properties, the emitted fluorescence intensity cannot be used to measure the fluorophore concentration unless a four-fold error is acceptable.
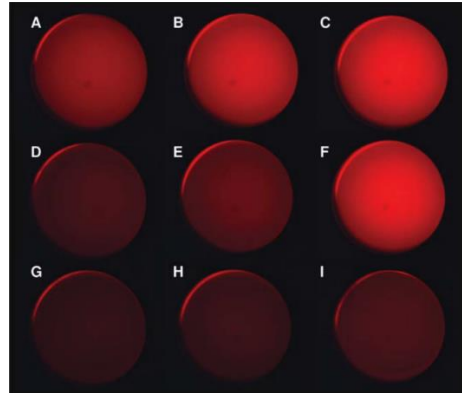
Figure 2-11: Fluorescence from phantoms with varying optical properties, but the same protoporphyrin IX (PpIX) concentration. Reproduced with permission from [152].

Methods have been developed to compensate for the optical properties of a 3D sample and quantify its fluorescence correctly. Optical phantoms of known optical properties and fluorophore concentration are typically used to validate the quantification methods. Optical phantoms are sample-simulating material whose optical properties can be controlled. In this dissertation, optical phantoms were used to validate the quantification algorithm presented in section 4.5.3. Typical optical phantoms are composed of a scattering medium (μ_s'), an absorbing medium (μ_a), and the fluorophore of interest. For example, lipid emulsions (Intralipid®), oxides such as TiO_2, Al_2O_3, and SiO_2, or microspheres can be used as scattering agents. Absorbing agents are generally soluble dyes presenting either a flat spectral behaviour, such as India ink, nigrosine, or carbon black, or a specific absorption peak, such as food colouring dyes. Phantoms matrix can be liquid-based (such as water), hydrogel-based (such as gelatin or agar), or solid-based (such as resins like polyester, and polyurethane, or silicone rubber) [153].

2.4.1 Quantification techniques

Several quantification techniques were developed and are reviewed by Bradley *et al*. [154]. Briefly, techniques can be theory-, measurement-, or empirically-based. Each technique will be valid for a specific set of μ_a and μ_s' values, due to the hypotheses needed to develop the technique.

Theory-based techniques use the fact that light propagation can be described by the radiative transfer equation, which describes how a light beam can gain energy from scattering towards the beam and other light sources and lose energy through absorption and scattering away from the beam by the medium. Various approximations of this equation can then be used depending on the scattering and the absorption of the sample to simplify the resolution of the equation.

The second technique is based on experimentally and explicitly measuring the optical properties of the sample, μ_a and μ_s', and using those values in a model. Kim *et al*. [152] hypothesized that the absorption of a tissue is higher at the excitation wavelength than at the emission wavelength and derived an equation describing the fluorescence intensity depending on μ_a at the excitation wavelength and the reflectance of the sample at both the excitation and the emissions wavelengths. Using their previously developed instrumental method of measuring μ_a and μ_s' with an optical fibre probe, they validated that their point probe method could quantify fluorescence correctly using phantoms and *ex vivo* measurements of mouse tissue.

The third technique uses empirically validated equations to quantify the fluorescence emitted by a sample. Equations are usually based on using the reflectance or endogenous fluorescence spectrum of the sample. The equation is optimized and validated using optical phantoms of known optical properties. For example, Valdés *et al*. [155] divided the measured fluorescence spectrum by the reflectance value at the excitation and at the emission spectrum to quantify PpIX fluorescence in tissues. This technique was used in this work and is further described in section 3.2.

CHAPTER 3   GENERAL METHODOLOGY

This chapter presents the general methodology used in both articles included in this dissertation. The methodology is presented in relation to each research objective. The relation between the articles and each research objective is also stated.

3.1 Development of a wide-field hyperspectral imaging system for spheroid analysis

Objective 1: Design and build a wide-field hyperspectral imaging system to measure non-destructively the fluorescence emitted by co-culture spheroids cultured in microfluidic chips.

The first objective of this work was to design and build a wide-field hyperspectral imaging system to measure spheroid fluorescence. The HSI system is based on the use of a liquid crystal tunable filter (LCTF) to acquire hyperspectral data cubes by wavelength-scanning from 500 to 720 nm to acquire images at every 5 nm, building the transmittance and fluorescence spectra of the spheroids. The system is presented in detail in Article 1, section 4.5.1. Briefly, a Köhler illumination setup was implemented in one illumination branch to illuminate the sample from below with a white light source. A second illumination branch was designed to excite the sample uniformly with a supercontinuum laser. This excitation laser was used for a more versatile imaging system, allowing the user to choose the excitation wavelength between 400 and 700 nm. The two illumination branches were then combined towards the sample using a beamsplitter. The system was also designed to be wide-field (7.25 mm-diameter field of view) to image the multiple spheroids trapped in the microfluidic chip in a single acquisition; increasing the statistical relevance of the results by acquiring multiple replicates easily. The combination of the wide field of view and the low transmission of the tunable filter required the use of a highly sensitive camera to acquire the spheroid fluorescence images at each wavelength. A thermoelectrically cooled EMCCD camera designed for low light imaging was selected. A custom Labview program was then used to acquire the hyperspectral datacube (one image per wavelength) and control the white light automatically. Article 1, section 4.5.2 describes the different types of acquisition necessary to measure spheroid fluorescence. Then, a custom algorithm, detailed in Article 1, section 4.5.3, applied a series of calibration steps to the hyperspectral datacubes. Each spheroid's fluorescence was also

automatically extracted by determining regions of interest in the image corresponding to a spheroid. Two types of sample holder were designed for the HSI system, as illustrated in Figure 3-1. The sample holder was originally designed to hold 25 x 75 mm^2 glass slides and was used here to hold microfluidic chips of a similar size. The second sample holder was designed and fabricated with help by student Tien Nguyen and technician Jean-Paul Lévesque to hold well plates. With this second sample holder, 3D samples cultured in 6- to 384-well plates, such as prostate tubules structures, can be imaged.
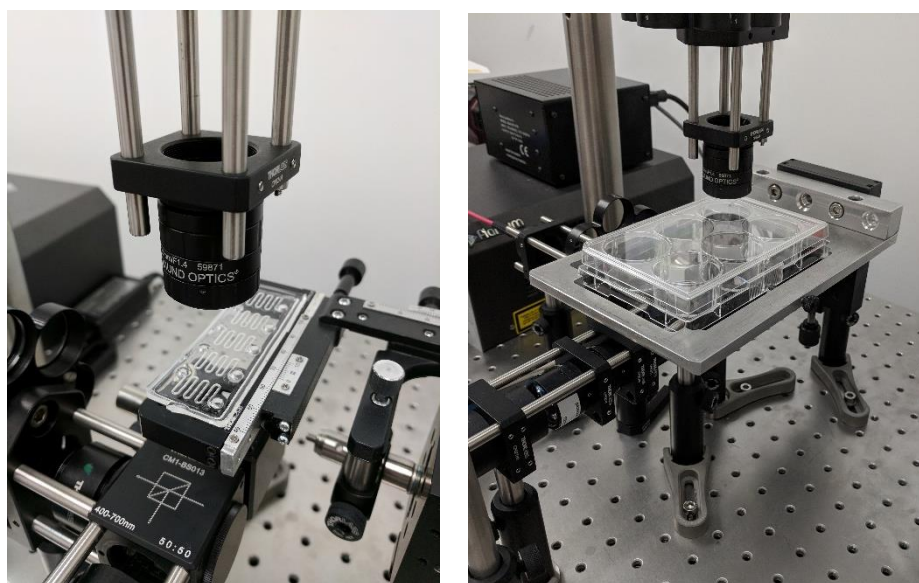
Figure 3-1: A) Sample holder for glass slides or microfluidic chips of similar size. B) Sample holder for well plates.

3.2 Validation of the fluorescence quantification capabilities of the HSI system

Objective 2: Validate the hyperspectral imaging system and evaluate the ability of image analysis algorithms to quantify fluorescence, sampling up to the spheroid centre, and measure spheroid composition in co-culture spheroids.

Objective 2 was fulfilled by first validating the capacity of the HSI system to extract and quantify fluorescence from the effect of the sample optical properties. One of the main advantage of using hyperspectral imaging to image fluorescent samples is utilizing the higher spectral resolution to

measure the reflectance or transmittance spectrum of the sample. This spectrum can then be used to quantify the sample fluorescence. The fluorescence intensity measured at the camera will depend on the number of fluorophore molecules and its scattering and absorbing properties. Empirical-based algorithms can be used to compensate the optical properties effect using the transmittance of the sample. The technique used in this dissertation for measuring the concentration of fluorophores in 3D samples is based on Valdés *et al.* work [155]. This technique corrects the fluorophore emission spectrum of a semi-infinite tissue using the white light reflectance spectrum according to the following equation:

$$\Phi(\lambda) = \frac{\Phi^{\text{Fluo}}(\lambda)}{\Phi_x^{\text{Ref}} \times \left(\Phi_m^{\text{Ref}}\right)^\alpha} \tag{3-1}$$

where $\Phi(\lambda)$ is the quantified fluorescence spectrum, $\Phi^{\text{Fluo}}(\lambda)$ is the raw fluorescence spectrum, Φ_x^{Ref} et Φ_m^{Ref} are the integrated reflectance spectra at the excitation (x) and emission (m) range of wavelengths, and α is an empirical parameter specific to the sample geometry, fluorophore imaged and optical system used. Figure 3-2 shows how the quantification algorithm works. Before any fluorescence quantification (A), fluorescence levels for a specific fluorophore concentration vary depending on the optical properties of the sample. After quantification (B), optical properties are compensated for and fluorescence intensities only depend on the fluorophore concentration. This technique is only valid for the range of μ_a and μ_s' tested with optical phantoms and any changes to the sample geometry of the imaging system will require a new phantom validation.

A

$$\Phi^{Ratio}(\lambda) = \Phi^{Fluo}(\lambda)$$

B

$$\Phi^{Ratio}(\lambda) = \frac{\Phi^{Fluo}(\lambda)}{\Phi_x^{Ref} \times \left(\Phi_m^{Ref}\right)^{\alpha}}$$
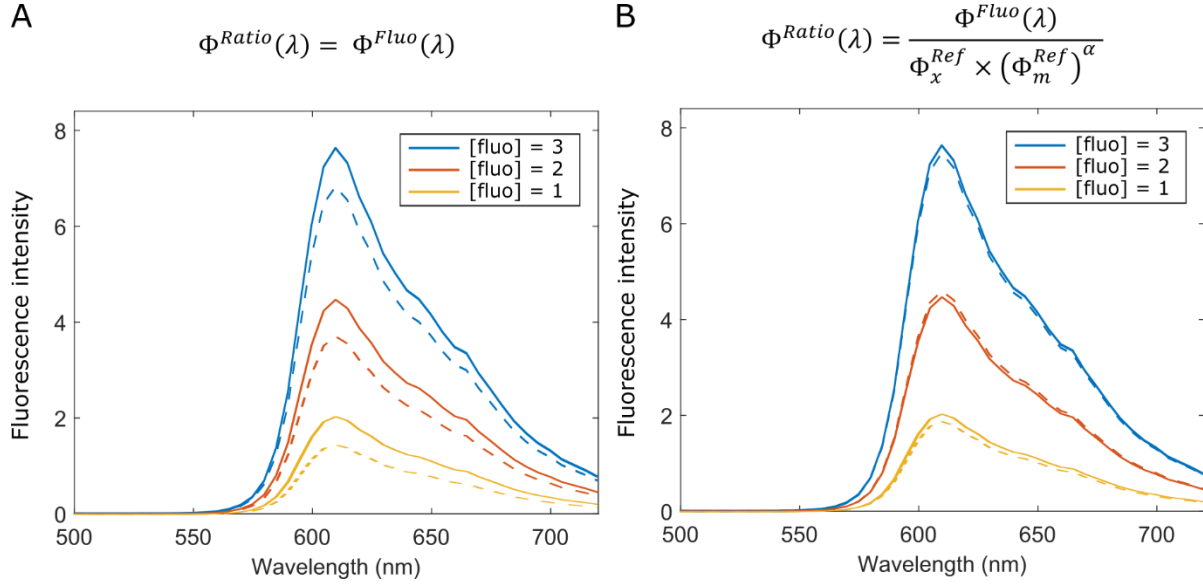
Figure 3-2: Fluorescence quantification algorithm from Valdés *et al*. [155] demonstration. A) Raw fluorescence where each colour represents a fluorophore concentration. Solid and dotted lines represent the optical properties effect on the measured fluorescence. B) Quantified fluorescence where optical properties do not affect the fluorescence intensity for a specific fluorophore concentration.

In this thesis work, equation (3-1) was modified to consider the transmittance of the sample, as described in Article 1, section 4.5.3. Optical properties of spheroids were estimated from Hargrave *et al*. [156] and Wallace *et al*. [157] and Intralipid® [158] was selected as the scattering medium. While the composition of Intralipid®, a lipid emulsion, differs from the composition of spheroids, cells, using a stable lipid emulsion to fabricate an artificial spheroid sample allows for precise control of its optical properties. By varying the scattering coefficient of the optical phantoms around the estimated value of spheroids, the range of values at which the quantification algorithm is valid can be determined. No absorbers were included as spheroids do not present strong absorption such as hemoglobin. The fluorophore of interest, enhanced Green Fluorescent Protein (eGFP), was simulated using dissolved fluorescein, since eGFP and fluorescein excitation and emission peaks are similar. Each phantom was then imaged using the HSI system after introducing them one at a time in a 1 mm-pathlength cuvette. The phantom hyperspectral datacubes were processed with the Matlab algorithm described previously with and without the final fluorescence quantification step. This algorithm to quantify fluorescence was validated with optical phantoms of a planar geometry (small height and large width). While it was able to quantify these phantoms

fluorescence, as shown in Article 1, it cannot be directly transferred to samples of spherical geometry, as one algorithm parameter depends on the sample geometry. Preliminary experiments were done to form spherical optical phantoms: a microfluidic chip was designed to form hydrogel beads of 300 μm in diameter and tested by forming beads containing a scatterer. These results are presented in Appendix A.

A second type of validation of the HSI system was done using a Monte Carlo simulation platform. The goal was to validate if the HSI system could sample the drug response at the spheroid centre, as it is a challenge in other types of microscopy. The HSI system geometry as well as the spheroid geometry were implemented in a Monte Carlo light propagation simulator and the trajectory of fluorescence excitation and emission photons were simulated. Preliminary results of this validation are presented in Appendix B.

Finally, the HSI system and the image analysis algorithm capacity to measure the composition in cell population of co-culture spheroids was validated with the gold standard, flow cytometry. Co-culture spheroids made from two fluorescent cell lines were formed and cultured in microfluidic chips. Different ratios of the two cell lines, from only green fluorescent cells, to 50% of each, and to only red fluorescent cells, were used to form the spheroids. Microfluidics chips containing the spheroids were first imaged using the HSI system. Immediately after, the same spheroids were harvested from the chips, digested into single cells, and analyzed using flow cytometry. Spheroid compositions as a percentage of each cell population measured by each technique were then compared and results are detailed in Article 2, section 5.4.3.

3.3 On-chip hyperspectral imaging of co-culture spheroids to study clonal heterogeneity

Objective 3: Study clonal heterogeneity in ovarian cancer by forming co-culture spheroids and follow their response to chemotherapy treatments on-chip over time.

Two microfluidics chip designs were used in this dissertation and are represented in Figure 3-3. The chips were designed by Mélina Astolfi [44] (chip A) and Bishnubrata Patra [72], [159] (chip B) with the ease of use by biologists in mind, an important factor determining the adoption

of the technology by research biologists [160]. They are composed of a single channel and either 5 or 120 wells, fluids are introduced and removed using micropipettes, and no pumps are necessary.
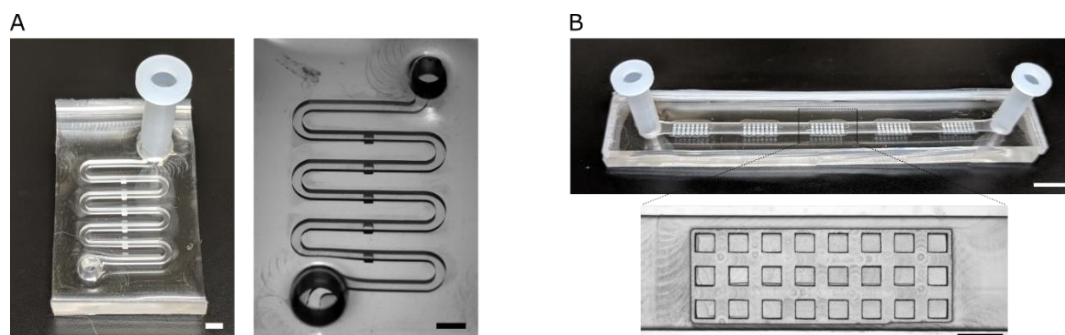
Figure 3-3: Microfluidic chips used throughout this dissertation. A) Microfluidic chip A was designed to trap microtissues in 5 gravitational traps. Scale bars = 2 mm. B) Microfluidic chip B was designed to form and trap 120 spheroids on chip in 5 groups of 24 spheroids. Scale bars = 6 and 1 mm.

To study the treatment response of co-culture spheroids, several ovarian cancer cell lines derived from patients were used during this work. To be able to distinguish them in spheroids, cell lines were genetically modified to express either a green or red fluorescent protein by Adriana Mari Orimoto and Maxime Cahuzac. In most experiments, microfluidic chip B was used to form 120 spheroids made from a single cell suspension or from various ratios of two cell lines (100:0, 90:10, 75:25, 50:50, 25:75, 10:90, 0:100). Two days after formation, spheroids were either cultured over time or exposed to chemotherapy treatments (platinum-based or PARP inhibitor). Medium was changed daily to replenish the available nutrients and remove cell waste. Because HSI is a non-destructive technique, spheroids were imaged daily, and each population fluorescence was followed over time and as a response to treatment. The HSI image analysis algorithm was used to calculate the spheroid composition also over time and as a response to treatment. A proof-of-concept that co-culture spheroid composition can be followed over time using HSI is presented in Article 1. A second set of more complete experiments are presented in Article 2, clearly showing that each population response to external stimuli can be measured individually.

Lastly, a modification to a statistical test was developed to analyze monotonic trends in spheroid-based research. The Mann-Kendall statistical test was already available to identify monotonic trends in a series of data points. However, if the data points consist of an average of multiple experiment replications and the associated error, the test cannot be applied, as it cannot take into

account the errors. Based on work by Soderberg and Hennet [161], I modified the implementation of the test as described in Appendix C. The modified Mann-Kendall test was used by Mohana Marimuthu to confirm that controlling the cell seeding density while forming spheroids on-chip led to a monotonic increase as the cell number increases [78].

CHAPTER 4   ARTICLE 1: FLUORESCENCE HYPERSPECTRAL IMAGING FOR LIVE MONITORING OF MULTIPLE SPHEROIDS IN MICROFLUIDIC CHIPS

A. St-Georges-Robillard,[1,2,3,4] M. Masse,[1] M. Cahuzac,[3,4] M. Strupler,[1] B. Patra,[1,3,4] A. M. Orimoto,[3,4] J. Kendall-Dupont,[3,4] B. Péant,[3,4] A.-M. Mes-Masson,[3,4,5] F. Leblond[1,2,3] and T. Gervais[1,2,3,4]

[1] Department of Engineering Physics, Polytechnique Montréal, C.P. 6079, Succ. Centre-ville, Montreal, Qc, H3C 3A7, Canada.

[2] Institut de génie biomédical, Polytechnique Montréal, C.P. 6079, Succ. Centre-ville, Montreal, Qc, H3C 3A7, Canada.

[3] Centre de recherche du Centre hospitalier de l'Université de Montréal, 900 St-Denis St., Montreal, Qc, H2X 0A9, Canada.

[4] Institut du cancer de Montréal, 900 St-Denis St., Montreal, Qc, H2X 0A9, Canada.

[5] Department of Medicine, Université de Montréal, 2900, boul. Edouard-Montpetit, Montreal, Qc, H3T 1J4, Canada

4.1 Background information

Published article 1 [159] is presented in this chapter and discuss the hyperspectral imaging system design and its image analysis algorithm. This article details the methodology in terms of image acquisition and processing used throughout this dissertation. The optical design and the image acquisition sequence used in the subsequent image analysis steps are first presented. The HSI system was then characterized in terms of spatial resolution and shading correction performance. The system performance to quantify fluorescence from the sample optical properties was then studied using optical phantoms of known fluorophore concentrations and optical properties. Finally, two imaging experiments were performed to illustrate the HSI system capabilities to do wide-field imaging of 3D cultures. First, spheroids made from two fluorescent cell lines were formed using the hanging droplet method and loaded in a first microfluidic chip. In a second experiment, co-culture spheroids were formed directly on-chip using a second chip design and their growth was followed over time to assess the proliferation of each cell population.

My contribution for this article is 80% of the work. I designed, build, and calibrated the HSI system and wrote its image analysis algorithm. I performed and analyzed the phantom experiment validation and most of the spheroid cell culture and hyperspectral imaging. I wrote the article, except the Experimental section 4.5.7 describing the confocal imaging. M.M helped during his internship to test the imaging system and optimize distances between lenses. M.C. generated the mCherry-OV1946 clone. M.S. helped design the brightfield illumination branch of the system. B.Patra designed microfluidic chip B. A.M.O. generated the eGFP-OV1946 and mCardinal-OV90 clones and formed the co-culture spheroids using the hanging droplet method. J.K.D. performed the confocal imaging. B.Péant helped design the second co-culture experiment. A.-M.M.-M., F.L., and T.G. provided support and supervised the research.

The article was submitted on March 22nd, 2018 and accepted on June 27th, 2018 in *Analyst*, volume 143, issue 16, pages 3829–3840. The article is reproduced from [159] with permission from The Royal Society of Chemistry.

4.2 Abstract

Tumor spheroids represent a realistic 3D *in vitro* cancer model because they provide a missing link between monolayer cell culture and live tissues. While microfluidic chips can easily form and assay thousands of spheroids simultaneously, few commercial instruments are available to analyze this massive amount of data. Available techniques to measure spheroid response to external stimuli, such as confocal imaging and flow cytometry, are either not appropriate for 3D cultures, or destructive. We designed a wide-field hyperspectral imaging system to analyze multiple spheroids trapped in a microfluidic chip in a single acquisition. The system and its fluorescence quantification algorithm were assessed using liquid phantoms mimicking spheroid optical properties. Spectral unmixing was tested on three overlapping spectral entities. Hyperspectral images of co-culture spheroids expressing two fluorophores were compared with confocal microscopy and spheroid growth was measured over time. The system can spectrally analyze multiple fluorescent markers simultaneously and allows multiple time-points assays, providing a fast and versatile solution for analyzing lab on a chip devices.

4.3 Introduction

Interest in multicellular tumor spheroids (MCTS, or spheroids) as a 3D *in vitro* cancer model has been steadily growing in the past decade [40]. They represent a realistic 3D cell culture model with properties that bridge the gap between monolayer cell culture and live tissues, including human biopsies, surgical specimens, or mouse xenografts [4], [162]. MCTS are 3D constructs made of cells that aggregate together to form spheres of varying compactness. Contrary to monolayer (2D) cell culture, they display cell-cell and cell-matrix interactions [4]. Tumor cell lines are often able to spontaneously form these 3D constructs when cultured in hanging droplets, low-attachment plates or passivated microfluidic chips [57].

The microfluidics community has put considerable effort in the past ten years to develop chip-based platforms capable of forming and/or testing MCTS [40], [45], [59], [65], [66], [70], [71], [81], [125], [163]. Some of them can be used to synthesize thousands of spheroids in one step [104], [164]. Others can be used to form spheroids of different sizes utilizing a single cell suspension [78]. They can also hold (or trap) spheroids in place during medium changes or while adding/removing reagents without the risk of pipetting them out, an issue often encountered when manipulating spheroids with micropipettes in 96-well plates [73], [74], [76].

Still, microfluidic chips are not yet fully adopted by research biologists, one of the main reasons being the complexity of use. Many microfluidic chips are designed to perform experiments efficiently but need complex pumping systems or handling [160]. Also, while microfluidic chips are able to easily produce large amounts of spheroids, very few commercial applications exist to analyze this massive amount of data. Typical techniques used by researchers consist of confocal, two-photon, and light sheet microscopy, and flow and imaging cytometry. Confocal microscopy is often used in conjunction with live/dead fluorescent markers to count the numbers of viable cells compared to dead cells in a spheroid [89], [125], [165], [166]. Mohapatra *et al*. acquired spheroid fluorescence emission spectra for whole optical sections during confocal imaging [126]. While this technique offers high resolution imaging and spatial information on spheroid viability, it is limited to the first few cell layers (50-100 µm) due to limited light penetration in the 3D culture. Imaging larger fields of view also requires multiple acquisitions and image stitching [44], [121], [122]. Loss of signal-to-noise with imaging depth can prevent accurate measurement of the spheroid center response to a treatment, where necrotic, senescent, or slowly proliferating cells are present [40].

Two-photon and light sheet microscopies circumvent this limitation by using different illumination strategies, albeit with significant drawbacks. While two-photon imaging typically uses infrared excitation to image whole spheroids, its long acquisition time for large volumes and its working distance render the technique difficult to use on multiple spheroids trapped in thick (> 5 mm) microfluidic chips [15]. Light sheet microscopy, in turn, uses structured illumination to excite a single plane in the spheroid but is not adapted to image multiple spheroids in one acquisition [135]. Other researchers have developed lens free microscopy over large fields of view, but the spectral capabilities of their systems are limited to the static (non-tunable) filters used to image fluorescent samples [117].

Flow cytometry is also used to analyze cell populations in spheroids using fluorescent markers [44], [104]. Spheroids are first digested into a single cell suspension and each cell is analyzed one at a time using fluorescence-activated cell sorting (FACS). This technique can precisely measure the proportion of cells marked by each fluorescent marker since it analyzes each cell individually. Because of the necessary spheroid digestion, FACS is a destructive analysis technique. No spatial information is obtained, contrary to confocal microscopy, and the same sample cannot be analyzed at multiple time-points. Image cytometry instruments are starting to be available for spheroid analysis [103], but they lack the spectral resolution necessary to separate more than a few fluorophores or perform fluorescence quantification.

Wide-field fluorescence spectroscopy, seldom used in the context of 3D cell culture or microfluidics, holds several advantages that could improve spheroid analysis, namely its higher spectral resolution and its wide-field capability to image multiple samples in one acquisition. Wide-field quantitative fluorescence imaging is currently used in surgical guidance to identify residual tumors during cancer resection [167], [168]. However, since tunable filters generally have low transmission in the visible range [138], it is a challenge to design an imaging system with a large field of view while maintaining enough sensitivity to detect the fluorescence emitted by a spheroid.

Here, we report the first use of wide-field fluorescence hyperspectral imaging to accelerate spheroid analysis while they are still trapped in a microfluidic chip. We have designed a wide-field quantitative hyperspectral imaging (HSI) system with the potential to spectrally analyze spheroids using multiple fluorescent markers in a single acquisition and in a non-destructive fashion (Figure 4-1). The HSI system relies on the use of a liquid crystal tunable filter to acquire wide-field

spectroscopic data of a sample with a spectral resolution of 7 nm. Because of its wide-field capability, the system can analyze multiple samples in one acquisition, enabling the study of large numbers of spheroids independently without increasing analysis time exponentially as would confocal imaging or flow cytometry. The system and its image analysis algorithm also use transmittance images of the sample to correct for its optical properties and quantify its emitted fluorescence. The proposed technique is non-destructive; samples can be analyzed at multiple time-points if the fluorescent markers used are not cytotoxic. Also, the higher spectral resolution of the HSI system enables the resolution of a larger number of fluorescent markers than a standard microscope limited by fluorescence filter cubes. Fluorophores with close emission peaks can also be resolved more easily. We also demonstrate how the HSI system can be used to analyze spheroids either made on-chip (using chip B) or made using other methods (such as hanging droplets) and loaded in a microfluidic chip (chip A).
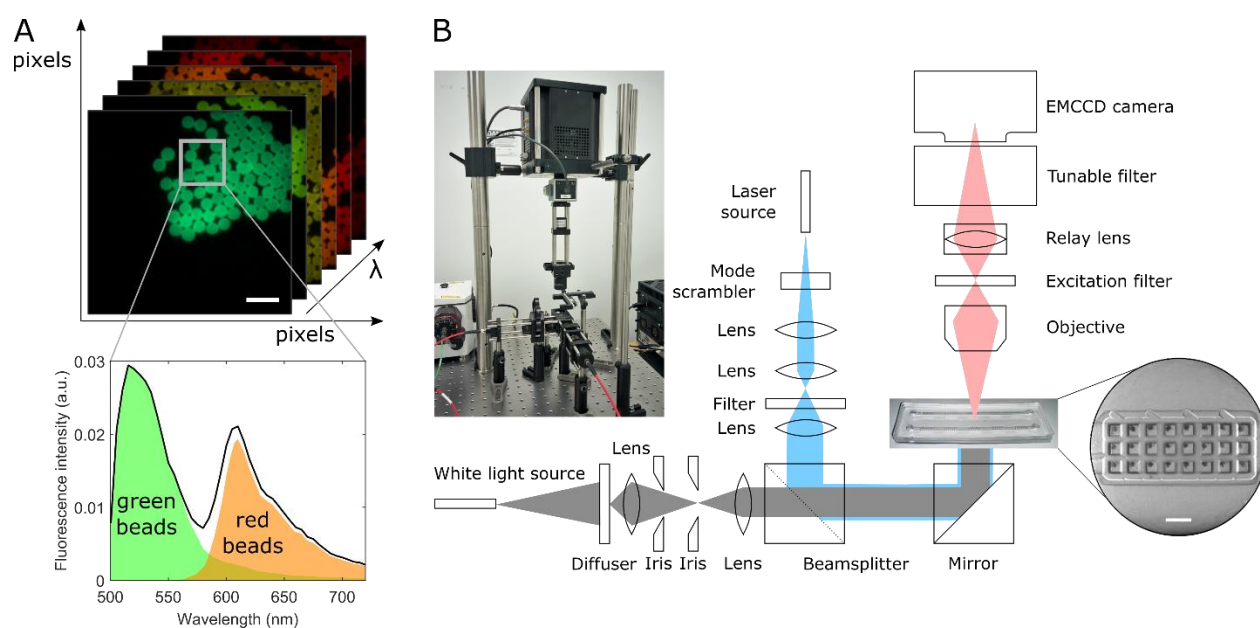
Figure 4-1: Hyperspectral imaging. (A) Concept figure of hyperspectral imaging of a single layer of green and red fluorescent beads and the average spectrum from the pixels inside the gray rectangle. Unit a.u. is for arbitrary units. Scale bar = 1 mm. (B) Hyperspectral imaging system diagram. Circular inset shows microfluidic chip B containing 24 wells where spheroids were formed and trapped. Scale bars = 1 mm. Photograph shows the imaging system.

We further introduce a method to perform fluorescence quantification that is, the number of molecules of a fluorescent dye present in a spatially resolved sample. In general, that information is lost as the scattering and absorption coefficients of the sample imaged affects the fluorescence detected at the camera [151]. A custom fluorescence quantification algorithm was used to decouple the emitted fluorescence from scatterers and absorbers in the tissue using transmittance images, in order to recover the intrinsic sample fluorescence signal. Its performance is demonstrated by imaging calibrated liquid phantoms with optical properties similar to those of spheroids. Wide-field hyperspectral images of fluorescent co-culture spheroids were compared with maximum projections obtained by confocal imaging. Finally, growth curves of two cell populations forming co-culture spheroids were measured over nine days.

Overall, the HSI system is simple to use and displays superior performance when compared in terms of spectral resolution, fluorescence quantification, and analysis time with other methods and suggests that it may form the backbone of future spheroid imaging platforms.

4.4 Results and Discussion

4.4.1 System design and characterization

The custom-built HSI system uses a tunable filter to sweep across the emission spectrum of the fluorescent sample and acquires one image per wavelength. Figure 4-1A shows a concept figure where green and red fluorescent beads were placed in a single layer on a glass slide. By analyzing the emitted fluorescence intensity variations according to the measured wavelength, the beads emission spectrum can be reconstructed and the contribution of each fluorophore, unmixed.

The system is composed of two illumination paths combined towards the sample using a beamsplitter (Figure 4-1B). A tungsten-halogen white light source is used to measure the transmittance spectrum of the sample while a supercontinuum laser filtered using a laser line filter is used to excite the sample fluorescence at the chosen wavelength. An objective and relay lens form the sample's image on a highly sensitive electron-multiplying charged couple device (EMCCD) camera. A liquid crystal tunable filter sweeps across wavelengths to measure the sample transmittance and fluorescence spectra.

To measure the true emitted fluorescence intensity of a sample, precise steps are needed. Figure 4-2. presents an overview of the image analysis steps performed to measure and quantify the fluorescence emitted by a sample, correcting for the sample optical properties and the system response. Each step details are presented in the Experimental section.
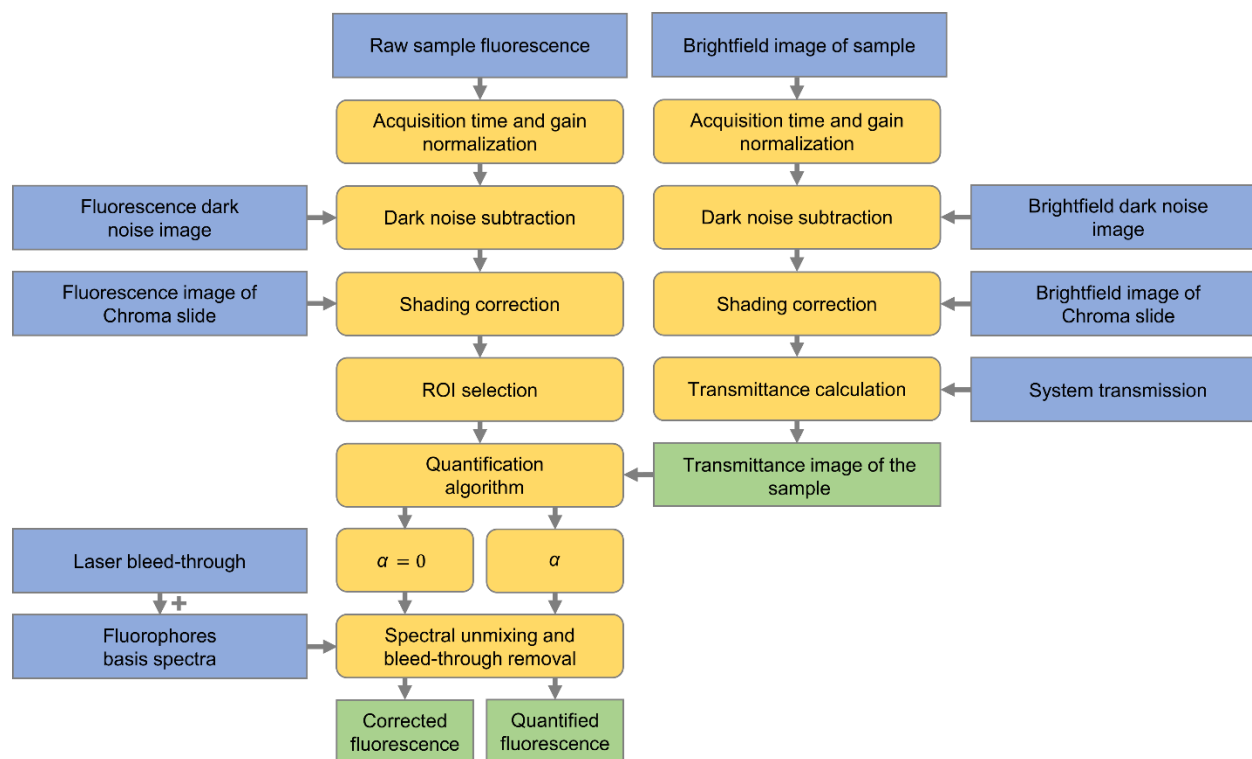
Figure 4-2: Image analysis steps to quantify the fluorescence emitted by the imaged sample using its transmittance measurement. Blue blocks represent experimental input images, yellow blocks represent image analysis steps performed on the acquired brightfield and fluorescence images of the sample, and green blocks represent output results. Details of each step are presented in the Experimental section.

The optical resolution and field of view of the HSI system were first characterized. A 1951 USAF resolution target was used to measure the field of view in both the *x* and *y* directions, yielding a circular field of view of 7.25 mm in diameter (see Figure 4-3A). This field of view is large enough to measure multiple samples in one image. The resolution target was also used to measure the resolution of the imaging system. The smallest element where a contrast difference of more than 27% between a black and a white line can be detected was observed to determine the resolution

(see Figure 4-3B). In both horizontal and vertical axes, the measured spatial resolution is 22.6 line pairs per millimeter.
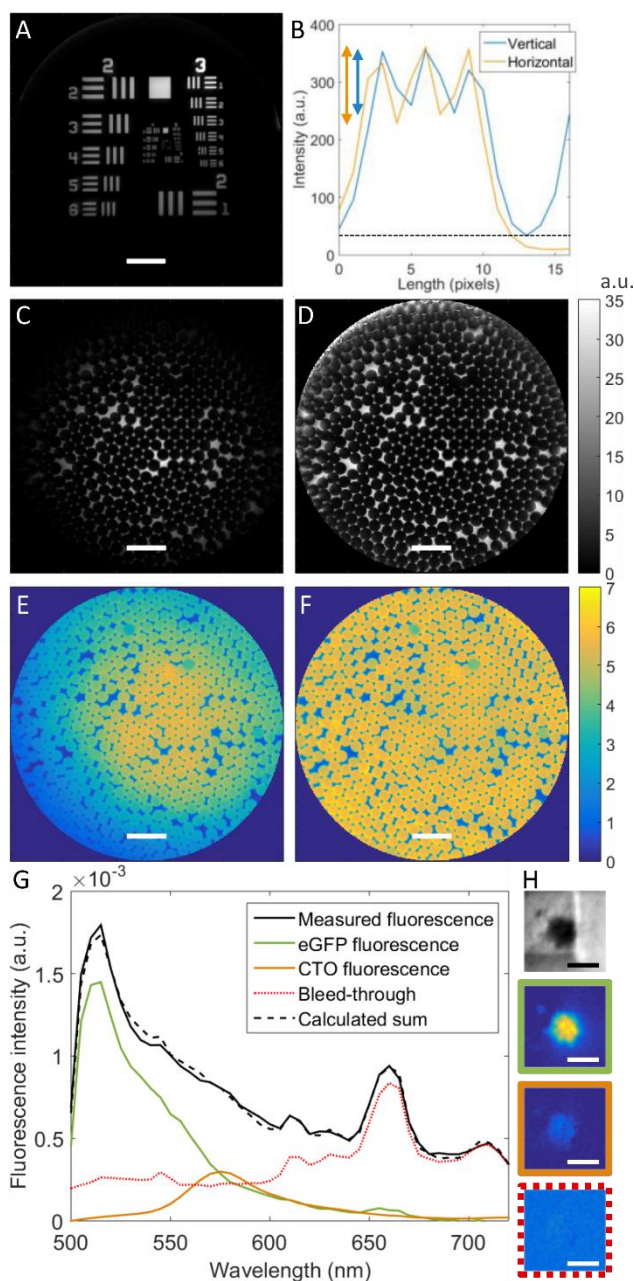
Figure 4-3: System characterization and image analysis steps. (A) Brightfield image (sum of wavelengths between 500 and 720 nm) of a 1951 USAF resolution target. Scale bar = 1 mm. (B) Average intensity profiles horizontally and vertically of the 3 lines of element 4, group 4 of the resolution target. Arrows show that the Rayleigh criterion of > 27% is respected. (C-D) Brightfield (a.u.) (at 720 nm) and (E-F) fluorescence (a. u.) images (at 610 nm) of a single

layer of fluorescent beads before (C;E) and after (D;F) the shading correction. Scale bars = 1 mm. (G) Spectral unmixing of the eGFP and CTO fluorescence from the excitation laser bleed-through in a spheroid. (H) Top figure shows the brightfield image (at 720 nm) of the spheroid. Bottom three figures show the unmixed eGFP fluorescence (green perimeter) and CTO fluorescence (orange perimeter) from the laser bleed-through (red, ⋯ perimeter). Scale bars = 200 µm, a.u. is for arbitrary units.

4.4.2 Fluorescence quantification

The sample fluorescence was quantified with a custom algorithm according to the steps listed in Figure 4-2 and using the different input data cubes described in the Experimental section. Each data cube is first normalized to the acquisition time and the gain of the camera. Figure 4-3C-D shows an example of the shading correction used to correct for uneven illumination and detection responsible for a vignetting effect. The correction is shown here on the brightfield image of a single layer of fluorescent beads with diameters ranging from 300 to 355 µm. Figure 4-3E-F shows the shading correction applied to the fluorescence image of the beads. While the intensity of the beads in the center of the image is clearly higher than in the periphery before the shading correction, the image after shading correction shows that the intensity is uniform. This correction allows intensity comparison of samples located in the center of the image versus the periphery as it compensates for the lower illumination/detection of peripheral samples.

A laser line tunable filter is used in the HSI system to select a specific wavelength for fluorescence excitation. This versatility comes at the cost of small out of band light contamination. An example of excitation laser bleed-through measured when a fluorescent spheroid emitting two fluorophores (enhanced Green Fluorescent Protein, eGFP, and CellTracker™ Orange, CTO) is excited at 500 nm is shown in Figure 4-3G. The spheroid fluorescence intensity (peaks at 515 and 575 nm) is similar to the bleed-through intensity (three peaks around 625 nm). Spectral unmixing is used to remove this bleed-through and to separate the contribution of each fluorophore to the spheroid fluorescence. Because of the varying thickness of the PDMS between samples, the intensity of the excitation laser bleed-through varies and cannot be simply subtracted. Here, the spectral unmixing algorithm considers the spectral shape of the bleed-through to be removed (see Figure 4-3G). Hyperspectral images in Figure 4-3H illustrate the removal of the bleed-through from a region of interest containing an eGFP-expressing and CTO-stained spheroid loaded into a well of

microfluidic chip A (see Experimental section for the details on the two microfluidic chips used throughout this work). Because of the low intensity of CTO fluorescence compared to eGFP, it would be impossible to detect CTO with a conventional fluorescence microscope. Figure 4-3G-H shows how it was possible to use the HSI system and spectral unmixing to separate the CTO contribution from the eGFP fluorescence and illustrates the potential of hyperspectral imaging in spheroid-based research.

The fluorescence quantification performance of this imaging system was verified using liquid optical phantoms mimicking the optical properties of tumor spheroids. Here, since spheroids do not contain strong absorbers, such as hemoglobin, their absorbance is found to be negligible compared to their scattering coefficient [156], [157]. The fluorophore of interest expressed by the eGFP modified cells used to make spheroids was simulated using fluorescein diluted in a 0.1 M TRIS-HCl (Tris(hydroxymethyl)aminomethane hydrochloride) buffer at pH 8. This buffer and pH were selected to position fluorescein's maximum emission peak at 514 nm when dissolved. Lipid emulsion Intralipid® 20% was used to simulate the scattering properties of spheroids [158]. Thirty phantoms were fabricated, introduced in a 1 mm-pathlength optical glass cuvette and their fluorescence was measured using the HSI system. The fluorescence images of each phantom were then analyzed to find the best α (see equation (4-1)) to quantify the fluorescence, similar to what Valdés *et al.* presented in their work [155]. Figure 4-4A shows the corrected fluorescence intensity at 515 nm of optical phantoms with varying fluorophore concentrations, [*F*], and reduced scattering coefficients, μ_s'. The images shown are those obtained after performing all image analysis steps using $\alpha = 0$ to measure the corrected fluorescence of the phantom without any quantification. As the fluorophore concentration increases, the detected fluorescence intensity increases linearly, as expected. Similarly, as the reduced scattering coefficient increases, the detected fluorescence intensity also increases, while the transmittance of the phantom decreases (Figure 4-4B). Figure 4-4C shows the quantified fluorescence images of each fluorophore where, for a specific fluorescein concentration, the quantified fluorescence is the same.
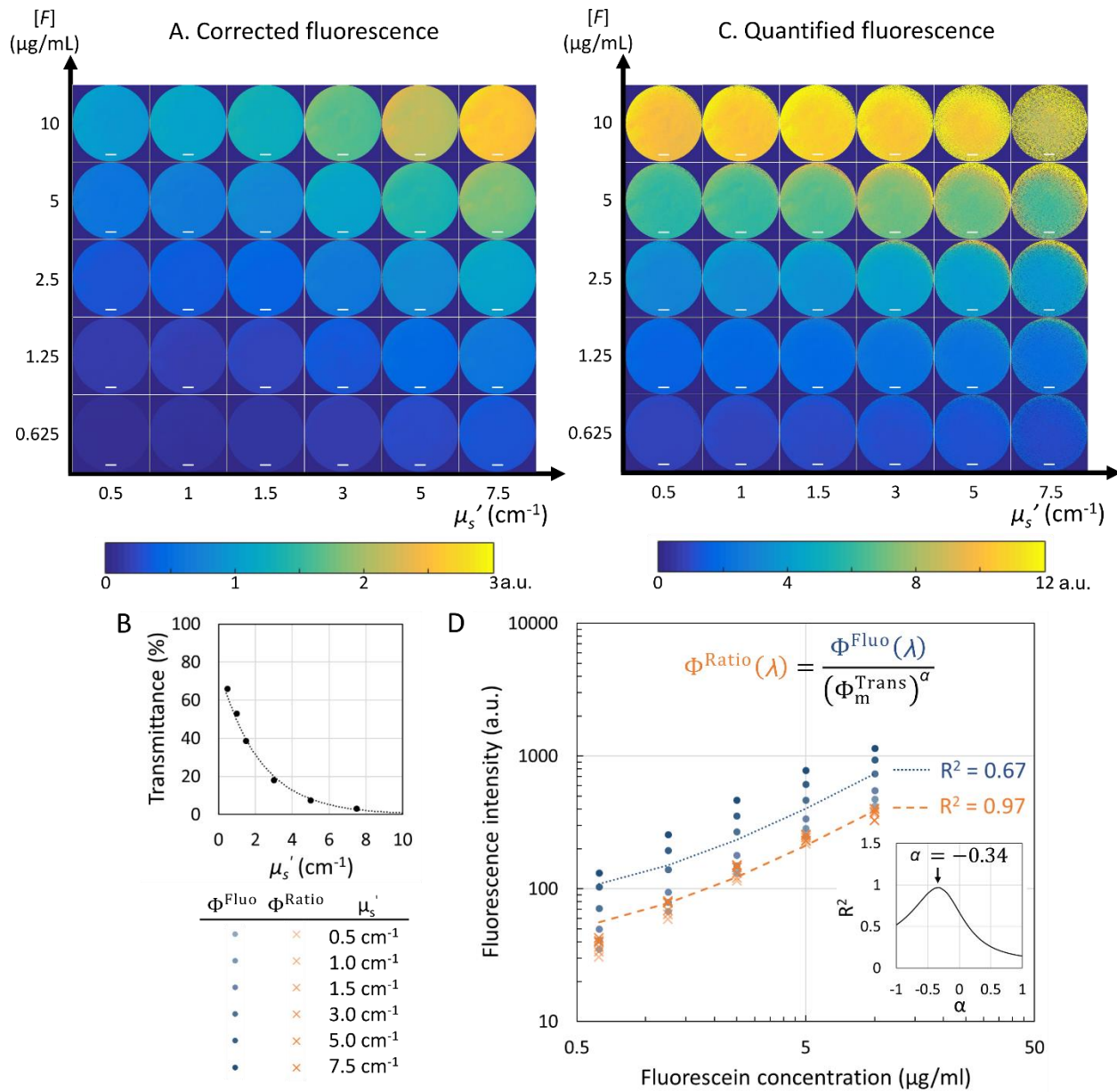
Figure 4-4: Optical phantom experiment. (A) Corrected fluorescence intensity images for 30 phantoms. (B) Mean transmittance of the phantoms with equal μ_s' values. Error bars (± standard deviation) are smaller than the size of the markers. (C) Quantified fluorescence intensity images of the same 30 phantoms. (D) Fluorescence quantification algorithm's performance to compensate for varying scattering coefficients. Raw fluorescence (blue, ●) and quantified fluorescence (orange, x) for μ_s' varying from 0.5 to 7.5 cm⁻¹. 7.5 cm⁻¹ corresponds to the most saturated blue and orange while 0.5 cm⁻¹ corresponds to the least saturated blue and orange. Insert shows

the optimization of the geometry parameter α in relation to R^2. Scale bars = 1 mm, a.u. is for arbitrary units.

The phantom or imaged sample geometry will affect the fluorescence intensity measured at the camera by an imaging system in transmission mode. Here, as the scattering coefficient of the phantoms is increased, their transmittance also decreases. Meanwhile, the measured fluorescence increases. This seems counter-intuitive, as one could think the more scattering the sample is, the more light will be scattered away from the camera. Our results can be explained by a greater number of photons trapped inside the sample at higher concentrations of scatterers, yielding a higher amount of excited fluorophore molecules and a higher detected fluorescence intensity at the camera. This observation highlights why the geometry of the optical phantom used to mimic the biological specimen is important.

Figure 4-4D shows the fluorescence intensity summed from 500 to 720 nm of a square region of interest of 6 by 6 pixels selected in the middle of the images. Corrected fluorescence ($\alpha = 0\alpha = 0$) and quantified fluorescence ($\alpha = -0.34$) are presented. The insert in Figure 4-4D shows the optimization of the geometric quantification factor $\alpha\alpha$. The large dispersion of corrected fluorescence intensity values prevents accurate fluorescence quantification ($R^2 = 0.67$ for a linear fit) while quantified fluorescence yields a linear fit where $R^2 = 0.97$.

For phantoms where $\mu_s' = 7.5$ cm^{-1}, noise is introduced into the quantified fluorescence images because of the low transmittance of the sample, illustrating the limit of this method for fluorescence quantification at very low transmittances. This phantom experiment also shows how transmittance of finite phantoms can also be used to quantify fluorescence, similarly to how reflectance is used in the case of semi-infinite phantoms or tissues [154].

4.4.3 Imaging co-culture spheroids

The system's performance in fluorescence imaging of 3D biological samples was first tested by comparing hyperspectral and confocal images of the same spheroids. Spheroids were made using the hanging droplet method [11] and different ratios of eGFP-OV1946 cells and mCardinal-OV90 cells and then loaded in chip A (Figure 4-5A). Spheroids were first imaged using confocal microscopy followed by hyperspectral imaging and regions of interest are presented in Figure 4-5B. Visual comparison shows that, while the spatial resolution of the hyperspectral system is lower,

the same features can be observed in the spheroids. Even if HSI images have a lower resolution than confocal imaging, we can still observe that the fluorescent cells originating from two different cell lines do not mix homogeneously while forming the spheroid. Instead, they tend to aggregate in separate volumes.
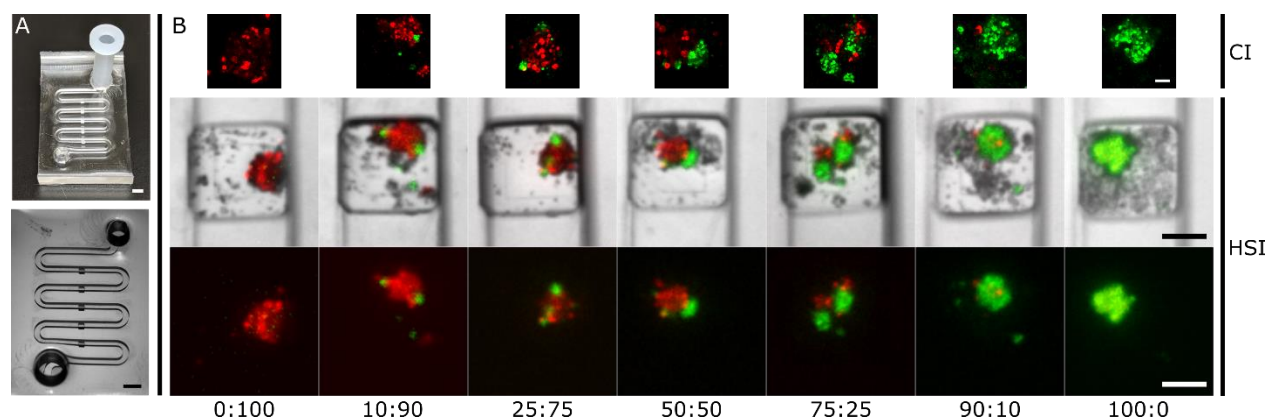
Figure 4-5: Fluorescence study of spheroids loaded on-chip. (A) Microfluidic chip A. Top photograph shows chip A with an inlet inserted. Bottom photograph shows the tilted chip. Scale bars = 2 mm. (B) Visual comparison of confocal imaging (CI) and HSI of co-culture spheroids made with different ratios of eGFP-OV1946 and mCardinal-OV90. Top row shows maximum projections of confocal imaging of the same spheroids. Scale bar = 100 µm. Middle row shows brightfield (at 720 nm) overlaid with eGFP (at 515 nm) and mCardinal (at 685 nm) fluorescence. Bottom row shows only the fluorescence intensities of eGFP and mCardinal. Scale bars = 300 µm.

In a second experiment, we used fluorescent clones produced from the same cell line to form homogeneously mixed co-culture spheroids. Since the cell line OV1946 is known for its genetic instability [35], the stable clone selection process done after transfection with fluorescent proteins should produce subclones of varying growth behaviors. To assess if hyperspectral imaging could measure these even in co-culture spheroids where the cells are mixed homogeneously, spheroids were made in chip B using mCherry- and eGFP-expressing OV1946 cells at the following initial ratios: 100:0, 75:25, 25:75, and 0:100. 24 spheroids were imaged in a single acquisition and their subpopulations' fluorescence was measured every day for 9 days. The experiment was repeated 3 times. Figure 4-6A shows the microfluidic chip used in this experiment. The bottom row images in Figure 4-6A show that, contrary to spheroids shown in Figure 4-5B, cells in co-culture spheroids formed using fluorescent subclones of the same cell line are homogeneously mixed. Figure 4-6B

shows the brightfield image of 24 spheroids made in chip B using the initial ratio 25:75 (eGFP:mCherry). Blue squares are added to represent the maximum number of spheroids that it would be possible to image in a single acquisition using the hyperspectral system. For this particular well size, 60 spheroids could be imaged in the 7.25 mm-diameter field of view. Figure 4-6C shows the corrected fluorescence at 515 nm (eGFP's emission peak) and 610 nm (mCherry's emission peak) while Figure 4-6D shows the transmittance image at 515 nm of the same 24 spheroids. The spheroids' transmittance varies between 20% and 30%, depending on their size. Here, α was fixed at 0 during the image analysis steps to show the spheroid corrected fluorescence. Acquisition times for confocal and hyperspectral imaging are similar ($\approx$ 5 minutes per acquisition). But since the wide-field capabilities of the HSI system allows up to 60 spheroids in the same field of view, acquisition times are up to 60 times faster using our system.
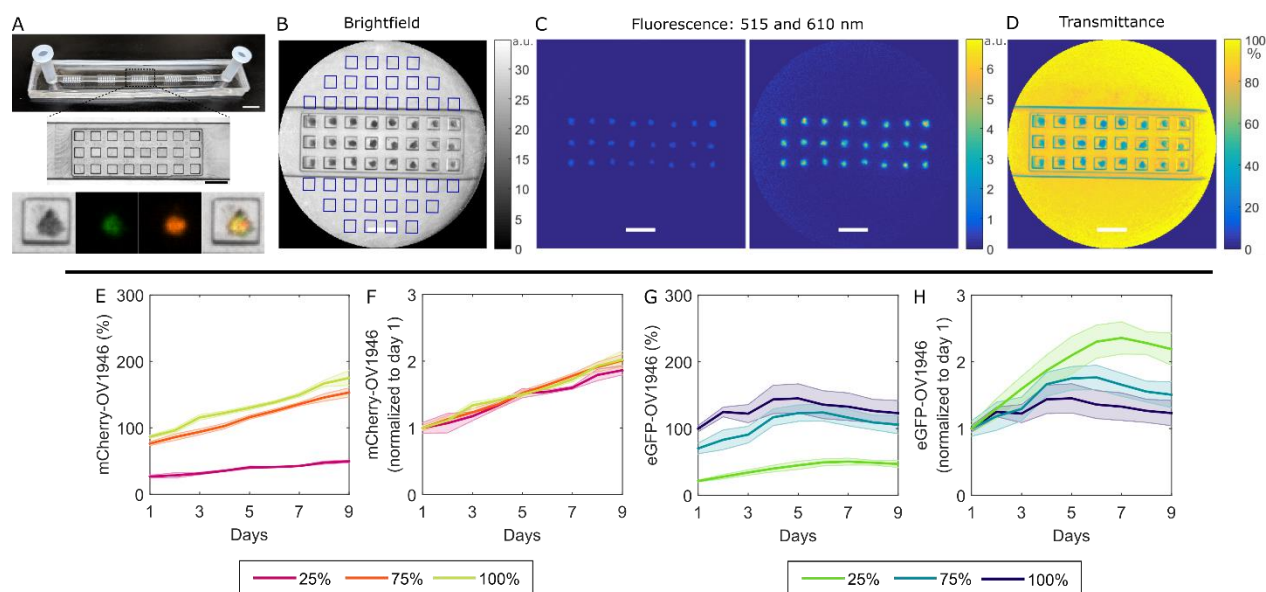
Figure 4-6: Fluorescence-based growth assay of spheroids formed on-chip. (A) Microfluidic chip B. Top photograph shows chip B with inlets and outlets inserted. Scale bar = 6 mm. Middle photograph shows a series of 24 wells. Scale bars = 1 mm. Bottom photographs show brightfield and fluorescence at 515 and 610 nm images and their overlay. (B-D) Brightfield (at 720 nm), fluorescence (at 515 and 610 nm) and transmittance (at 515 nm) imaging of 24 co-culture spheroids expressing eGFP and mCherry (ratio 25:75). Scale bars = 1 mm, a.u. is for arbitrary units. In (A), blue square shows an extrapolation of how many spheroids of the same size could be imaged if the microfluidic chip was optimized. (E-H) Growth assay quantifying each fluorescence subpopulation forming co-culture spheroids. Co-culture

spheroids were formed by mixing two cell lines at specific ratios (100:0, 75:25, 25:75, and 0:100). Evolution over time of the initial percentage of mCherry-OV1946 (E) and eGFP-OV1946 (G) cells for each initial ratio. Day 1-normalized fluorescence intensity of mCherry-OV1946 (F) and eGFP-OV1946 (H). Shaded areas for each curve represent the standard error of the mean ($n = 3$).

Figure 4-6E shows the percentage of mCherry-OV1946 cells over time for each initial ratio. Figure 4-6F shows the same curves normalized to day 1, since spheroids are formed in 24 h. This figure clearly shows that, from day 1 to 9, their growth rate is linear and nearly identical for each initial ratio. Contrary to mCherry-OV1946 cells, eGFP-OV1946 cells presented a different growth behaviour (Figure 4-6G). While each experiment repetition yielded very similar growth curves for mCherry cells, as highlighted by the small error bars, eGFP cells proliferated more erratically in each repetition. Their growth also reached a plateau around day 4, contrary to mCherry cells. Figure 4-6H shows that eGFP cells that formed initially 25% of a spheroid grew more than eGFP cells that formed 100%, even if the total amount of cells in the spheroids was the same. In 200 to 300-µm spheroids, eGFP cell growth is reduced in the presence of other eGFP cells.

By showing how cell subpopulations behave differently in co-culture spheroids, Figure 4-6E-H illustrates how quantifying co-culture spheroid fluorescence using HSI is an ideal method to measure cell populations independently and non-destructively while the spheroids are still trapped in a microfluidic chip. Also, the hyperspectral system was found to be more versatile in terms of choosing which and how many fluorophores to image since the shape of the whole fluorescence spectrum is known for each pixel of the image, while confocal imaging is limited to the filter cubes or spectral capability of the confocal microscope.

Since the samples are transilluminated, a larger volume of the spheroids can be analyzed, providing an advantage over confocal microscopy (usually used in epi-illumination). In confocal microscopy, the pinholes used to create the optical sectioning limit the detected intensity and light penetration in 3D cultures [44], [121], [122]. Also, the volume sampled in a 3D specimen by an imaging system depends on the illumination and detection configuration. Epi-illumination imaging systems mostly sample one side of the spheroids, since illumination and detection are performed on the same side. This technique will be more sensitive to the effect of a treatment on the outer layer of a spheroid.

51

Transillumination, on the other hand, will sample more of the spheroid volume since illumination is on the other side of the sample compared to detection.

4.5 Experimental

4.5.1 Hyperspectral imaging system

The custom-built spectroscopic imaging system presented here is detailed in Figure 4-1B. It uses a white light lamp for transmittance measurements and a filtered supercontinuum laser that allows the user to vary the fluorescence excitation wavelength between 400 nm and 720 nm. A liquid crystal tunable filter is used to perform a wavelength-sweep and acquire spectroscopic data. More precisely, a tungsten-halogen white light source (HL-2000, Ocean Optics, USA) is used to illuminate the sample from below, using a Köhler illumination setup, where two irises independently control the area illuminated and the illumination irradiance. In a second illumination branch, a supercontinuum laser (Fianium, NKT Photonics, Denmark) coupled to a laser line tunable filter (LLTF, Photon etc, Canada) and a mode scrambler is used to excite the fluorescence of the sample. The two illumination branches are combined using a 50:50 cube beamsplitter (BS013, Thorlabs, USA). A fixed focal length objective (59-871, Edmund Optics, USA) and a Steinheil triplet lens (67-422, Edmund Optics) acting as a relay lens are used to image the sample on an electron-multiplying charged coupled device (EMCCD) camera (HNü 512, Nüvü Caméras, Canada) thermoelectrically cooled to -85°C. A liquid crystal tunable filter (LCTF) with a bandwidth of 7 nm (VariSpec VIS, Perkin-Elmer, USA) is placed between the relay lens and the EMCCD to acquire spectroscopic data at each pixel of the image. A 500 nm (or 550 nm) shortpass filter (FESH0500 or FESH0550, Thorlabs) filters out the excitation laser light to remove any unwanted harmonics due to the LLTF. A 500 nm (or 550 nm) longpass filter (FELH0500 or FELH0550, Thorlabs) is placed after the objective to remove the excitation laser from the acquired images.

4.5.2 Data acquisition

Two excitation wavelengths are used in this work: 480 nm and 530 nm. To acquire a spectroscopic image of the microfluidic chip placed in the sample plane, the LLTF is set to 480 nm (or 530 nm) and a custom LabVIEW 2014 (National Instruments, USA) software [168] is used to sweep the

LCTF from 500 to 720 nm (or 560 to 720 nm) and acquire an image every 5 nm. The resulting image cube is a 3D matrix of 512 by 512 pixels by 45 (or 33) wavelengths.

To apply the image analysis steps, the acquisition of several data cubes is required for each sample. First, three acquisitions are made using the imaging system in fluorescence mode, all at the same acquisition time and gain: 1) a fluorescence image (while the sample is present in the sample plane); 2) a dark noise image (camera shutter closed); 3) a bleed-through image of the laser (no sample present). A similar set of data cubes is acquired using the white light source to measure the transmittance of the sample. A typical acquisition of brightfield and fluorescence (480 nm excitation) data cubes takes 149.85 s (2.5 min). Table 4-1 summarizes the different data cubes needed for the subsequent image analysis and shows the typical acquisition parameters used to measure the fluorescence of spheroids trapped in a microfluidic chip.

Table 4-1: Data cube definition and typical acquisition parameters. Top: Different data cubes acquired for a given sample. Bottom: Summary of the typical acquisition parameters.

Condition	Fluorescence acquisition	Brightfield acquisition
Sample present	Fluorescence of sample	Brightfield of sample
Camera; shutter closed	Dark noise (fluorescence)	Dark noise (brightfield)
No sample present	Laser bleed-through	System transmission

		Fluorescence acquisitions	
Parameters	Brightfield acquisitions	480 nm excitation	530 nm excitation
Cut-off wavelengths for filters	500 nm	500 nm	550 nm
Acquisition time (per wavelength)	10 ms	200–1000 ms	500–1000 ms
Gain (per wavelength)	50	500	250–500
Time to acquire one image cube	2.7 s	11.25 to 47.25 s	29.50 to 62.25 s
Laser power density	—	$213\ \mu W\ cm^{-2}$	$316\ \mu W\ cm^{-2}$
Spectral resolution		7 nm	
Acquisition range		500–720 nm	
Wavelength-step		5 nm	

After any changes to the imaging system (such as optical alignment or optical parts for example), a series of calibration steps are performed to characterize the imaging system. First, the transmittance of a USAF 1951 resolution target (R3L3S1N, Thorlabs) is measured between 500 and 720 nm using the white light source. This acquisition is used to measure the field of view and the spatial resolution of the system. A set of uniformly fluorescent Chroma slides (92001, Chroma, USA) is then measured in fluorescence and brightfield modes to characterize the spatial intensity variations due to the imaging system's optical design. A shading correction is applied for each sample and its performance is assessed using uniformly fluorescent beads (UVPMS-BR-1.090 300-

355um, Cospheric LLC, USA). Finally, the excitation laser power density for both excitation wavelengths is measured at the sample plane using a power meter (S121C, Thorlabs).

4.5.3 Image analysis

To analyze hyperspectral images and quantify a sample's fluorescence, a custom algorithm was developed. Fluorescence spectra acquired for each sample are processed in MATLAB R2015a (The MathWorks, Inc., USA) to extract quantified data according to the steps listed in Figure 4-2. Each data cube is first normalized to the acquisition time and the gain of the EMCCD camera, as those parameters are calibrated linearly by the camera's manufacturer. Dark noise, measured for each acquisition time and gain parameter set (see Table 4-1), is then subtracted from the fluorescence and brightfield images of the studied sample.

A shading correction is applied to the sample images to correct for uneven illumination and detection due to the system's optical design. Using fluorescence and brightfield images of the uniformly fluorescent orange Chroma slide acquired during the calibration steps, a compensation matrix is calculated by first smoothing the images and then normalizing them to their maximal values. For fluorescence measurements, a single fluorescence compensation matrix is calculated using the image at the emission peak maximum (555 nm), while a brightfield compensation matrix is calculated at each wavelength of the brightfield measurements. The shading correction is applied to the fluorescent images by dividing the images at each wavelength by the fluorescence compensation matrix and to the brightfield images by dividing the images at each wavelength by their corresponding brightfield compensation matrix.

The transmittance of the sample is then calculated by dividing its brightfield data cube by the brightfield images acquired while no sample is present ("System transmission" data cube from Table 4-1). The region of interest (ROI) to further study the fluorescence of the sample is then defined.

If precise fluorescence quantification is needed, a quantification step can be performed to correct for the optical properties of the sample that are impacting the fluorescence measured by the camera.

To do so, the fluorescence data cube is divided by the transmittance image according to a modified normalization quantification algorithm based on [155]:

$$\Phi^{Ratio}(\lambda) = \frac{\Phi^{Fluo}(\lambda)}{(\Phi_m^{Trans})^\alpha} \qquad (4\text{-}1)$$

where $\Phi^{Ratio}(\lambda)$ is the quantified fluorescence spectrum, $\Phi^{Fluo}(\lambda)$ is the fluorescence spectrum after shading correction, Φ_m^{Trans} is the transmittance intensity at the fluorophore emission peak, and α is empirically determined using liquid optical phantoms of known optical properties.

In each ROI, a spectral unmixing is performed to 1) remove the excitation laser bleed-through and 2) extract the contribution of each fluorophore present in the sample. The spectral unmixing is done by solving a nonnegative linear least-square problem. The basis spectra are previously acquired experimental fluorescence spectra of each fluorophore, and an average spectrum extracted from the same region of interest but using the bleed-through data cube ("laser bleed-through" from Table 4-1). Since the intensity of the bleed-through is acquired while no sample is present and the PDMS affects the intensity of the bleed-through contamination when the fluorescence of the sample is acquired, the bleed-through is removed through spectral unmixing instead of simply subtracted from the fluorescence data cube.

4.5.4 Optical phantoms

Optical phantoms mimicking spheroid optical properties were made of fluorescein (M422-05, Avantor, USA) to simulate eGFP and Intralipid® 20% (2B6023, Baxter, Canada) as a light scatterer. Fluorescein was solubilized in a 0.1 M TRIS-HCl (Tris(hydroxymethyl)aminomethane hydrochloride) buffer (TRIS base: 600-125-IK, Wisent Inc., Canada, and HCl: 3750.1-32, Ricca Chemical Company, USA) made at pH 8. Fluorescein concentrations of 0.625, 1.25, 2.5, 5, and 10 µg/ml and reduced scattering coefficients at 515 nm of 0.5, 1, 1.5, 3, 5, and 7.5 cm^{-1} were combined to make 30 different phantoms. These liquid phantoms were introduced in a 1 mm-pathlength cuvette made of optical glass (G101, Azzota, USA).

4.5.5 Microfluidic chips

Two microfluidic chips were used to form spheroids on-chip and/or hold them in place to image them. Chip A, shown in Figure 4-5A, is based on Astolfi *et al.* [44] and is composed of a main

channel and five wells. A maximum of five spheroids previously made using other techniques can be loaded in the chip and trapped in the wells. The second microfluidic chip used, Chip B, shown in Figure 4-6D, is based on a design by Patra *et al.* [104] and is used to form 120 spheroids directly on-chip using a cell suspension. Spheroids made using this microfluidic chip can then be easily exposed to treatments without accidentally releasing them from the wells. The microfluidics chips used in each experiment were chosen according to how the spheroids were formed, whether on-chip or using the hanging droplet method [11].

Chip A consists of 5 wells placed under a main channel. Each well is 600 x 600 μm^2 and 500 μm in height. The top channel is 600 μm wide by 600 μm in height. Poly(methyl methacrylate) (PMMA) molds were micromachined by a computerized numerical control (CNC) machine (EMCO PC Mill 55, EMCO GmbH, Austria); one for the main channel and the wells and the other for the layer containing the inlets and outlets. Degassed liquid PDMS (Sylgard® 184 silicone elastomer kit, Dow Corning, USA) mixed at 10:1 ratio was then poured into the two molds and cured in an oven at 80 °C for 1 h. The two layers were then exposed to an atmospheric plasma for 30 s and then bonded together. Hollow nylon cylinders (91145A138, McMaster-Carr, USA) were then inserted in the main channel inlets. In this design, spheroids made using the hanging droplet method were introduced in the chip inlet. Careful aspiration of the fluid at the outlet was then used to position the spheroids over the wells and let them sediment.

Chip B was also made using CNC micromachined molds and PDMS. It consists of a main channel containing 5 series of 24 wells. Each well is 500 x 500 μm^2 and 500 μm in height. The top channel is 2 mm wide and 500 μm in height. The circular inset of Figure 4-1B shows a brightfield image of a section of the chip where 24 wells contain spheroids formed on-chip.

Both microfluidic chip designs were prepared for cell culture by first introducing 100% ethanol to remove any bubbles in the chips. 70% ethanol was then introduced for 10 minutes to sterilize the chips. A solution of sterilized triblock copolymer (10 mg/mL, Pluronic® F-108, 542342, Sigma-Aldrich, USA) was then incubated in the chip at 37 °C for at least 1 h or overnight to prevent cell adhesion on the channel walls and inside the wells. Chips were then re-sterilized using 70% ethanol for 10 minutes and chips were finally completely rinsed and filled with sterile Hank's Balanced Salt Solution (HBSS, 311-516-CL, Wisent Inc.) supplemented with 600 $\mu g/L$ amphotericin B (450-105-QL, Wisent Inc.) and 55 mg/L gentamicin (450-135-XL, Wisent Inc.) and then stored for

future use at room temperature in a sterile humidity chamber (plastic box containing a tissue moistened with sterile water) to prevent HBSS evaporation.

4.5.6 Spheroid culture

Two high grade serous epithelial ovarian cancer cell lines, OV1946 [35] and OV90 [36], were previously established from patient ascites in our laboratory at the Centre de recherche du CHUM. The two cell lines were transiently transfected with either an eGFP plasmid (pEGFP-N1, 6085-1, Clontech Laboratories Inc., USA), a mCardinal plasmid [169] (mCardinal-N1, #54590, Addgene, USA), or a mCherry plasmid (mCherry2-N1, #54517, Addgene). Plasmids mCardinal-N1 and mCherry2-N1 were gifts from Michael Davidson. To generate stable clones, successfully transfected cells were selected with 500 µg/ml G418 (Geneticin®, 10131-035, Thermo Fisher Scientific, USA) and single clones were selected by limiting dilution. Available stable clones were eGFP-expressing and mCherry-expressing OV1946 cells, and mCardinal-expressing OV90 cells.

In a first experiment, co-culture spheroids were formed using the hanging droplet method described previously [11]. Briefly, cell suspensions of eGFP-OV1946 (passage 8) and mCardinal-OV90 (passage 8) in complete OSE medium [OSE medium (316-030-CL, Wisent Inc.) supplemented with 10% FBS (080-150, Wisent Inc.), 55 mg/L gentamicin (450-135-XL, Wisent Inc.), and 600 µg/L amphotericin B] with 500 µg/mL G418 were used to obtain a total of 2.5 x 10^5 cells/ml at different ratios: 100:0, 90:10, 75:25, 50:50, 25:75, 10:90, and 0:100. Then, 16 µL of the different cell suspensions were carefully pipetted onto the inner side of the cover of a 150 mm petri dish (CA25383-103, VWR, Canada) to form droplets. The cover was gently placed on the dish containing 15 ml of phosphate buffered saline (PBS, 311-012-LL, Wisent Inc.) to prevent dehydration of the droplets. Petris were placed in an incubator at 37 °C and 5% CO_2. The spheroids were harvested at day 7 and carefully loaded into the wells of chip A for hyperspectral and confocal imaging.

Co-culture spheroids made from different ratios of two fluorescent cell lines were formed directly inside chip B. Cell suspensions of 9 x 10^5 cells/mL containing various ratios of eGFP-OV1946 cells (passage 90) and mCherry-OV1946 cells (passage 34) were prepared in complete OSE medium with G418 (500 µg/mL). Studied ratios of eGFP- versus mCherry-expressing cells were 100:0, 75:25, 25:75, and 0:100. About 600 µL of cell suspension were introduced in the main channel of each microfluidic chip to form spheroids in 24 h. The culture medium, complete OSE

medium without phenol [using OSE medium without phenol (316-031-CL, Wisent Inc.)] supplemented with 500 µg/mL G418, was replaced every 24 h by introducing 70 µL of new medium at the inlet and removing 3 x 20 µL of medium at the outlet, three times. Medium without phenol was used to avoid autofluorescence due to the phenol. Between medium changes, the microfluidic chips were kept in a sterile humidity chamber in an incubator at 37 °C and 5% CO_2. 24 h after cell seeding, the cells aggregated and formed one spheroid per well without adhering to the PDMS surface. When necessary, spheroids trapped in the microfluidic chip were stained with fluorescent markers. A 5 µM solution of CellTracker™ Orange CMTMR (C2927, Thermo Fisher Scientific) in HBSS was added to the chip and placed in an incubator at 37 °C and 5% CO_2 for 1 hour. The staining solution was then rinsed with fresh medium.

4.5.7 Confocal imaging

Confocal imaging was performed on co-culture spheroids trapped in Chip A. Images were acquired on a Leica TCS-SP5 inverted microscope (Leica Microsystems, Germany) using a HC PL FLUOTAR 20x/0.50 dry objective. Excitation system was performed using the 488 nm line of an argon laser for eGFP, and the 561 nm diode-pumped solid state (DPSS) laser for mCardinal using a sequential acquisition at a scan speed of 400 Hz. Spectral detector mirrors were set for each fluorophore to avoid excitation and emission crosstalk: 500 nm-550 nm for eGFP; 598 nm-700 nm for mCardinal. Z-stack images were acquired with an 8 µm step size and maximum projections were performed using the Las-AF software. Final images are 8 bits and 512 x 512 pixels with a zoom factor of 1.5.

4.6 Conclusions

We presented a custom designed wide-field HSI system based on a liquid crystal tunable filter to image tumor spheroids while they are trapped in a microfluidic chip. It circumvents the typical limitations of confocal microscopy: acquisition time and light penetration depth. Its wide-field capability allows the simultaneous measurement of up to 60 spheroids in a single acquisition. Furthermore, the spectral resolution of the HSI system enables a wide choice of fluorophores to image. The acquisition of the whole fluorescence spectrum for every pixel of the image increases the discriminating power for spectral unmixing and allows the study of fluorophores with more similar spectra than conventional filter-based methods. Also, because of the supercontinuum laser

and its laser line filter, the excitation wavelength can be adjusted for photoactivable fluorophores [170]. The HSI system permits non-destructive measurements of 3D cell cultures, unlike flow cytometry. This becomes an important advantage when studying the evolution of a spheroid response to a molecular agent at multiple time-points. Although the spheroid work presented here relates to ovarian cancer, any cancer whose cells spontaneously form spheroids in low attachment environment can be studied as well as small tissues such as organoids [41], embryos [171], and microdissected tissues [44].

4.7 Conflicts of interest

There are no conflicts of interest to declare.

4.8 Acknowledgements

CHAPTER 5   ARTICLE 2: LONG TERM FLUORESCENCE HYPERSPECTRAL IMAGING OF ON-CHIP TREATED CO-CULTURE TUMOUR SPHEROIDS TO FOLLOW CLONAL EVOLUTION

Amélie St-Georges-Robillard,[1,2] Maxime Cahuzac,[2] Benjamin Péant,[2,3] Hubert Fleury,[2] Muhammad Abdul Lateef,[2] Alexis Ricard,[2] Alexandre Sauriol,[2] Frédéric Leblond,[1,2] Anne-Marie Mes-Masson,[2,4] Thomas Gervais[1,2]

[1] Polytechnique Montréal, Department of Engineering Physics and Institute of Biomedical Engineering, Montreal, H3C 3A7, Canada.

[2] Centre de recherche du Centre hospitalier de l'Université de Montréal and Institut du cancer de Montréal, Montreal, H2X 0A9, Canada.

[3] TransMedTech Institute, Montréal, H3T 1J4, Canada.

[4] Université de Montréal, Department of Medicine, Montreal, H3T 1J4, Canada.

5.1 Background information

Article 2 [172] was submitted to *Integrative Biology* on December 17th, 2018 and is presented in this chapter. It discusses an application of the hyperspectral imaging system on how to follow cell populations in co-culture spheroids over time and non-destructively. This article details an experiment design and the analysis necessary to calculate the co-culture spheroid composition quantitatively and measure their response to external stimuli. First, two fluorescent subclones of the same parental ovarian cancer cell line were created. HSI spheroid composition measurements were compared with values obtained by flow cytometry, the gold standard to measure cell populations in 3D culture. A 2D proliferation assay of the two fluorescent subclones independently and mixed together was performed. The trend observed in 2D, where the green subclone grew faster than the red, was also observed in 3D spheroids using hyperspectral imaging. A treatment assay to PARP inhibitor talazoparib was then performed to illustrate how HSI can follow each cell population's response to the treatment in the same spheroids over time. A proof-of-concept that HSI can also follow cell population's response to chemotherapy drug carboplatin was also performed.

My contribution for this article is 70% of the work. I designed, performed, and analyzed all the experiments, except the 2D proliferation assay (5.6.6), and the 2D clonogenic assay (5.6.7) results. I wrote the article, except the Materials and methods sections: 5.6.5, 5.6.6, and 5.6.7. M.C. generated the mCherry-OV1946 clone, performed the 2D IC$_{50}$ experiment and part of the 2D proliferation experiment and interpretation. B.P. helped design the experiments. H.F. and A.R. did part of the 2D proliferation experiment and interpretation. M.A.L. performed the flow cytometry. A.S. generated a variant of the OV1956 cell line. A.-M.M.-M., F.L., and T.G. provided support and supervised the research.

5.2 Abstract

Multicellular tumour spheroids are an ideal *in vitro* tumour model to study clonal heterogeneity and drug resistance in cancer research because different cell types can be mixed at will. However, measuring the individual response of each cell population over time is challenging: current methods are either destructive, such as flow cytometry, or cannot image throughout a spheroid, such as confocal microscopy. Our group previously developed a wide-field fluorescence hyperspectral imaging system to study spheroids formed and cultured in microfluidic chips. In the present study, two subclones of a single parental ovarian cancer cell line transfected to express different fluorophores were produced and co-culture spheroids were formed on-chip using ratios forming highly asymmetric subpopulations. We performed a 3D proliferation assay on each cell population forming the spheroids that matched the 2D growth behaviour. Response assays to PARP inhibitors and platinum-based drugs were also performed to follow the clonal evolution of mixed populations. Our experiments show that hyperspectral imaging can detect spheroid response before observing a decrease in spheroid diameter. Hyperspectral imaging and microfluidic-based spheroid assays provide a versatile solution to study clonal heterogeneity, able to measure response in subpopulations presenting as little as 10% of the initial spheroid.

5.3 Introduction

Many types of cancer, including ovarian cancer, are characterised by the presence of clonal heterogeneity, where tumours are composed of multiple populations of malignant subclones with different genetic mutations. These subclones can then each evolve differently over time and in response to treatments. Treatment affecting one subclone can lead to tumour repopulation by a

different and possibly more resistant subclone. Cancers with high levels of clonal heterogeneity are thus associated with poor prognosis, treatment resistance, and an increased difficulty to develop biomarkers of prognosis or treatment response [10], [49], [50]. To study clonal heterogeneity, monolayer co-culture of cancer cells can be used as an *in vitro* cancer model. However, there is now evidence that 3D cellular models, such as spheroids, are more relevant than 2D cell culture as *in vitro* cancer models for drug discovery [42]. Spheroids are 3D cell aggregates that better reproduce cell-cell and cell-matrix interactions [4], [39], [40]. They also incorporate fundamental mass transfer limitations important in most cellular response to drugs [121]. By mixing two or more cell lines in a single spheroid, researchers can improve their relevance and include clonal heterogeneity in their studies. Informative assays include mixing epithelial and stromal cells, resistant and sensitive cells, or cancer and immune cells.

The microfluidics community has provided numerous tools that can easily perform assays on 3D tissue models such as spheroids, organoids [41], and micro-dissected tissues [44]. Researchers have developed chips that can form up to thousands of spheroids in one step and expose them to external stimuli [13], [59], [65], [70], [78], [104], [173]. Chips are especially useful to hold or trap spheroids in place during medium changes or when adding drugs of interest without the risk of pipetting them out of plate wells [73], [74], [76]. However, there remains important challenges including methods that analyse sample dynamics, including tracking cell populations in co-culture spheroids.

To study these co-culture spheroids in terms of proliferation, response to treatment, or invasion, each cell population composing the spheroids must be studied independently rather than measuring whole spheroid response [85] as cell populations can compete or co-operate for survival against a drug within a spheroid [51]. These constraints greatly restrict the number of methods that can be employed to analyse this response. For example, diameter or volume measurements, often reported in the literature as a metric of spheroid response [14], [54], [103], can no longer be applied to determine cell population-specific responses.

Over the years, several methods have been developed to distinguish subclonal population growth within a multicellular system whether spheroids were formed in microfluidic chips or using conventional methods. Techniques are either based on cell morphology [174], colorimetric or fluorescent antigen stains [14], genetic modifications to inherently express different fluorescent

markers, or viability dyes [14]. When these markers are used in 2D monolayer culture, conventional microscopes can distinguish individual cells. Cells can then be counted visually according to whether they present the markers or not. However, the same technique cannot be applied to 3D tissue analysis unless spheroids are first digested into a single cell suspension.

In response, a lot of effort has been applied to adapting fluorescence-based methods to correctly quantify cell populations in 3D cultures using either fluorescent proteins [107], fluorescent trackers or viability dyes [105], [108]. A conventional optical fluorescence microscope can quantify spheroid fluorescence intensity if parameters during the image acquisition are known and controlled [14], [112]. However, most optical microscopes are designed to image cell monolayers using a depth of field corresponding to the size of a cell. If used to image 3D cultures, a slightly out of focus sample can drastically affect the measured fluorescence intensity [114], [115]. This hinders precisely quantifying spheroid fluorescence using conventional optical microscopes and limits their usefulness. Confocal microscopy was developed to image virtual optical sections of 3D samples individually using pinholes to reject light from out of focus planes of the sample. Fluorescent cells can then be counted on each slice. However, this optical sectioning is done at the cost of lower signal intensity and, coupled with tissue absorption and scattering, limits light penetration in the centre of a biological sample. Samples thicker than 70-100 μm are thus more difficult to image [6], [14], [120], or need to be optically cleared [175], [176]. Multiphoton microscopy can circumvent this by taking advantage of the near-infrared optical window, a range of wavelengths between 650 and 1 300 nm where light penetration depth is the highest in tissues. However, to achieve multiphoton excitation of fluorophores, objectives with high numerical apertures and shorter working distances are needed, rendering imaging thick (> 5 mm) microfluidic chips difficult [15]. For all three types of microscopy, the typical filter cubes used reduce their spectral resolution and increases cross-talk between fluorescence channels, limiting which and how many fluorophores can be imaged, especially when large spectral overlaps exist [112]. Flow cytometry or fluorescence activated cell sorting (FACS) can resolve a large number of fluorescent markers but require spheroid digestion into individual cells before analysis [177]. Studying the same sample over time is impossible using this type of destructive technique. Finally, immunohistochemistry and immunofluorescence performed on tissue slices (paraffin embedded or cryosections) are also used but present the same drawback as FACS as they are destructive techniques [14].

In this paper, we describe a method using hyperspectral imaging (HSI) to quantify cell populations over time in co-culture spheroids in response to external stimuli. The HSI system was optimised to analyse multiple spheroids on-chip in a single acquisition. Co-culture spheroids expressing two fluorescent proteins were formed directly on-chip and their growth was followed over time as a function of the initial cell seeding ratio. Based on the different proliferation rates for each fluorescent subclone, we hypothesised that hyperspectral imaging could also be used to study the dynamic effect of chemotherapy drugs affecting DNA such as PARP inhibitors [23] and platinum-based drugs [22] in cell populations with distinct growth properties. We then studied spheroid response to different chemotherapy drug concentrations and measured each fluorescent population's dynamic response to the drug over time. Our method has the advantage of being non-destructive: the dynamic response of each cell population in the spheroids can be followed at multiple time-points over time and large numbers of spheroids can easily be measured. Three sets of experiments are described in this work illustrating the potential of hyperspectral imaging for spheroid-based research.

5.4 Results

5.4.1 Hyperspectral imaging workflow to quantify cell populations in co-culture spheroids

Figure 5-1 introduces the workflow presented in this article. We first produced fluorescent subclones of the ovarian cancer cell line OV1946 [35]. This cell line, established from patient ascites, can form spheroids in a low attachment environment. In a previous study [159] we observed that subclones made from two different parental cell lines did not mix homogeneously in spheroids and remained as distinct aggregates. As cell-cell interactions are an important factor in studying cancer and drug resistance [5], we chose to use a single ovarian cancer cell line to make two fluorescent subclones with the hypothesis that the two cell populations would mix homogeneously. The two fluorescent populations were produced by transfecting OV1946 cells with enhanced Green Fluorescent Protein (eGFP) (eGFP-OV1946) and mCherry (mCherry-OV1946) plasmids. Two subclones from the transfected populations were selected by limited dilution to obtain cells expressing each fluorescent protein at similar intensity for a specific subclone, as illustrated in step 1 of Figure 5-1.
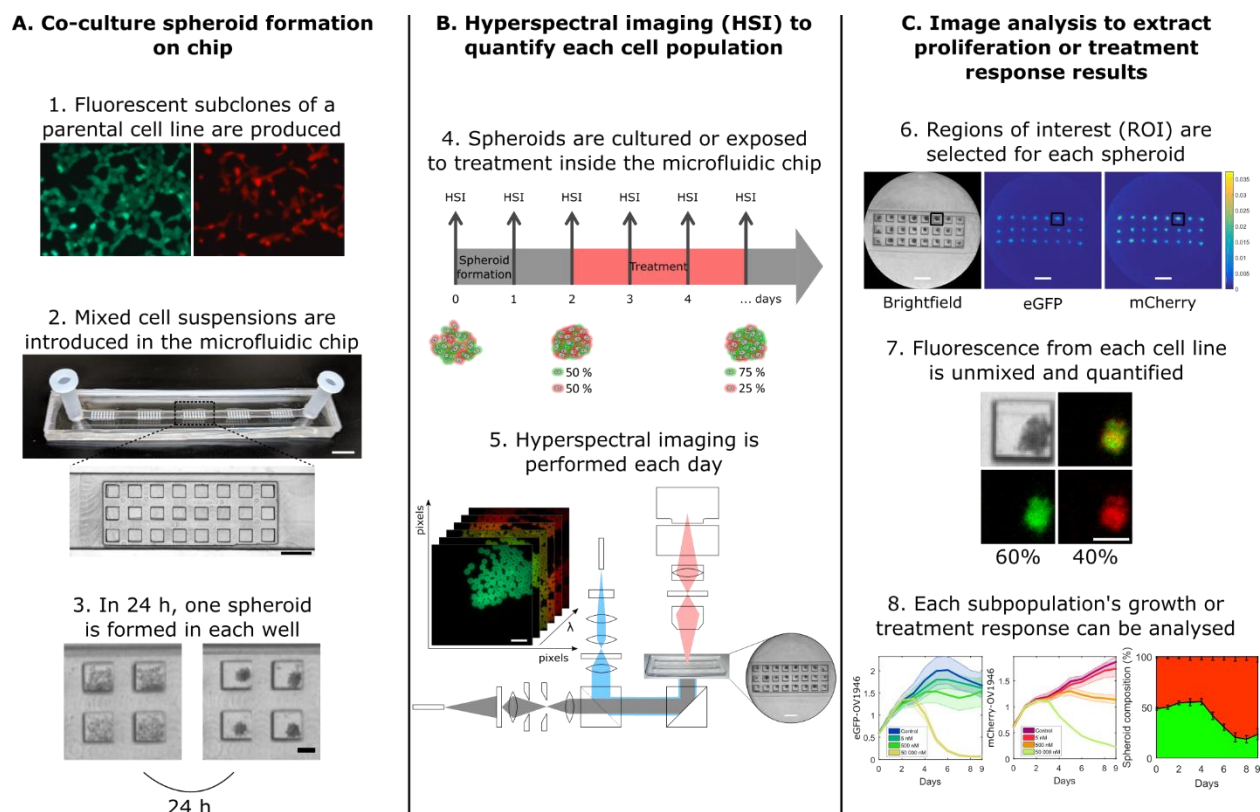
Figure 5-1: Co-culture spheroid assay using hyperspectral imaging workflow. A) Fluorescent subclones of the same parental cell line were first generated by transfecting OV1946 cells. For one subclone, all cells express the fluorescent protein (eGFP or mCherry) at similar levels due to a limited dilution selection. Co-culture spheroids are then formed on-chip by introducing a cell suspension containing both subclones in the main channel of the microfluidic chip. Cells sediment into the wells and form spheroids in 24 h. Scale bars in 2 represent 6 and 1 mm and scale bar in 3 represents 250 μm. B) Spheroids are cultured in the microfluidic chip and medium, in which drugs can be added, is changed daily. A custom-built HSI system[159] was then used to image and quantify the spheroids' fluorescence at multiple time-points. C) HSI images were processed to remove any system response. Regions of interest (ROI) corresponding to each well of the microfluidic chip were determined and spectral unmixing was performed to separate the spectral entities. Fluorescence intensities from each fluorescent protein were normalised to the reference intensity and the spheroid composition, a percentage of each subclone, was calculated. Using the fluorescent protein intensity and the spheroid compositions over time, the co-culture

spheroid response to external stimuli could be analysed. Scale bar in 7 represents 250 μm and other scale bars not specified represent 1 mm.

The two fluorescent subclones were then mixed at different ratios to form co-culture spheroids on-chip. Various cell seeding ratios were studied: 100:0, 90:10, 75:25, 50:50, 25:75, 10:90, and 0:100 (eGFP:mCherry). The microfluidic chip used to form these spheroids is based on Patra *et al*. [104] and is composed of a main channel with groups of 24 wells placed underneath. Cells sediment in the wells and form one spheroid per well in 24 h. Their compactness depends on the cell line used. Spheroids were then cultured on-chip up to nine days after formation. Medium was changed every 24 h to replenish the nutrients available to the spheroids and remove their waste, in compliance with previously published on-chip 3D cell culture guidelines [45].

Hyperspectral imaging was used to image one group of 24 spheroids trapped on-chip in a single hyperspectral acquisition. HSI images were acquired with the system illustrated in Figure 5-1 and calibrated using the image analysis steps described in detail previously [159] to extract the true fluorescence intensity emitted by the sample from the system response. These steps are also detailed in the Materials and Methods section. As both fluorescent subclones emit the same fluorescence intensity for all their cells, and that intensity is not the same for both subclones, both proteins' intensities were normalised before calculating the proportion of each cell population in the spheroids. An average intensity of the fluorescence in regions of interest corresponding to each spheroid at day 0 was used as a reference.

5.4.2 2D proliferation assay on cell populations

While creating the eGFP and mCherry subclones by transfection, we selected clones with different proliferation rates to see if HSI is able to measure this difference while forming co-culture spheroids. Figure 5-2 shows the standard 2D proliferation assay performed to measure the proliferation rate of each subclone. Figure 5-2A-C shows the proliferation of each subclone cultured independently, where eGFP-OV1946 cells doubling time is 1.5 times faster than mCherry-OV1946. When eGFP cells were mixed at different ratio with mCherry cells, they again proliferated faster than mCherry cells (Figure 5-2D-F).
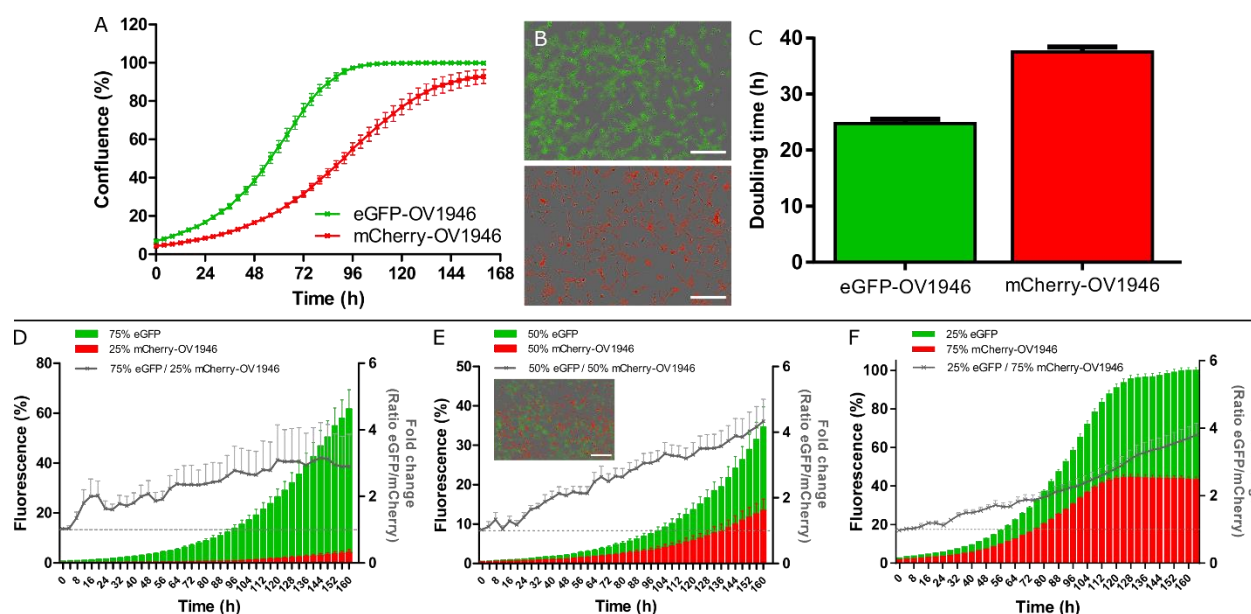
Figure 5-2: 2D cell population proliferation in monolayer culture. A) Representative example of the cell growth over time. B) Fluorescence images at 96 h, and C) average doubling time (n = 3) of each subclone cultured separately. D-F) Representative example (n = 1) of the proliferation over time of each subclone cultured together at various ratios: 75:25 (D), 50:50 (E, inset shows a fluorescence image at 96 h), and 25:75 (F). Grey curves show the fold change (normalised to 1) of the ratio between eGFP and mCherry fluorescence. Scale bars = 300 μm.

5.4.3 FACS validation

Before using hyperspectral imaging to quantify spheroid composition, we first validated that spheroid composition measurements obtained by HSI were similar to those obtained by FACS. Spheroids were made on-chip according to the same initial seeding ratios described previously. They were then cultured on-chip for 3 to 6 days, depending on the experiment (n = 3). Medium was changed daily. For this validation, 3 groups of 24 wells per chip were first imaged individually using HSI and the same spheroids were then pooled and analysed by FACS (Figure 5-3A). Figure 5-3B shows that HSI has an absolute error in spheroid composition percentage of at most 5% when compared to FACS.
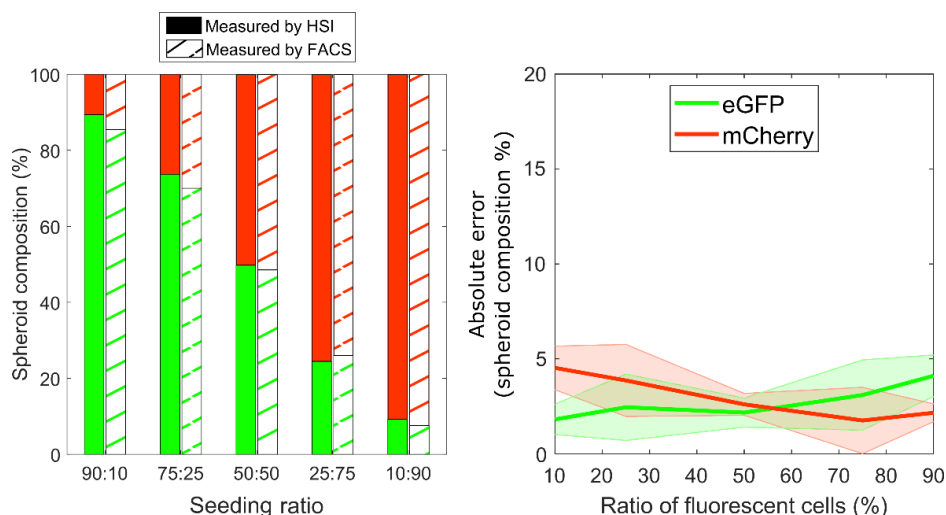
Figure 5-3: FACS validation of HSI measurements. A) Comparison of spheroid composition measurements obtained by HSI and by FACS (representative example of n = 1). B) Absolute error of HSI measurements compared to FACS. Shaded regions indicate the standard deviation of the calculated error (n = 3).

5.4.4 3D proliferation assay on cell populations

Using our HSI system and its image analysis algorithm, we validated that similar trends in the proliferation of both subclones in 2D could be observed in a 3D spheroid. The 3D proliferation assay timeline on cell populations is detailed in Figure 5-4A. Spheroids were formed on-chip at various initial seeding ratios (100:0, 90:10, 75:25, 50:50, 25:75, 10:90, and 0:100) and 24 spheroids per ratio were imaged daily until day 9. The experiment was repeated three times. Step 7 of Figure 5-1 presents representative fluorescence and brightfield images of a co-culture spheroid made with subclone of the same parental cell line, confirming our hypothesis that the two subclones would mix homogeneously. Figure 5-4B shows the brightfield images of one representative spheroid per ratio over time. We observed that compact spheroids were formed on day 2 and individual spheroid diameter then increases over time as cells proliferate. However, brightfield images alone cannot distinguish the individual growth rate of eGFP or mCherry cells. We tested the ability of fluorescence measurements by HSI to track cell population growth over time. Figure 5-4C i and iii show the spheroid composition in eGFP and mCherry cells for each initial seeding ratio. The same curves normalised to day 1 are shown in Figure 5-4C ii, iv, and v. We noted that eGFP cells first experience a rapid proliferation from day 0 up to day 5, doubling their fluorescence intensity. Their

proliferation then decreased until day 9. Shaded areas represent error bars (standard error of the mean, n = 3) and illustrate how eGFP cells' behaviour varies between the experimental repetitions. Noteworthy, even if the total number of cells in each spheroid at day 0 was the same, eGFP cells in spheroids composed mainly of mCherry cells grew more than in those made only of eGFP cells (Figure 5-4C ii). In contrast, as highlighted by the smaller error bars, mCherry cells proliferation remains constant from experiment to experiment. Their proliferation is slower than eGFP cells, but continues until day 9, where their fluorescence intensity was doubled compared to day 0. Also, we did not observe a dependence on the initial number of mCherry cells as mCherry cells in all spheroids grew at the same rate (Figure 5-4C iv). Importantly, when comparing subclones proliferation up to day 5 (Figure 5-4C v), we can see that eGFP cells grew faster than mCherry cells in earlier days, replicating the biological characteristics observed in 2D cultures.

In addition to following each cell population's fluorescence intensity over time, we also calculated the proportion occupied by each population in the spheroids. eGFP and mCherry fluorescence intensities were first normalised to a reference intensity so that both intensities could be compared, and the spheroid composition was calculated with equation (5-1) (see Materials and Methods). Figure 5-4D utilises a stacked area chart to represent the spheroid composition over time as a function of the initial seeding ratio. The proportion occupied by eGFP cells is represented by the bottom (green) area while the top (red) area represents the proportion occupied by mCherry cells. In the first 5 days, we can see a slight increase of the percentage of eGFP cells, correlating to their higher proliferation rate of the first days. At day 9, the spheroid composition then returns around the initial composition of day 0. This contrasts with results from 2D culture, where eGFP cells continued to proportionally occupy more space than mCherry cells (Figure 5-2D-F). This could be explained by effects unique to spheroids, such as competition for space within the 3D volume.
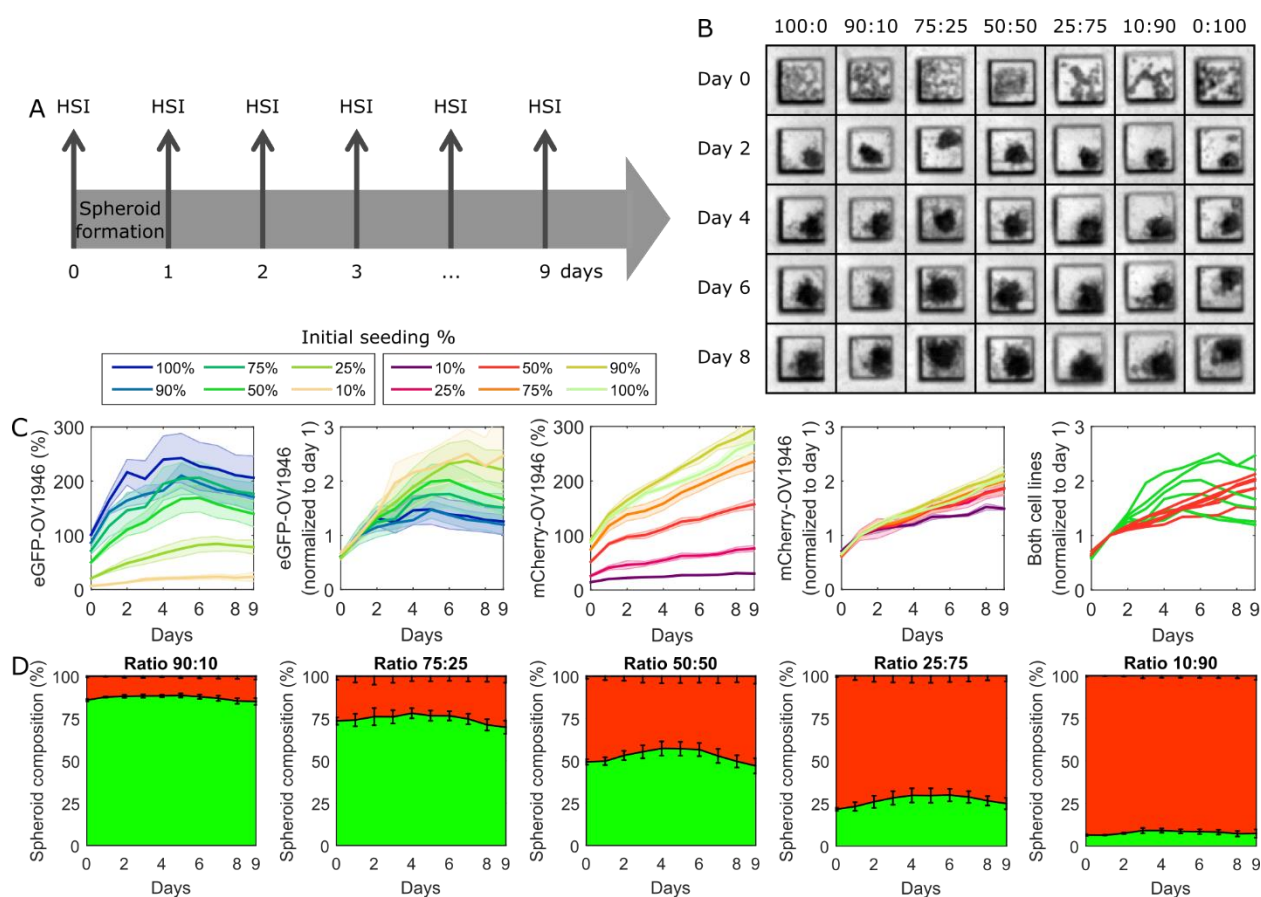
Figure 5-4: Cell population proliferation in co-culture spheroids. A) Experiment timeline. B) Brightfield images of spheroids over time. For a specific seeding ratio, the same spheroid is shown over time. C i-ii) eGFP-OV1946 and C iii-iv) mCherry-OV1946 proliferation according to the initial cell seeding ratio. In C ii and iv, curves from i and iii are normalised to day 1. C v) Comparison of the proliferation rates normalised to day 1 of both fluorescent clones (same data as in C ii and iv). D i-v) Evolution over time of spheroid composition according to initial seeding ratio (bottom/green: eGFP; top/red: mCherry). Shaded regions or error bars represent the standard error of the mean (n = 3).

5.4.5 Treatment response assay on cell populations

Clonogenic assays were performed to assess each subclone's response to the PARP inhibitor talazoparib. Figure 5-8 shows that the eGFP subclone is slightly more resistant than the mCherry subclone, although this difference is not statistically significant: eGFP cells have a 2D concentration at which 50% of colony formation is inhibited (IC_{50}) of 27.7 ± 2.0 nM and mCherry cells, of 21.2 ± 6.0 nM. Knowing that 2D and 3D culture can have different responses to

treatment [121], [178], we hypothesised that HSI could follow each cell population response independently and observe differences in response. A treatment response assay was performed by exposing the same co-culture spheroids, made at the same seeding ratio as previously, to three concentrations of drug from day 2 to day 9 (Figure 5-5A). The experiment was repeated three times. Figure 5-5B shows brightfield images of representative spheroids at day 8, depending on the treatment concentration, while Figure 5-5C shows brightfield images of spheroids over time as they are exposed to the highest talazoparib concentration (50 µM). For a specific seeding ratio, the evolution of the same spheroid over time is shown. The fluorescence intensity of each cell population measured by HSI is shown in Figure 5-5D-E. Each graph presents the response of 24 spheroids made at a specific seeding ratio to the three talazoparib concentrations and the talazoparib vehicle (medium and DSMO). In each graph, we observed a dose-response effect, where fluorescence intensity (both eGFP and mCherry) decreases after exposure to the drug starting at day 2. For both cell lines, 5 nM is too low to elicit a response, as the curves are similar to those of the control with no drug. However, for the highest concentration, we can clearly see fluorescence decreases sharply for both cell populations, indicating that cells are affected by the treatment between day 3 and 4 (after 24-48 h of treatment), which is consistent with the subclones doubling time. Using the HSI, the treatment effect was detected earlier, as spheroid diameters at day 8 (Figure 5-5B) are just starting to diminish at the highest concentration. While curves for spheroid with low starting number of cells are noisier due to a lower signal intensity (Figure 5-5D i and E vi, for example), they still demonstrate that our method can measure treatment response of cell populations occupying as little as 10% of the spheroid.
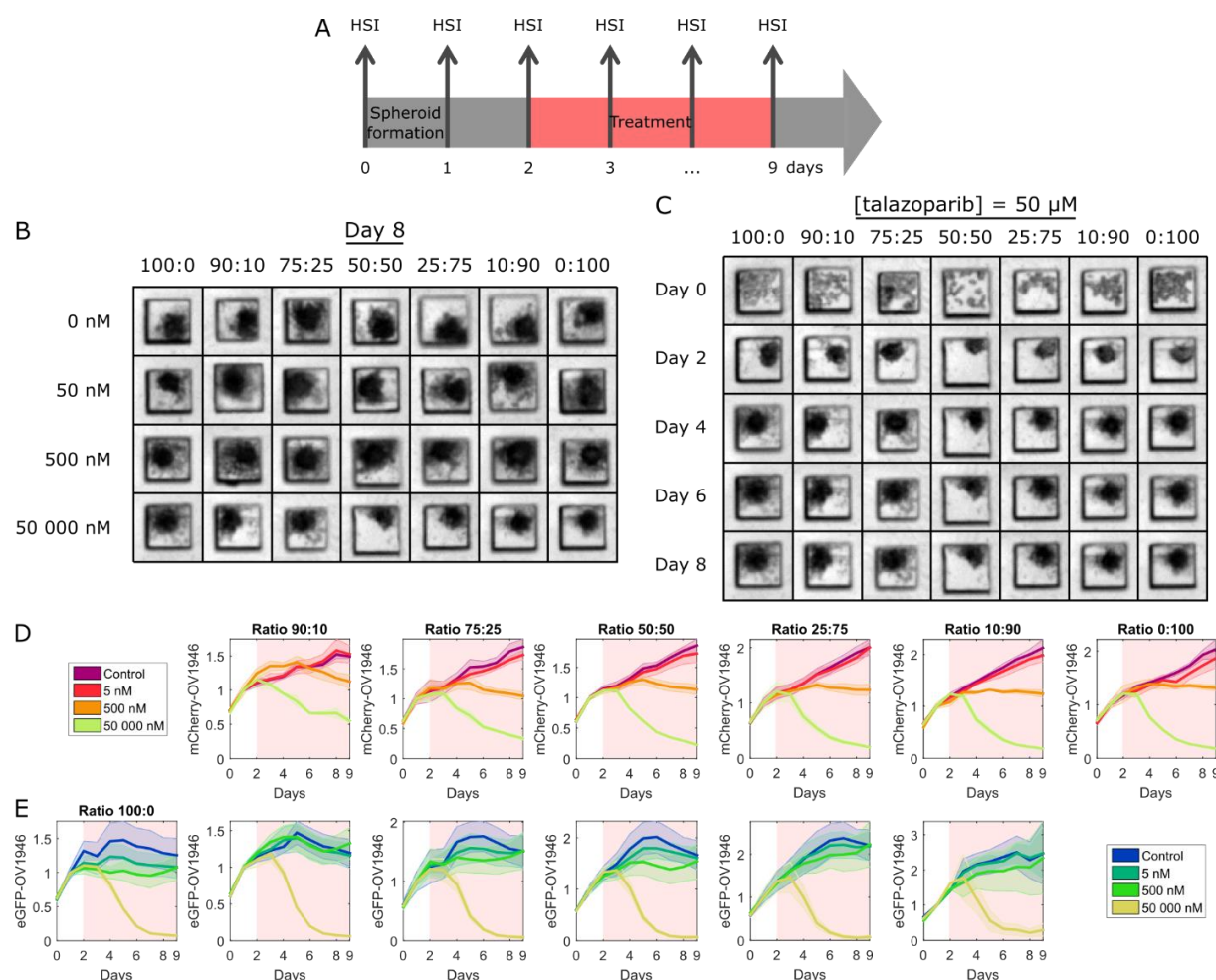
Figure 5-5: Treatment response assay using talazoparib. A) Experiment timeline. B) Brightfield images of spheroids at day 8, relevant to the drug concentration. C) Brightfield images of spheroids over time, for a talazoparib concentration of 50 μM. For a specific seeding ratio, the same spheroid is shown over time to observe its response to the drug. D i-vi) Day 1-normalised mCherry-OV1946 response to different concentrations of talazoparib, according to the initial seeding ratio. E i-vi) Day 1-normalised eGFP-OV1946 response to different concentrations of talazoparib, according to the initial seeding ratio. Shaded regions represent the standard error of the mean (n = 3).

Figure 5-6 presents the spheroid composition as a response to the three talazoparib concentrations. At 5 nM (Figure 5-6A), both cell populations react similarly to the control (Figure 5-4D). At the intermediate concentration of 500 nM (Figure 5-6B), the eGFP percentage seems to increase very slightly over time. At the highest concentration of 50 μM, we can observe that the spheroids experience a clonal takeover by mCherry cells. Both cell populations die from talazoparib, as

illustrated by Figure 5-5D-E, but mCherry-OV1946 cells seem more resistant and die less, proportionally. Independent of the initial cell seeding ratio, this takeover starts consistently at day 4, after 48h of treatment. While Figure 5-5D-E present how each subclone responds to treatment, Figure 5-6 reveals the behaviour differences between the two subclones.
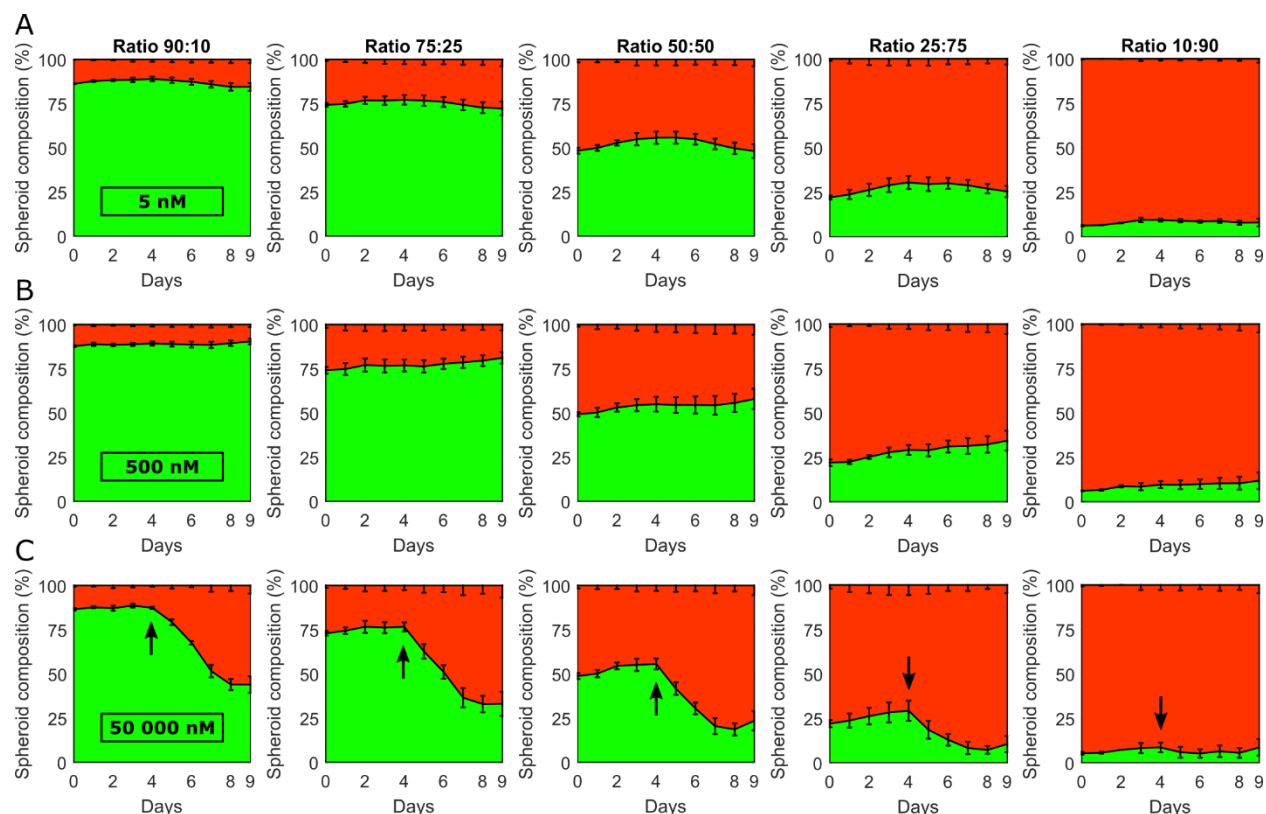
Figure 5-6: Spheroid composition as a response to talazoparib applied from day 2 to day 9. Spheroid composition over time, according to the initial seeding ratio for a talazoparib concentration of A) 5 nM, B) 500 nM, and C) 50 µM. Control data (for a talazoparib concentration of 0 nM) is shown in Figure 5-4D. For all graphs, bottom/green represent eGFP and top/red, mCherry. Arrows indicate clonal takeover onset. Error bars represent the standard error of the mean (n = 3).

As a proof of concept that HSI can also measure treatment response of spheroids exposed to platinum-based drugs, we formed co-culture spheroids using the following seeding ratios: 100:0, 50:50, and 0:100, and exposed them to carboplatin from day 1 to day 3 (Figure 5-7A). The experiment was performed once (n = 1) on 24 spheroids per condition (ratio and drug concentration). Figure 5-7B shows that, similar to the treatment response assay to talazoparib, spheroid diameters as a metric to measure treatment response is not always appropriate.

Fluorescence intensities over time (Figure 5-7C) show a dose-dependent decrease in day 1 fluorescence intensities for both subclones. At the two highest carboplatin concentrations (300 µM and 3 mM), both subclones start to die between day 1 and day 3. At the low concentration of 30 µM, the fluorescence intensities do not immediately decrease from day 1 to day 3, but instead, the decrease starts after the chemotherapy is removed: mCherry intensity starts to decrease 24 h after eGFP intensity. This difference can also be observed on the corresponding spheroid composition graph and is highlighted by arrows. From day 0 to day 3, the spheroid composition in eGFP-OV1946 cells increases consistently. Between day 3 and day 4, eGFP-OV1946 cells are more affected by the treatment than mCherry-OV1946 cells, resulting in a steep decrease in eGFP spheroid composition. From day 4 to the end of the experiment, mCherry-OV1946 cell death reaches similar rates as eGFP-OV1946 cells and the spheroid composition stabilises.
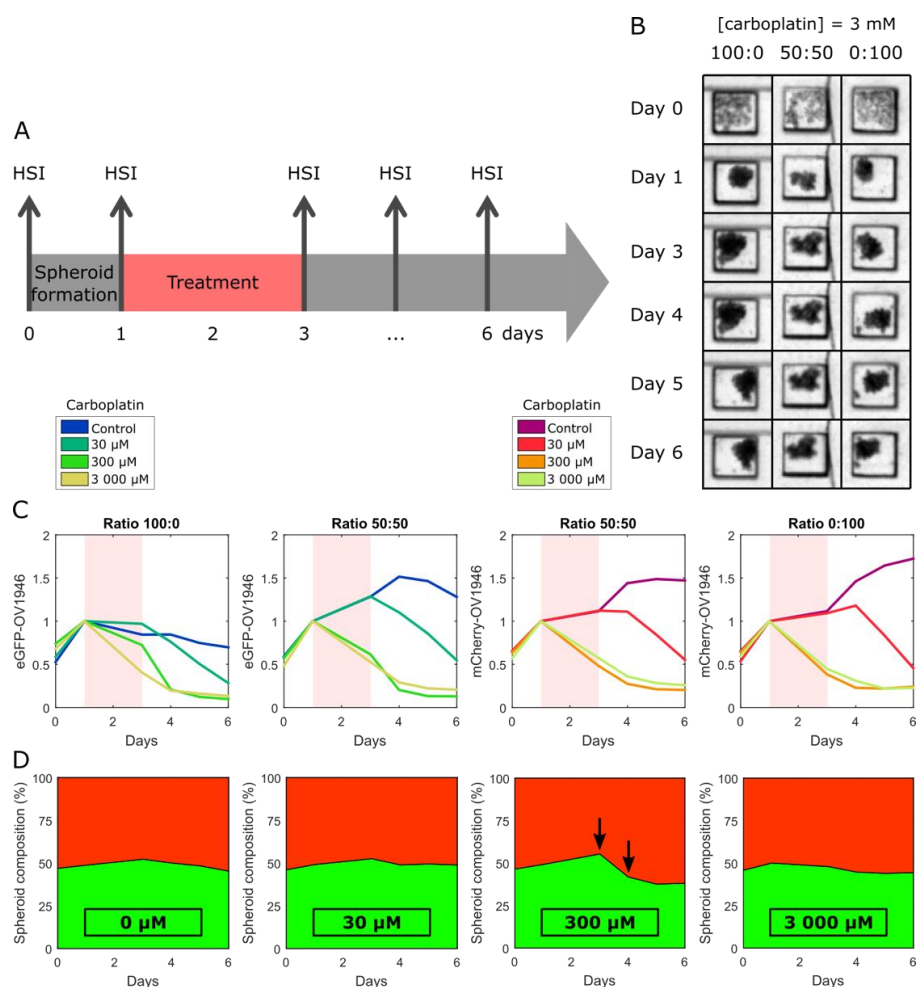
Figure 5-7: Treatment response assay using carboplatin. A) Experiment timeline. B) Brightfield images of spheroids over time, for a carboplatin concentration of 3 mM. For

a specific seeding ratio, the same spheroid is shown over time to observe its response to the drug. Brightfield images could not be acquired for 100:0-day 6 and 50:50-day 3. C i-ii) Day 1-normalised eGFP-OV1946 response to different concentrations of carboplatin, according to the initial seeding ratio. C iii-iv) Day 1-normalised mCherry-OV1946 response to different concentrations of carboplatin, according to the initial seeding ratio. D) Spheroid composition over time (bottom/green: eGFP; top/red: mCherry). Each curve represents the average of 24 spheroids (n = 1). Arrows indicate differences in behaviour of the two subclones.

5.5 Discussion and Conclusion

Many research groups have developed methods using various combinations techniques to study co-culture spheroids and follow their cell populations over time. Several of these methods are either based on destructive techniques such as digesting spheroids prior to analysis [85], [105], [108], cryosections [107], [108], or flow cytometry [105], [108], or on confocal microscopy [107]. These methods cannot achieve long term repeated analyses of the same spheroids over time while also sampling the centre of larger spheroids (> 70-100 µm). Our method, based on forming and treating spheroids on-chip, and following their fluorescence over time using wide-field hyperspectral imaging, has the advantages of being rapid, precise, and versatile. Multiple samples can be imaged in the wide field of view. We were able to measure 24 spheroids for 28 conditions each (7 ratios x 4 drug concentrations) in a single experimental run, taking approximately 4 hours to perform. If confocal or multiphoton imaging were to be done in 30 seconds for each spheroid, as it is customary, 5.6 hours would have been required just to perform the imaging step. The hyperspectral capabilities of the system can distinguish fluorophores with close emission peaks or fluorophores of low intensity overshadowed by a fluorophore of higher intensity, as demonstrated in our previous work [159]. Finally, since the excitation wavelength of the HSI system can be chosen between 400 and 700 nm and the emitted fluorescence can be measured from 450 to 720 nm, the system is highly versatile in terms of which fluorophores can be imaged. Overall, our microfluidic chip and our hyperspectral imaging system can generate and treat spheroids rapidly with an absolute error of less than 5% in spheroid composition compared to FACS analysis.

The 2D proliferation assay showed that one subclone, eGFP-OV1946, has a doubling time 1.5-times faster than the mCherry subclone when cultured separately. Cultured together at different seeding ratios, eGFP-OV1946 also proliferated faster than mCherry-OV1946 cells. This trend was

also observed in spheroids using the HSI system, although eGFP-OV1946 cell proliferation decreased starting at day 5 of spheroid culture. Our method to assess treatment response on ovarian cancer spheroids also illustrates how, depending on the cell line and drug studied, using fluorescence can detect treatment response earlier than the spheroid diameter.

We observed that a concentration as high as 50 µM was necessary to illicit a clear decrease in fluorescence, especially for eGFP cells, even if the 2D IC50 of both subclones is between 20 and 30 nM. At the 500 nM drug concentration (around 20X of the 2D IC_{50} for both cell lines), a slight decrease in fluorescence compared to the control and the 5 nM concentration was observed (Figure 5-5D-E). This result is typical of treatment response in 3D cultures, as the drug concentrations necessary to elicit a drug response are normally higher in 3D than in 2D[7]. Other experimental work in our laboratory also indicate that drug concentrations around 100X the 2D IC_{50} are necessary to elicit a response in ovarian cancer spheroids [121], [178].

One advantage of using HSI to follow cell populations over time is that we were able to measure treatment response of a cell population representing only 10% of the spheroid composition Figure 5-5D i and E iv). Typical studies on clonal population either can detect subclones of 10% but are destructive, or cannot follow over time such a low population [85], [105]. Our HSI system offers advantages in terms of imaging highly asymmetrical populations compared to conventional fluorescence microscopy where crosstalk can cause inaccuracy when measuring each population fluorescence intensity [112]. Finally, using the carboplatin treatment response results, we showed how breaks in the spheroid composition curve over time (Figure 5-7D ii-iii) can highlight changes in the cell populations response to treatment and indicate periods of interest to study treatment response.

In conclusion, this work introduces a novel method to rapidly and dynamically analyse the response to external stimuli of highly asymmetrical co-culture spheroids formed in microfluidic chips. As HSI has demonstrated it can image and quantify three or more fluorophores without increasing experimental time [159], mixing more than two types of cells, such as epithelial and stromal cells, resistant and sensitive cells, or cancer and immune cells could be done. Our work could be applied to other types of assays, such as drug penetration in tissue studies, invasion assay, or angiogenesis studies and could find applications in high throughput/high content drug screens on spheroids to

test new or known drugs on co-culture spheroids. HSI is also compatible with recently emerging *ex vivo* tumour on a chip models [179].

5.6 Materials and methods

5.6.1 Microfluidic chip

Spheroids were formed directly inside a microfluidic chip using a design and technique described previously [159]. The chip consists of a main channel of 2.5 mm in width and 500 µm in height with wells of 500 x 500 x 500 µm^3 placed underneath. 120 wells are placed in 5 groups of 24 to form spheroids using a single cell suspension. Spheroids stay trapped in the wells when the medium (containing drugs or not) in the main channel is changed using a low flow rate [45]. Photographs of the chip are presented in Figure 5-1.

Two poly(methyl methacrylate) (PMMA) moulds were micromachined using a computerised numerical control (CNC) machine (EMCO PC Mill 55, EMCO GmbH, Austria); one for the layer containing the main channel and inlets/outlets, and one for the layer containing the wells. Degassed poly(dimethylsiloxane) (PDMS, Sylgard® 184 silicone elastomer kit, Dow Corning, USA) mixed at a 10:1 ratio was then poured onto each PMMA mould and cured in an oven at 80 °C for 1 h. Both PDMS layers were exposed 30 s to an atmospheric plasma (Dyn-A-Mite, Enercon, USA) and bonded together to form the microfluidic chip. Hollow nylon cylinders (91145A138, McMaster-Carr, USA) were then introduced in the inlets and outlets.

Microfluidic chips were prepared for cell culture by first removing any bubbles in the channels using 100% ethanol followed by a 70% ethanol incubation for 10 minutes to sterilise the chip. Channel walls were then passivated to prevent cell adhesion to the PDMS by introducing a solution of triblock copolymer block (10 mg/mL, Pluronic® F-108, 542342, Sigma-Aldrich, USA) in the channels. Chips were put in a sterile humidity chamber (plastic box with a tissue moistened with sterile water) to prevent evaporation and incubated with the passivating solution for at least 1 h or overnight at 37 °C and 5% CO_2. A final sterilisation step of ethanol 70% for 10 minutes was followed by a rinsing of the channel with sterile Hank's Balanced Salt Solution (HBSS, 311-516-CL, Wisent Inc., Canada) supplemented with 600 µg/L amphotericin B (450-105-QL, Wisent Inc.)

and 55 mg/L gentamicin (450-135-XL, Wisent Inc.). Chips could then be stored at 4 °C or used immediately to form spheroids on-chip.

5.6.2 Co-culture spheroids

The ovarian cancer cell line OV1946 was previously established from patient ascites [35]. OV1946 cells possess the ability to form spheroids in low attachment conditions. Two fluorescent subclones were produced by transiently transfecting OV1946 cells with an eGFP plasmid (pEGFP-N1, 6085-1, Clontech Laboratories Inc., USA) and a mCherry plasmid (mCherry2-N1, #54517, Addgene, USA). Plasmid mCherry2-N1 was a gift from Michael Davidson. Successfully transfected cells were selected using G418 (500 µg/mL, Geneticin®, 10131-035, Thermo Fisher Scientific, USA). Single clones from each transfection were finally produced by limited dilution to obtain two OV1946 subclones expressing each fluorophore at the same level for all cells within a subclone.

Co-culture spheroids were formed on-chip by first mixing eGFP-OV1946 and mCherry-OV1946 cells at the following initial seeding ratios: 100:0, 90:10, 75:25, 50:50, 25:75, 10:90, and 0:100 (eGFP:mCherry). The total number of cells for all cell suspensions was 9×10^5 cells per millilitre of OSE medium without phenol red (316-031-CL, Wisent Inc.) supplemented with 10% foetal bovine serum (FBS, 080-150, Wisent Inc.), 55 mg/L gentamicin, 600 µg/L amphotericin B, and 500 µg/mL G418. Complete OSE medium supplemented with G418 is referenced throughout this work as "medium", except where specified.

Spheroids were formed on-chip on day 0 by introducing 100 µL of cell suspension in the plastic cylinder of the inlet and quickly removing 100 µL of liquid from the outlet. This step was repeated 6 times to ensure a uniform distribution of cells in the chip. 24 h later, one spheroid per well was visibly formed. Experiments were started on day 2. To remove cell wastes and replenish nutrients, medium was changed every 24 h by adding 70 µL of new medium in the inlet and removing 3 x 20 µL from the outlet to prevent ejecting spheroids from their well. Throughout the experiment, chips were incubated at 37 °C and 5% CO_2 while placed in a humidity chamber to prevent medium evaporation.

To perform a drug response assay using PARP inhibitors, talazoparib (HY-16106, MedChemExpress, USA) was first solubilised in dimethyl sulfoxide (DMSO) (D8418, Sigma-

Aldrich) at 20 mM. This solution was then diluted to 5 nM, 500 nM, and 50 μM in medium. DMSO was added to each solution, including the control, to match the final DMSO concentration of 0.25% (v/v) in the 50 μM solution. To perform a drug response assay using a chemotherapy drug, carboplatin (10 mg/mL, Omega Laboratories Limited, Canada) was diluted to 30, 300, and 3 000 μM in medium.

5.6.3 Hyperspectral imaging system

A custom-built hyperspectral imaging system was previously developed [159] to acquire fluorescence hyperspectral data cubes (pixel x pixel x nm) of multiple spheroids trapped in a microfluidic chip with a 22.6 line-pairs per millimetre spatial resolution and a 7 nm spectral resolution. The HSI system has a field of view of 7.25 mm in diameter and can image 24 wells/spheroids of the microfluidic chip described earlier. Briefly, the HSI system is composed of two illumination branches: a halogen white light (HL-2000, Ocean Optics, USA) is used for brightfield illumination and a supercontinuum laser (Fianium, NKT Photonics, Denmark) coupled to a laser line tuneable filter (LLTF, Photon etc, Canada) is used for fluorescence excitation at various wavelengths. The illuminations are combined using a 50:50 beamsplitter (BS013, Thorlabs, USA) towards the sample. A fixed focal length objective (59-871, Edmund Optics, USA), a longpass filter (FELH0500 or FELH0550, Thorlabs), a relay lens (67-422, Edmund Optics) and a liquid crystal tuneable filter (LCTF, VariSpec VIS, Perkin-Elmer, USA) form the sample image on an electron multiplying charged-coupled device (EMCCD) camera (HNü 512, Nüvü Caméras, Canada). A custom LabVIEW 2014 (National Instruments, USA) software sweeps the tuneable liquid crystal filter to acquire images at every 5 nm and measure the sample's fluorescence emission spectrum or transmittance.

In this work, excitation wavelengths used were 480 nm for eGFP and 530 nm for mCherry. The fluorescence emission spectra were acquired from 400 to 720 nm or 550 to 720 nm, depending on the excitation wavelength used. Typical acquisition time for an image at one wavelength was 500 to 1000 ms and gain was set at 500. For each microfluidic chip, the middle group of wells was imaged, resulting in 24 spheroids imaged per condition. For the comparison with flow cytometry, 3 groups of 24 spheroids were imaged per chip (72 spheroids in total).

Brightfield and fluorescence hyperspectral data cubes of each chip imaged were analysed with a series of steps described in detail in our previous study [159]. Briefly, each data cube was first divided by its acquisition time and gain. Dark noise acquired when closing the camera shutter was then subtracted. A shading correction was then applied to compensate for uneven illumination and detection.

5.6.4 Fluorescence image analysis

Hyperspectral data cubes were processed using MATLAB R2015a (The MathWorks, Inc., USA) to extract the fluorescence intensity emitted by each spheroid. Since the exact positioning of the chip in the field of view of the HSI system is different for each day and chip, regions of interest (ROI) corresponding to each well of the chip were determined by registering each image with a reference image, where well positions are known. Spectral unmixing is then performed on each selected ROI to separate each spectral entity contribution using a library of previously acquired fluorescence spectrum of the fluorophores of interest. The coefficients obtained for eGFP and mCherry were used as the fluorescence intensity emitted by each fluorescent protein. This is more precise than using the fluorescence intensity at the emission peak, especially in the case of overlapping fluorophores spectra.

Because of the limited dilution performed to select one clone after transfection, all the eGFP-OV1946 (or mCherry-OV1946) cells express the eGFP (or mCherry) protein at a very similar level. However, that intensity level is not the same for both fluorescent subclones. To be able to compare eGFP and mCherry intensities, both intensities need to be normalised. Fluorescence intensities at day 0 were averaged for all spheroids that had the same initial seeding ratio (all spheroids made at 25:75 were averaged at day 0 and fluorescence values were reported for eGFP 25% and mCherry 75%, regardless of the drug concentration tested after). A linear fit was performed, and the fit was then used to obtain an intensity for a spheroid made at 100% of each subclone. An example of this linear fit is presented in Figure 5-9. These reference intensities were used to normalise all acquired data. Spheroid composition was then calculated as follows:

$$\%_A = \frac{I_A}{I_A + I_B} \times 100 \tag{5-1}$$

where $\%_A$ is the percentage of the spheroid composed of subclone A, $I_{A/B}$ is subclone A/B normalised intensity for this spheroid.

5.6.5 FACS validation

Co-culture spheroids at various seeding ratios were formed on-chip according to the method described above. Spheroids were cultured on-chip and medium, supplemented with 0.25% (v/v) DMSO, was changed every day. The experiment was repeated three times and depending on the experiment repetition, spheroids were cultured 3, 4, or 6 days on-chip. Three groups of 24 spheroids were imaged by HSI per chip and their composition in eGFP and mCherry cells was calculated and averaged. On the same day, the chips were cut to separate the same three groups of 24 spheroids which were imaged. These spheroids were harvested from the chip by peeling apart the two layers of PDMS and collecting them in a 1.5 ml tube with 100 µl of phosphate buffered saline (PBS, 311-012-LL, Wisent Inc.). The spheroids were digested by adding 100 µl of trypsin 0.05% (325-041, Wisent Inc.) for 30 seconds. Trypsin was then neutralised by the addition of 200 µl of FBS. The single cell suspension obtained was centrifuged at 1 200 rpm for 10 minutes at 4 ℃, washed with PBS, and the pellet was reconstituted in FACS buffer [PBS supplemented with 2% FBS, 1 mM EDTA (EDT001, Bioshop, Canada), and 0.1% sodium azide (V015-05, JT Baker, USA)]. The samples were read in a BD LSRFortessa (BD Biosciences, Canada) cell analyser. Results were analysed with FlowJo v10 (FlowJo, LLC, USA).

5.6.6 2D proliferation assay

A 2D proliferation assay was performed to determine fluorescent subclone proliferation rates. A total of 750 cells from both subclones were seeded in 96-well plates in OSE medium. Cells were imaged using phase contrast and fluorescence imaging by the IncuCyte® S3 live-cell analysis system (Essen BioScience, USA). Frames were captured at 4-hour intervals in two separate regions per well using a 10X objective. Acquisition times were 350 ms for eGFP and 500 ms for mCherry. Proliferation data were calculated from phase contrast images and fluorescence confluence measurements using the IncuCyte® S3 software. Curves were constructed using Prism 6 (GraphPad Software, USA). Each experiment was performed in triplicate and repeated three times.

5.6.7 2D clonogenic assay

eGFP-OV1946 and mCherry-OV1946 cells were plated at 2 000 cells per well in distinct 6-well plates. The next day, talazoparib diluted in medium was added to the cells at several concentrations from 0 to 4 000 nM and cells were incubated for 7 days. Colonies were stained with methylene

blue 0.5% dissolved in methanol (41424, ThermoFisher Scientific) and counted under a stereo microscope. IC$_{50}$ values were calculated using Prism 6 (GraphPad Software). Each experiment was performed at least three times in duplicate.

5.7 Acknowledgements

5.8 Supplementary material
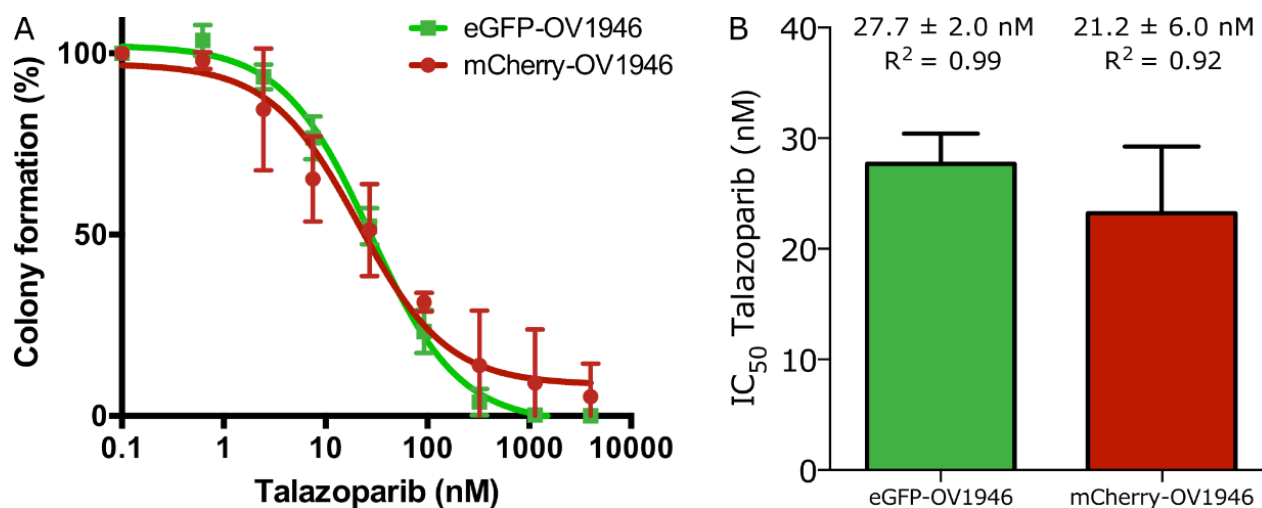
Figure 5-8: Determination of the 2D IC$_{50}$ by clonogenic assay for both subclones. A) Average dose-response curves for both subclones. B) Talazoparib IC$_{50}$ for eGFP-OV1946 and mCherry-OV1946, p = 0.655. Error bars represent the standard deviation (n = 3).
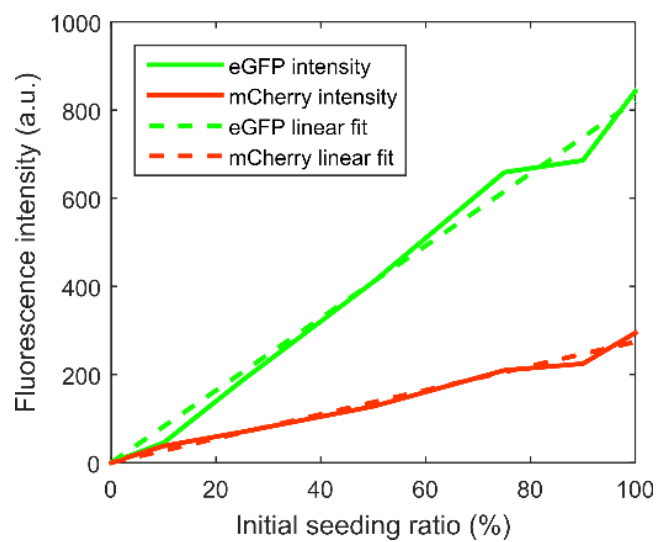
Figure 5-9: Reference intensity linear fitting for eGFP and mCherry fluorescence comparison.

CHAPTER 6   GENERAL DISCUSSION

The main goal of this thesis work was to provide a versatile and high-throughput analysis instrument to measure the fluorescence of 3D samples cultured in microfluidic chips. This was achieved by the development and validation of a wide-field hyperspectral imaging system compatible with *in situ* imaging of spheroids on-chip. The first article published on this work describes the HSI system design and its image processing algorithm. A proof-of-concept that wide-field hyperspectral imaging of spheroid fluorescence is possible is also presented. The second submitted article expands on spheroid imaging and illustrates how HSI can be used to study the effect of clonal heterogeneity in cancer. This chapter presents a general discussion of both articles, by first reviewing them in terms of each research objective. The limitations of this thesis work as well as the limitations of hyperspectral imaging are then discussed.

6.1 Development of a wide-field hyperspectral imaging system for spheroid analysis

The first research objective of this dissertation was to design and build a wide-field hyperspectral imaging system capable of measuring spheroid fluorescence. This was done by using a liquid crystal tunable filter to sweep across the emission spectra of the fluorophores imaged and acquiring one image per interrogated wavelength. Spectral unmixing was then used to quantify the fluorescence intensity of each fluorophore in the spheroids. A simple visual comparison of hyperspectral and confocal images of the same spheroids shows that HSI can acquire hyperspectral images of spheroid fluorescence and observe a degree of spatial distribution of two cell lines that do not mix homogeneously during co-culture (Figure 4-5).

A low numerical aperture objective was selected to image a large field of view and obtain a depth of field larger than typical spheroid diameters. Because of the use of this objective combined with the low transmission of the tunable filter (between 25% and 57% from 500 nm to 700 nm), a highly sensitive EMCCD camera was chosen. Being able to measure 24 spheroids in a single acquisition reduces experimental work and increases the statistical power of the results, as more replicates are analyzed, making it worthy to use this type of camera. When imaging spheroids one by one and assuming a 30 s acquisition time, a situation often necessary using confocal, multiphoton, and light sheet microscopy, imaging 28 conditions and 24 spheroids per conditions requires 5.6 hours.

Acquiring 24 spheroids in a single acquisition using the HSI system reduces this time to less than 3 hours of experimental work including acquiring the other datacubes necessary for the subsequent image analysis step (Table 4-1). By optimizing the microfluidic chip used to form spheroids, up to 60 spheroids could be imaged without increasing acquisition time (Figure 4-6). Microfluidic channels could also be designed to image multiple conditions in the same image.

The HSI system has a spatial resolution of 22.6 line pairs per millimetre, or 44.2 μm resolution over a circular field of view of 7.25 mm in diameter, or 41 mm^2. This spatial resolution is sufficient to image spheroids of a few hundreds of micrometres in diameter. The spectral resolution of the HSI system is 7 nm and is also sufficient to unmix fluorophores with overlapping spectra (Figure 4-3). To analyze the acquired hyperspectral datacube automatically and quantitatively, a custom Matlab algorithm was developed and implemented. As the measured spatial intensity of a homogeneous sample was not uniform, due to the illumination and detection optics, a shading correction step was added to the image analysis algorithm. While this step allows for comparing fluorescence intensities across the wide field of view, it decreases the total range of fluorescence intensities that the system can measure, as samples with low fluorescence levels that are at the periphery of the image could be below the higher instrument noise floor of the image periphery. Also, the noise at the image periphery is amplified by the necessary multiplication with the compensation matrix (section 4.5.3) used to apply the shading correction.

The hyperspectral imaging system can also be compared with other imaging techniques in terms of resolution or capabilities, as detailed in Table 6-1. Hyperspectral imaging as the advantage of a higher spectral resolution compared to other imaging techniques that rely on filter cubes. While the HSI system described here does not provide any imaging advantage compared to a confocal microscope, since the HSI system spatial resolution is much lower than the confocal microscope used in Figure 4-5, its main advantage resides in the number of fluorophores that hyperspectral imaging systems can resolve. At least one detection channel per imaged fluorophore is necessary to spectrally unmix them. Contrary to multiphoton imaging and light sheet microscopy, the HSI system is able to image spheroids trapped in thicker microfluidic chips in a high-throughput manner. The versatility of hyperspectral imaging can also be used to investigate which spectral bands are ideal to analyze specific samples. The imaging system can then be optimized to utilize those selected bands to accelerate the analysis using either the same imaging system or a second instrument.

Table 6-1: Comparison of hyperspectral imaging to other imaging techniques

Comparison point	Hyperspectral imaging	Epifluorescence imaging	Confocal imaging	Multiphoton imaging	Light sheet microscopy
Spectral resolution	< 10 nm	> 30 nm	> 30 nm	> 30 nm	> 30 nm
Imaging up to the spheroid centre	Yes	Yes	No	Yes, up to a certain diameter	Yes
Acquisition time for 1 spheroid	1 s per wavelength (45 s)	10 s	30 s	30 s	30 s
Acquisition time for 24 spheroids	1 s per wavelength (45 s)	10 s (using lower magnifications)	24 x 30 s	24 x 30 s	24 x 30 s
High-throughput imaging of microfluidic chips	Yes	Yes	Yes	No	No

The image analysis algorithm was also designed to extract regions of interest in each image corresponding to each of the 24 wells containing spheroids. Using the current version of the algorithm, the active user time required to analyze 28 conditions applied to 24 spheroids over 10 days (the equivalent of 6 720 spheroids or data-points) is about 8 hours. An additional computing time of around 30 hours is also necessary but can be scheduled during the night and requires no input from the user. This computing time is mainly due to the spectral unmixing performed on each of the 262 144 pixels (512 x 512 pixels) of the hyperspectral datacubes.

In addition to ovarian cancer spheroids, other types of 3D cultures were imaged throughout this thesis work. Figure 6-1 present three types of 3D cultures that the HSI system successfully imaged. Using microfluidic chip B, Maeva Bavoux, a master's student in our laboratory, formed sarcoma spheroids using cell line STS117. She then stained them with a live cell fluorescent marker, CellTracker™ Green (CTG), and a dead cell marker, propidium iodide (PI). Figure 6-1A shows the resulting brightfield and fluorescence images at both fluorophores' emission peaks, 515 nm for CTG and 610 nm for PI. Our laboratory has also developed a method to microdissect tissue obtained from mice xenograft or human biopsies into submillimetre spheres [44]. The microtissues are then loaded in microfluidic chip A, a chip designed to trap and maintain in culture 5 microtissues. Here, mice xenografts were made from eGFP-expressing OV1946 cells by Adriana Mari Orimoto and Kim Leclerc Desaulniers. The grown tumour was harvested and cut into spheres of 380 μm in diameter. The fluorescent microtissues were then loaded in the wells of microfluidic chip A and imaged using the HSI system. Figure 6-1B shows the brightfield, fluorescence emission

(at 515 nm) and transmittance (at 515 nm) images of three microtissues. As a third example, prostate cells RWPE-1 were cultured on a Matrigel™ layer in a 6-well plate by Andrée-Anne Grosset and Mame Kany Diop and formed tubular structures in 12 days. These 3D structures were then stained with calcein AM (live cell stain) and Ethidium-homodimer 1 (EthD-1, dead cell stain), and imaged using the HSI system. Figure 6-1C shows the brightfield and fluorescence images for calcein AM and EthD-1. The HSI system was able to measure the emitted fluorescence of these 100 μm-in height structures.
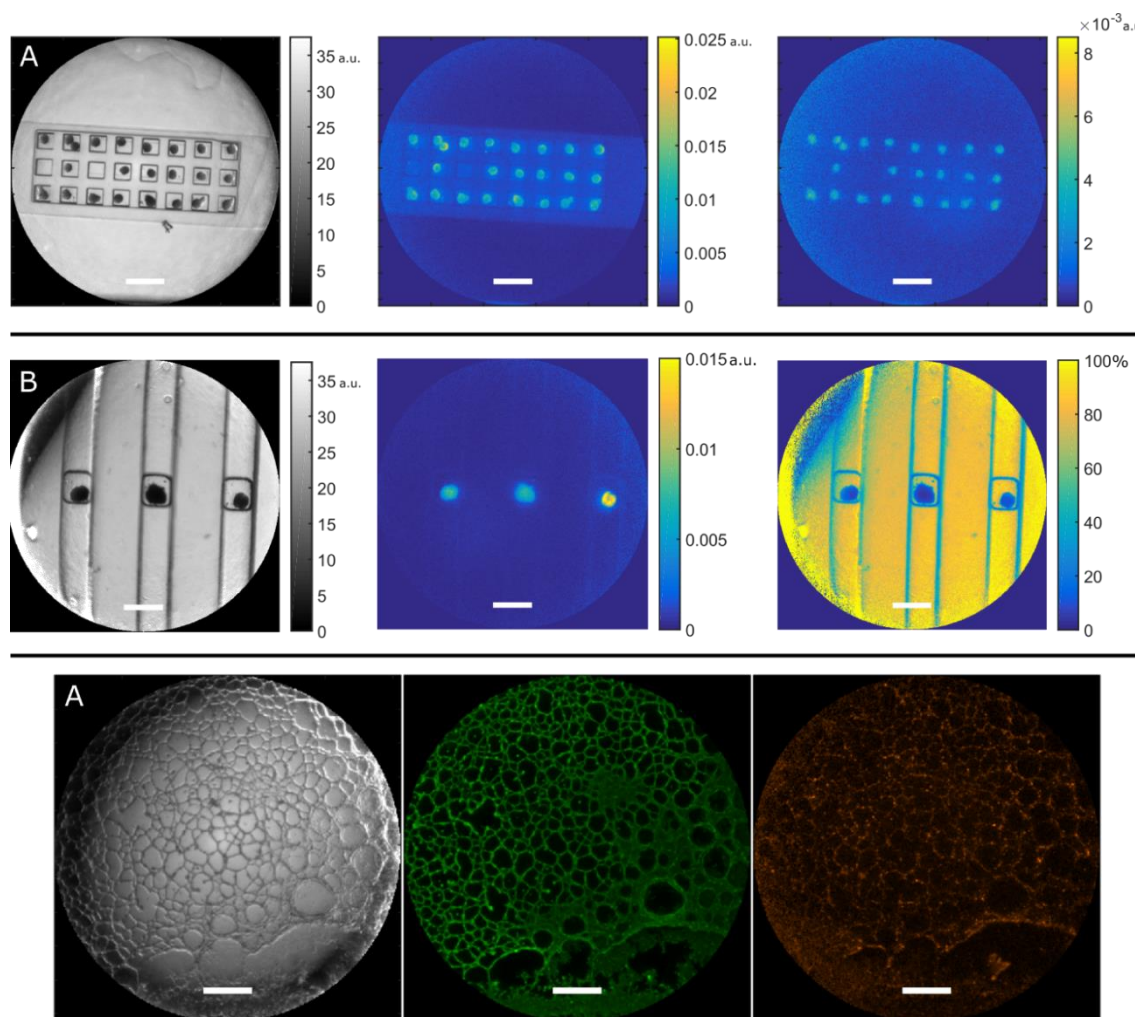
Figure 6-1: 3D cultures imaged using the HSI system. A) STS117 spheroids, formed, stained by CellTracker™ Green and propidium iodide [i) Brightfield (720 nm), ii) CTG fluorescence (515 nm), and iii) PI fluorescence (610 nm) images]. B) EGFP-expressing microdissected mouse xenografts loaded on chip [i) Brightfield (720 nm), ii) fluorescence (515 nm), and iii) transmittance (515 nm) images]. C) Prostate cells forming tubules on Matrigel™, formed

and stained with calcein AM and EthD-1 [i) Brightfield (720 nm), ii) calcein AM fluorescence (515 nm) and, iii) EthD-1 fluorescence (615 nm) images]. Scale bars = 1 mm.

6.2 Validation of the fluorescence quantification capabilities of the HSI system

After confirming that the HSI system could detect spheroid and other types of 3D culture fluorescence, the quantification capabilities of the system were validated using optical phantoms of known fluorophores and elastic scattering properties (Figure 4-4). In doing so, the geometric factor α of equation was optimized for slab-like sample geometries. This α value depends on the sample geometry and on any changes to the optical components of the HSI system. Once α was determined, transmittance-based equation (4-1) was able to compensate for a wide range of scattering properties encompassing those of the spheroids. The HSI system is thus able to quantify fluorescence for slab-shaped phantoms having scattering properties, μ_s', ranging from 0.5 to 7.5 cm^{-1}. A major limitation of this transmittance-based quantification is that, for highly attenuating samples, the measured transmittance is null and equation (4-1) cannot be applied. This could lead to larger spheroids being impossible to analyze using this equation. A solution would be to increase the acquisition time or gain of the camera or the white light illumination intensity. However, since the microfluidic chip is made of transparent PDMS, pixels around the sample will then saturate. In the case of the EMCCD camera used here, pixel saturation can damage the camera and must be prevented. Still, the image analysis algorithm and equation (4-1) were proven able to quantify fluorescence for a specific scattering properties range.

A second type of validation was performed to assess if HSI can measure the spheroid composition in terms of percentage of each cell population. For this validation, flow cytometry was used as the gold standard technique. It was found that HSI measurements varied in spheroid composition percentage from flow cytometry results from at most 5%, a small absolute error considering the many processing steps prone to cell loss necessary for flow cytometry measurements versus *in situ* HSI. As HSI measurements are done without perturbing the spheroids, loosely aggregated cells located in the wells can be included in the measurements. For flow cytometry analysis, the layers forming the microfluidic chip are separated and spheroids are manually pipetted into tubes to be

digested into single cells. Each of these steps can add errors to the final measurement. Still, both techniques yielded results with an absolute difference of at most 5% in spheroid composition.

Finally, preliminary Monte Carlo light propagation simulation results, presented in Appendix B, shows that, when simulating the trajectory of excitation photons and generated fluorescence photons detected by the camera, fluorescent molecules with fluorescence properties similar to eGFP that are located at the spheroid centre are as much excited and detected than molecules in the outer layers. This is an advantage of HSI compared to confocal imaging of larger spheroids. However, estimating the exact value of the scattering coefficient of ovarian cancer spheroids is a challenge. For this simulation, as for the optical phantoms experiment, only two references explicitly stating the optical properties of tumour spheroids made from other cell lines were found [156], [157]. As spheroid compactness depends on the cell type used to form spheroids, ovarian cancer spheroid optical properties will differ from value found in the literature. Still, unless the optical properties of ovarian cancer spheroid (of each cell line available) are measured, those two references represent the best estimation available.

6.3 On-chip hyperspectral imaging of co-culture spheroids to study clonal heterogeneity

This final research objective was completed by first establishing a general workflow that incorporated HSI into a spheroid-based assay, as presented in Figure 5-1. One advantage of this workflow is that the same spheroids are imaged daily to see their dynamic response to external stimuli, such as drug treatments. In a typical end-point assay, where read-out techniques are destructive, the optimal time during the experiment to perform the end-point assay to observe treatment response is not known *a priori* and needs to be assessed in preliminary experiments. Cells can respond to drug in a few hours or a few days. Timing the end-point measurement is thus critical. Being able to dynamically follow the response eliminates this problem. Furthermore, dynamic measurements are able to detect if the cell populations in the spheroid do not respond at the same rate, independently of the intensity of their response. Arrows on Figure 5-7 illustrate this concept. If, for any reason, hyperspectral imaging is not sufficient for the study purposes, it could be used instead to optimize the ideal time when end-point assays should be performed.

Finally, the HSI system and its image algorithm were used to perform two complete experiments on cell population growth and treatment response in co-culture spheroids. A comment can be made about what happens to fluorescent proteins when cells die. If cells remain fluorescent after death, it could impact the validity of the results. A research group [180], [181] used genetically modified fluorescent cells and investigated if a decrease in eGFP fluorescence as an indicator of cell death compared to gold standard flow cytometry measurements using the apoptosis stain Annexin V. Their results showed that both methods detected similar amount and kinetics of cell death in monolayer cultures. They also proved that, for the cell lines they used, the decrease in fluorescence at cell death is not due to a leakage of the fluorescent proteins outside the cells [181]. In the case of spheroids, leaked proteins could accumulate and be trapped between the cells and reduce HSI measurement precision. The authors suggest other factors such as pH and redox changes leading to fluorescence quenching or protein denaturation could be responsible instead. While the exact mechanism is not known, they showed that a decrease in eGFP fluorescence can measure cell death. In this dissertation, cell death due to drug exposure (talazoparib and carboplatin) was observed 48 h after the first exposure, which corresponds to 1 or 2 cell divisions, as the average 2D doubling time of each subclone was 25 h and 37 h (Figure 5-2). This is consistent with the mechanism of action of those two chemotherapy drugs, as they affect cells during their division.

6.4 Limitations of this thesis work

The goal of this thesis work was to develop and validate a versatile hyperspectral imaging system to study co-culture spheroids trapped in microfluidic chips. This goal was achieved, as described previously. However, improvements on microfluidic chip design, on the HSI system, on fluorescence quantification validation and on the type of spheroid-based experiments can be identified.

First, as illustrated in Figure 4-6, a simple chip redesign could be done to multiply the number of spheroids in the field of view by 2.5 and image 60 spheroids. Or, instead of imaging 60 spheroids exposed to one condition, a microfluidic design could be used to study 3 conditions on 20 spheroids each. The 7.25 mm in diameter field of view of the HSI system opens up many possibilities that were not investigated up to this point.

One current limitation of the HSI system in its actual form is a high excitation laser bleed-through intensity. This intensity is sometimes of similar intensity to the fluorophores of interest. This render detecting fluorophores of low intensity challenging. Shortpass filters corresponding to the excitation wavelengths were added to the system and used throughout this dissertation to try to minimize this effect but were unable to remove all the excitation bleed-through contamination of the spectra. More work needs to be done to improve this problem.

Two fluorescent subclones were created using eGFP and mCherry plasmids. Because of the time constraints during this thesis, those two fluorescent proteins do not take advantage of the full capabilities of hyperspectral imaging as the two fluorophores require different excitation wavelengths. At the beginning of this project, the goal was to use a fluorescent protein with a larger Stokes shift as the second fluorophore in order to use the same excitation wavelength for both. However, difficulties during the transfection process led to using the only two fluorophores that were successfully transfected in OV1946 cells. A similar transfection problem led to OV1946 subclones of similar resistance to talazoparib and carboplatin. Ideally, a sensitive population would have been tested alongside a resistant one. This type of problem represents one of the challenges of using genetically modified cell lines: some cell lines are able to reject plasmid transfection. In return, once cell lines are modified, experiments are simplified as no external stains or additional experimental step are necessary before fluorescence imaging. Furthermore, since the HSI system demonstrated that it can discriminate three spectral entities (CTG, CTO and bleed-through, Figure 4-3G-H), co-culture spheroids composed of three cell populations could also be done, once the bleed-through and transfection problems are corrected.

Another major limitation of the current work is that the fluorescence quantification algorithm, equation (4-1), designed to compensate optical properties, was only tested on slab-like optical phantoms. Since the geometric parameter α depends on the sample geometry, no fluorescence quantification was done on hyperspectral images of spheroids. Since microfluidic chips have been used extensively to form droplets and hydrogel beads [79], preliminary experiments were performed by a student (Alexandre Chabot, Appendix A). 300 μm-diameter droplets were easily made using two typical microfluidic modules: T-junctions and hydrodynamic flow-focusing modules. The student then worked on forming droplets of alginate mix with a scattering agent in a calcium-infused oil phase. The calcium is used to cross-link the alginate into a hydrogel. Hydrogel beads containing Intralipid were produced but presented stability problems that need further

investigation. Once this limitation is overcome, analyzing spheroids of various compactness will be more precise, as their varying optical properties will be considered.

Finally, a modification to the Mann-Kendall statistical test designed to detect monotonic trends was developed during this dissertation to analyze Mohana Marimuthu's results (Appendix C). In the work presented in article 2, both cell populations prove to be of similar drug resistance levels. If different resistance levels had been observed, the modified Mann-Kendall test would have been interesting to test if cell populations respond monotonically as a function of their initial amount. It also would have been interesting to perform further experiments to assess how cell populations can interact.

6.5 Limitations of hyperspectral imaging for 3D culture

In this dissertation, hyperspectral imaging was used to quantify cell populations in spheroids, with some advantages and limitations compared to other techniques. The main advantage of hyperspectral imaging over flow cytometry and tissue slicing analysis technique is the non-destructive nature of imaging. Spheroids can be followed over time to measure the individual response of each spheroid, instead of the average response of many spheroids at the end-point. The drawback is that, contrary to analyzing individual cells or tissue slices, imaging-based fluorescence intensity measurements of 3D cultures will be affected by the optical properties of the sample. By imaging spherical phantoms of known optical properties or performing Monte Carlo light propagation simulations, this effect could be quantified and taken into account during measurements.

HSI is a non-destructive method relying on fluorescence intensity to characterize spheroids, instead of optical sectioning where cells can be visualized and counted even if the fluorescence level varies from cell to cell. Because of this, its application to study samples where each cell from one population does not emit similar levels of fluorescence is limited. Microscopy techniques using optical sectioning, such as confocal, multiphoton, and light sheet microscopy, have the advantage of counting individual cell. To use HSI, some cell lines can be easily modified to express fluorescent proteins, while others reject the transfection, limiting the range of cells that can be studied. Another possibility is to stain cells uniformly so that they emit the same fluorescence level. Uniform staining can be done on a cell suspension and spheroid can be made using those

fluorescent cell suspensions. One problem associated with this technique to follow spheroids over time is that fluorescent molecules from the stain will be passed to daughter cells during division, decreasing the fluorescence intensity of each cell as the population divides. Difficulties also arise when staining microdissected xenograft or biopsy tissue. To preserve the structure of the tissue, transfection with fluorescent proteins to create fluorescent clones cannot be done. These samples can instead be stained with viability markers but each cell type present in the sample will typically stain at different levels. Furthermore, all cells will be stained, and cell populations will not be discriminated.

The second objective of this work was to validate the fluorescence quantification capabilities (equation (4-1)) of the HSI system, among other things. Article 1 showed that the HSI system can be used to compensate optical properties and quantify the fluorescence emitted by samples of a slab-like geometry. While preliminary work on spherical optical phantoms mimicking spheroids has been started, evaluating the optical properties of ovarian cancer spheroids is still a challenge. Since only two references were found on spheroid optical properties, achieving fluorescence quantification with equation (4-1) on real spheroid sample is challenging.

CHAPTER 7   CONCLUSION AND RECOMMENDATIONS

The aim of this project was to provide a versatile and high-throughput analysis instrument to measure the fluorescence of 3D culture cultured in microfluidic chips. Hyperspectral imaging was used to quantify cell population fluorescence as a response to external stimuli. While the HSI system is functional and used by other researchers, improvements can still be made. This chapter details recommendations on how to improve the HSI system.

7.1 Recommendations to improve the hyperspectral imaging system to study 3D *in vitro* cancer models

Despite the intensive work of two research interns as well as that of the author, the hardware and software of the HSI system could still be improved to optimize the ease of use of the system. Currently, while everything is functional during the acquisition of a hyperspectral datacube, many steps are still manual. Two computer-controlled motorized filter wheels could replace the manual versions currently in place to prevent any acquisition errors where a user forgets to change the required filters. Also, only the white light source is automatically controlled by the custom designed Labview program presented in section 4.5.2. The excitation laser for fluorescence measurements could be automatically controlled to select the desired excitation wavelength and to turn it on and off at the right moment. Manually changing the filters and the excitation wavelength was one of the main sources of error during acquisition.

The acquisition time and gain of the camera were kept constant at every wavelength for a specific sample. They are currently adjusted by manually acquiring images at the fluorescence peak at various acquisition times and gain and the parameters leading to the highest detected fluorescence intensity without saturating the camera are selected. To improve the signal to noise ratio at other wavelengths, this optimization could be done at every wavelength, instead of only at the fluorescence peak.

While the Labview program automatizes the acquisition of hyperspectral datacubes by acquiring images at every chosen wavelength automatically, it does not guide the user throughout the multiple acquisitions necessary for the subsequent image analysis steps, such as dark noise, bleed-through, and system transmission acquisitions (top part of Table 4-1). Thus, a major overhaul of

the program will need to be done before non-technical users can perform the acquisition themselves.

Finally, a similar overhaul will be necessary for the Matlab-based image analysis algorithm, presented in Figure 4-2, to shorten the analysis time of the large number of images associated with each experiment. For example, a typical 10-day experiment on 28 conditions (one microfluidic chip per condition) will generate more than 560 hyperspectral datacubes or 25 000 wavelength-images (45 interrogated wavelengths per datacube). In its current form, many steps of the current image analysis algorithm are manual. A first version of this overhaul was done by Didier Blach-Laflèche and is presented at the end of Appendix A. Yet, we anticipate that, should the HSI system be turned into a commercial product, less than one month of work by a team of skilled engineers would be required to make the acquisition software and the image analysis algorithm robust and easy to use.

Completing both the Monte Carlo light propagation study and the spherical optical phantom experiments will improve our understanding of HSI and its ability to quantify spheroid fluorescence. Completion of the Monte Carlo light transport simulation will first confirm that hyperspectral imaging is able to detect fluorescence from all cells composing the spheroid. Simulations can also be done to evaluate at which spheroid diameter does the sampling volume diminishes, or what is the effect of the PDMS layers on fluorescence quantification. The simulations can also be used to simulate the transmittance and fluorescence of samples of different geometries and evaluate the α parameter in equation (4-1) and its capabilities to quantify fluorescence. Secondly, by completing the experimental validation of equation (4-1) on spherical optical phantom, the HSI system will be able to quantify fluorescence in spheroids, improving the precision when quantifying fluorophores. Finally, similar quantification could be done on larger 3D cultures, such as slice cultures [182] or precision-cut liver slices [183].

In addition to fluorescence-based measurements of 3D *in vitro* cancer models, the HSI system could be used to measure changes in transmittance of the samples. One example could be to identify regions in a biopsy with a high content of blood, as the hemoglobin absorbance spectrum is known. It would also be interesting to investigate if transmittance measurements could quantify non-fluorescent immunostaining of whole spheroids.

7.2 Outlook

As 3D *in vitro* cancer models gain more and more attention as models that better represent cell-cell and cell-matrix interactions inside human tumours, there is a need to develop versatile analysis techniques and instruments to study these 3D models. During this thesis work, I designed and built a functional version of the HSI system and validated its performances to follow specific cell population response in 3D spheroids to external stimuli. My work involved designing and building a few versions of the HSI system, writing the Matlab analysis algorithm to extract the fluorescence emitted by each spheroid of the image, and validation the fluorescence quantification algorithm to compensate optical properties. The results on the dynamic response to chemotherapy of two cell populations in spheroids made on-chip generated great interest in our collaborators laboratories at the Centre de recherche du CHUM (CRCHUM). Researchers are eager to try the HSI system and, currently, experiments on sarcoma and prostate 3D cultures are ongoing.

Once a few modifications to the HSI system are made to increase its ease-of-use, research biologists will be able to use the system themselves. A myriad of experiments can be thought of, such as forming spheroids on-chip with more than two fluorescent cell types and observing their response to drugs and their effect on each other. Combinatorial studies can also be done, such as a current collaborative project with Dr. Philip Wong (CRCHUM) on studying spheroid response to radiotherapy and drug combinations to treat soft tissue sarcoma. In conclusion, the hyperspectral imaging system and its image analysis algorithm developed here have proven themselves as a versatile instrument that can easily follow the response of dozens of spheroids on-chip, measuring the dynamic response pattern of each cell population individually. Because of its versatility in acquiring both the fluorescence and transmittance spectra of the studied samples, I firmly believe that hyperspectral imaging can benefit and accelerate spheroid-based research.

REFERENCES

[1]   Canadian Cancer Society's Advisory Committe on Cancer Statistics, "Canadian Cancer Statistics 2017," 2017.

[2]   D. S. Miller *et al.*, "Phase II Evaluation of Pemetrexed in the Treatment of Recurrent or Persistent Platinum-Resistant Ovarian or Primary Peritoneal Carcinoma: A Study of the Gynecologic Oncology Group," *J. Clin. Oncol.*, vol. 27, no. 16, pp. 2686–2691, 2009.

[3]   N. G. Alkema, G. B. A. Wisman, A. G. J. Van Der Zee, M. A. T. M. Van Vugt, and S. De Jong, "Studying platinum sensitivity and resistance in high-grade serous ovarian cancer: Different models for different questions," *Drug Resist. Updat.*, vol. 24, pp. 55–69, 2016.

[4]   F. Pampaloni, E. G. Reynaud, and E. H. K. Stelzer, "The third dimension bridges the gap between cell culture and live tissue.," *Nat. Rev. Mol. Cell Biol.*, vol. 8, no. 10, pp. 839–45, 2007.

[5]   P. Tofilon, N. Buckley, and D. Deen, "Effect of cell-cell interactions on drug sensitivity and growth of drug-sensitive and -resistant tumor cells in spheroids," *Science (80-.).*, vol. 226, no. 4676, pp. 862–864, 1984.

[6]   K. Stock *et al.*, "Capturing tumor complexity in vitro: Comparative analysis of 2D and 3D tumor models for drug discovery," *Sci. Rep.*, vol. 6, p. 28951, 2016.

[7]   J. Friedrich, R. Ebner, and L. A. Kunz-Schughart, "Experimental anti-tumor therapy in 3-D: Spheroids – old hat or new challenge?," *Int. J. Radiat. Biol.*, vol. 83, no. 11–12, pp. 849–871, 2007.

[8]   T. Rodrigues *et al.*, "Emerging tumor spheroids technologies for 3D in vitro cancer modeling," *Pharmacol. Ther.*, vol. 184, pp. 201–211, 2018.

[9]   A. Salomon-Perzyński, M. Salomon-Perzyńska, B. Michalski, and V. Skrzypulec-Plinta, "High-grade serous ovarian cancer: the clone wars," *Arch. Gynecol. Obstet.*, vol. 295, no. 3, pp. 569–576, 2017.

[10]   N. C. Turner and J. S. Reis-Filho, "Genetic heterogeneity and cancer drug resistance," *Lancet Oncol.*, vol. 13, no. 4, pp. e178-85, 2012.

[11]   M. Zietarska *et al.*, "Molecular Description of a 3D In Vitro Model for the Study of

Epithelial Ovarian Cancer (EOC)," *Mol. Carcinog.*, vol. 46, pp. 872–885, 2007.

[12]   L. P. Ferreira, V. M. Gaspar, and J. F. Mano, "Design of spherically structured 3D in vitro tumor models -Advances and prospects," *Acta Biomater.*, vol. 75, pp. 11–34, 2018.

[13]   K. Moshksayan *et al.*, "Spheroids-on-a-chip: Recent advances and design considerations in microfluidic platforms for spheroid formation and culture," *Sensors Actuators, B Chem.*, vol. 263, pp. 151–176, 2018.

[14]   E. C. Costa, A. F. Moreira, D. de Melo-Diogo, V. M. Gaspar, M. P. Carvalho, and I. J. Correia, "3D tumor spheroids: an overview on the tools and techniques used for their analysis," *Biotechnol. Adv.*, vol. 34, pp. 1427–1441, 2016.

[15]   M. Makale *et al.*, "Extended-working-distance multiphoton micromanipulation microscope for deep-penetration imaging in live mice and tissue," *J. Biomed. Opt.*, vol. 14, no. 2, p. 024032, 2009.

[16]   J. Andilla *et al.*, "Imaging tissue-mimic with light sheet microscopy: A comparative guideline," *Sci. Rep.*, vol. 7, no. 1, p. 44939, 2017.

[17]   C. St-Pierre, "Modélisation et représentation dans l'espace des phénomènes photoniques inélastiques en biophotonique," École Polytechnique de Montréal, 2017.

[18]   R. L. Siegel, K. D. Miller, and A. Jemal, "Cancer statistics, 2018," *CA. Cancer J. Clin.*, vol. 68, pp. 7–30, 2018.

[19]   L. A. Torre *et al.*, "Ovarian cancer statistics, 2018," *CA. Cancer J. Clin.*, 2018.

[20]   M.-L. Puiffe *et al.*, "Characterization of Ovarian Cancer Ascites on Cell Invasion, Proliferation, Spheroid Formation, Gene Expression in an In Vitro Model of Epithelial Ovarian Cancer," *Neoplasia*, vol. 9, no. 10, pp. 820-IN8, 2007.

[21]   V. M. Peterson *et al.*, "Ascites analysis by a microfluidic chip allows tumor-cell profiling," *Proc. Natl. Acad. Sci.*, vol. 110, no. 51, pp. E4978–E4986, 2013.

[22]   V. Malhotra and M. C. Perry, "Classical Chemotherapy: Mechanisms, Toxicities and the Therapeutc Window," *Cancer Biol. Ther.*, vol. 2, no. sup1, pp. S2–S4, 2003.

[23]   S. Kummar *et al.*, "Advances in using PARP inhibitors to treat cancer," *BMC Med.*, vol. 10, no. 1, p. 25, 2012.

[24] H. Fleury *et al.*, "Cumulative defects in DNA repair pathways drive the PARP inhibitor response in high-grade serous epithelial ovarian cancer cell lines," *Oncotarget*, 2016.

[25] J. de Bono *et al.*, "Phase I, dose-escalation, two-part trial of the PARP inhibitor talazoparib in patients with advanced germline BRCA1/2 mutations and selected sporadic cancers," *Cancer Discov.*, vol. 7, no. 6, pp. 620–629, 2017.

[26] B. Kaufman *et al.*, "Olaparib Monotherapy in Patients With Advanced Cancer and a Germline BRCA1/2 Mutation," *J. Clin. Oncol.*, vol. 33, no. 3, pp. 244–250, 2015.

[27] L. Cancian and D. Cohen, "Health Canada approves LYNPARZA^{TM} for the Treatment of Ovarian Cancer with BRCA-Mutations," 2016. [Online]. Available: https://www.astrazeneca.ca/en/media/press-releases/2016/health-canada-approves-lynparza.html#. [Accessed: 07-Aug-2018].

[28] T. Voskoglou-Nomikos, J. L. Pater, and L. Seymour, "Clinical Predictive Value of the in Vitro Cell Line , Human Xenograft , and Mouse Allograft Preclinical Cancer Models 1," *Clin. Cancer Res.*, vol. 9, no. 11, pp. 4227–39, 2003.

[29] M. P. Ponnusamy, P. Seshacharyulu, A. Vaz, P. Dey, and S. K. Batra, "MUC4 stabilizes HER2 expression and maintains the cancer stem cell population in ovarian cancer cells.," *J. Ovarian Res.*, vol. 4, no. 1, p. 7, 2011.

[30] L. D. Dunfield, T. G. Shepherd, and M. W. Nachtigal, "Primary culture and mRNA analysis of human ovarian cells," *Biol. Proced. Online*, vol. 4, no. 1, pp. 55–61, 2002.

[31] I. J. Létourneau *et al.*, "Derivation and characterization of matched cell lines from primary and recurrent serous ovarian cancer," *BMC Cancer*, vol. 12, p. 379, 2012.

[32] Rama, "Lab mouse mg 3216," 2008. [Online]. Available: http://commons.wikimedia.org/wiki/Mus?uselang=en-gb#mediaviewer/File:Lab_mouse_mg_3216.jpg. [Accessed: 01-Jul-2014].

[33] A. E. Green, A. A. Garcia, S. Ahmed, and J. E. Harris, "Ovarian Cancer," *Medscape*, 2014.

[34] C. M. Beaufort *et al.*, "Ovarian Cancer Cell Line Panel (OCCP): Clinical Importance of In Vitro Morphological Subtypes," *PLoS One*, vol. 9, no. 9, p. e103988, 2014.

[35] V. Ouellet *et al.*, "Characterization of three new serous epithelial ovarian cancer cell lines.,"

BMC Cancer, vol. 8, p. 152, 2008.

[36]   D. M. Provencher *et al.*, "Characterization of four novel epithelial ovarian cancer cell lines," *Vitr. Cell. Dev. Biol. - Anim.*, vol. 3, pp. 357–361, 2000.

[37]   J. Friedrich, C. Seidel, R. Ebner, and L. A. Kunz-Schughart, "Spheroid-based drug screen: considerations and practical approach," *Nat. Protoc.*, vol. 4, no. 3, pp. 309–324, 2009.

[38]   A. Abbott, "Biology's new dimension," *Nature*, vol. 424, no. August, pp. 870–872, 2003.

[39]   A. Frankel, R. Buckman, and R. S. Kerbel, "Abrogation of taxol-induced G2-M arrest and apoptosis in human ovarian cancer cells grown as multicellular tumor spheroids," *Cancer Res.*, vol. 57, no. 12, pp. 2388–2393, 1997.

[40]   F. Hirschhaeuser, H. Menne, C. Dittfeld, J. West, W. Mueller-Klieser, and L. A. Kunz-Schughart, "Multicellular tumor spheroids: an underestimated tool is catching up again.," *J. Biotechnol.*, vol. 148, no. 1, pp. 3–15, 2010.

[41]   A. Fatehullah, S. H. Tan, and N. Barker, "Organoids as an in vitro model of human development and disease," *Nat. Cell Biol.*, vol. 18, no. 3, pp. 246–254, 2016.

[42]   Y. Fang and R. M. Eglen, "Three-Dimensional Cell Cultures in Drug Discovery and Development," *SLAS Discov.*, vol. 22, no. 5, pp. 456–472, 2017.

[43]   C. L. Morton and P. J. Houghton, "Establishment of human tumor xenografts in immunodeficient mice," *Nat. Protoc.*, vol. 2, no. 2, pp. 247–250, 2007.

[44]   M. Astolfi *et al.*, "Micro-dissected tumor tissues on chip: an ex vivo method for drug testing and personalized therapy," *Lab Chip*, vol. 16, pp. 312–325, 2016.

[45]   N. Rousset, F. Monet, and T. Gervais, "Simulation-assisted design of microfluidic sample traps for optimal trapping and culture of non-adherent single cells, tissues, and spheroids," *Sci. Rep.*, vol. 7, p. 245, 2017.

[46]   J. A. Joyce and J. W. Pollard, "Microenvironmental regulation of metastasis," *Nat. Rev. Cancer*, vol. 9, no. 4, pp. 239–252, 2009.

[47]   S. M. Ansell and R. H. Vonderheide, "Cellular Composition of the Tumor Microenvironment," *Am. Soc. Clin. Oncol. Educ. B.*, vol. 33, pp. e91–e97, 2013.

[48]   M. Greaves and C. C. Maley, "Clonal evolution in cancer," *Nature*, vol. 481, no. 7381, pp. 306–313, 2012.

[49]   A. Goldman, M. Kohandel, and J. Clairambault, "Integrating Biological and Mathematical Models to Explain and Overcome Drug Resistance in Cancer. Part 1: Biological Facts and Studies in Drug Resistance," *Curr. Stem Cell Reports*, vol. 3, no. 3, pp. 253–259, 2017.

[50]   M. Gerlinger and C. Swanton, "How Darwinian models inform therapeutic failure initiated by clonal heterogeneity in cancer medicine," *Br. J. Cancer*, vol. 103, no. 8, pp. 1139–1143, 2010.

[51]   D. R. Caswell and C. Swanton, "The role of tumour heterogeneity and clonal cooperativity in metastasis, immune evasion and clinical outcome," *BMC Med.*, vol. 15, no. 133, pp. 1–9, 2017.

[52]   A. S. Cleary, T. L. Leonard, S. A. Gestl, and E. J. Gunther, "Tumour cell heterogeneity maintained by cooperating subclones in Wnt-driven mammary cancers," *Nature*, vol. 508, no. 7494, pp. 113–117, 2014.

[53]   M. Zhang *et al.*, "Intratumoral Heterogeneity in a Trp53-Null Mouse Model of Human Breast Cancer," *Cancer Discov.*, vol. 5, no. 5, pp. 520–533, 2015.

[54]   M. Zanoni *et al.*, "3D tumor spheroid models for in vitro therapeutic screening: a systematic approach to enhance the biological relevance of data obtained," *Sci. Rep.*, vol. 6, p. 19103, 2016.

[55]   J. P. Celli *et al.*, "An imaging-based platform for high-content, quantitative evaluation of therapeutic response in 3D tumour models," *Sci. Rep.*, vol. 4, pp. 1–10, 2014.

[56]   M. Vinci *et al.*, "Advances in establishment and analysis of three-dimensional tumor spheroid-based functional assays for target validation and drug evaluation," *BMC Biol.*, vol. 10, no. 1, p. 29, 2012.

[57]   R.-Z. Lin and H.-Y. Chang, "Recent advances in three-dimensional multicellular spheroid culture for biomedical research," *Biotechnol. J.*, vol. 3, no. 9–10, pp. 1172–1184, 2008.

[58]   G. H. Lee, J. S. Lee, X. Wang, S. H. Lee, and S. Hoon Lee, "Bottom-Up Engineering of Well-Defined 3D Microtissues Using Microplatforms and Biomedical Applications," *Adv.*

Healthc. Mater., vol. 5, no. 1, pp. 56–74, 2016.

[59]   R. Vadivelu, H. Kamble, M. Shiddiky, and N.-T. Nguyen, "Microfluidic Technology for the Generation of Cell Spheroids and Their Applications," *Micromachines*, vol. 8, no. 4, p. 94, 2017.

[60]   A. Folch, *Introduction to BioMEMS*. Boca Raton, USA: Taylor & Francis, 2013.

[61]   G. V. Casquillas and T. Houssin, "PDMS: A review." [Online]. Available: https://www.elveflow.com/microfluidic-tutorials/microfluidic-reviews-and-tutorials/the-poly-di-methyl-siloxane-pdms-and-microfluidics/. [Accessed: 17-Aug-2018].

[62]   S. Nath and G. R. Devi, "Three-dimensional culture systems in cancer research: Focus on tumor spheroid model," *Pharmacol. Ther.*, vol. 163, pp. 94–108, 2016.

[63]   D. Gao *et al.*, "Recent developments in microfluidic devices for in vitro cell culture for cell-biology research," *TrAC Trends Anal. Chem.*, vol. 35, pp. 150–164, 2012.

[64]   X. Cui, Y. Hartanto, and H. Zhang, "Advances in multicellular spheroids formation," *J. R. Soc. Interface*, vol. 14, no. 127, p. 20160877, 2017.

[65]   V. van Duinen, S. J. Trietsch, J. Joore, P. Vulto, and T. Hankemeier, "Microfluidic 3D cell culture: From tools to tissue models," *Curr. Opin. Biotechnol.*, vol. 35, pp. 118–126, 2015.

[66]   N. Kashaninejad *et al.*, "Organ-Tumor-on-a-Chip for Chemosensitivity Assay: A Critical Review," *Micromachines*, vol. 7, p. 130, 2016.

[67]   K. Moshksayan, N. Kashaninejad, and M. Saidi, "Inventions and Innovations in Preclinical Platforms for Cancer Research," *Inventions*, vol. 3, no. 3, p. 43, 2018.

[68]   L. Y. Wu, D. Di Carlo, and L. P. Lee, "Microfluidic self-assembly of tumor spheroids for anticancer drug discovery.," *Biomed. Microdevices*, vol. 10, no. 2, pp. 197–202, 2008.

[69]   W. Liu, J.-C. Wang, and J. Wang, "Controllable organization and high throughput production of recoverable 3D tumors using pneumatic microfluidics," *Lab Chip*, vol. 15, no. 4, pp. 1195–1204, 2015.

[70]   J. Ruppen *et al.*, "Towards personalized medicine: chemosensitivity assays of patient lung cancer cell spheroids in a perfused microfluidic platform," *Lab Chip*, vol. 15, no. 14, pp. 3076–3085, 2015.

[71] S. Agastin, U.-B. T. Giang, Y. Geng, L. A. Delouise, and M. R. King, "Continuously perfused microbubble array for 3D tumor spheroid model.," *Biomicrofluidics*, vol. 5, no. 2, p. 24110, 2011.

[72] B. Patra, Y. H. Chen, C. C. Peng, S. C. Lin, C.-H. Lee, and Y. C. Tung, "A microfluidic device for uniform-sized cell spheroids formation, culture, harvesting and flow cytometry analysis," *Biomicrofluidics*, vol. 7, no. 5, pp. 054114-1-054114-11, 2013.

[73] K. Kwapiszewska, A. Michalczuk, M. Rybka, R. Kwapiszewski, and Z. Brzózka, "A microfluidic-based platform for tumour spheroid culture, monitoring and drug screening.," *Lab Chip*, vol. 14, pp. 2096–104, 2014.

[74] A. R.Brunet, F. Labelle, P. Wong, and T. Gervais, "Reconfigurable Microfluidic Magnetic Valve Arrays: Towards a Radiotherapy-Compatible Spheroid Culture Platform for the Combinatorial Screening of Cancer Therapies," *Sensors*, vol. 17, p. 2271, 2017.

[75] A. St-Georges-Robillard *et al.*, "Chemosensitivity analysis of co-culture tumor spheroids on chip using hyperspectral fluorescence imaging," in *Proceedings of MicroTAS 2017*, 2017, pp. 545–546.

[76] O. Frey, P. M. Misun, D. A. Fluri, J. G. Hengstler, and A. Hierlemann, "Reconfigurable microfluidic hanging drop network for multi-tissue interaction and analysis," *Nat. Commun.*, vol. 5, p. 4250, 2014.

[77] H. F. Chan, Y. Zhang, Y.-P. Ho, Y.-L. Chiu, Y. Jung, and K. W. Leong, "Rapid formation of multicellular spheroids in double-emulsion droplets with controllable microenvironment," *Sci. Rep.*, vol. 3, no. 1, p. 3462, 2013.

[78] M. Marimuthu *et al.*, "Multi-size spheroid formation using microfluidic funnels," *Lab Chip*, vol. 18, pp. 304–314, 2018.

[79] S.-Y. Teh, R. Lin, L.-H. Hung, and A. P. Lee, "Droplet microfluidics," *Lab Chip*, vol. 8, no. 2, p. 198, 2008.

[80] C. Kim, J. H. Bang, Y. E. Kim, S. H. Lee, and J. Y. Kang, "On-chip anticancer drug test of regular tumor spheroids formed in microwells by a distributive microchannel network.," *Lab Chip*, vol. 12, no. 20, pp. 4135–42, 2012.

[81] L. Yu, C. Ni, S. M. Grist, C. Bayly, and K. C. Cheung, "Alginate core-shell beads for simplified three-dimensional tumor spheroid culture and drug screening," *Biomed. Microdevices*, vol. 17, no. 2, p. 33, 2015.

[82] G. Hu and D. Li, "Three-dimensional modeling of transport of nutrients for multicellular tumor spheroid culture in a microchannel.," *Biomed. Microdevices*, vol. 9, no. 3, pp. 315–23, 2007.

[83] V. E. Santo, S. P. Rebelo, M. F. Estrada, P. M. Alves, E. Boghaert, and C. Brito, "Drug screening in 3D in vitro tumor models: overcoming current pitfalls of efficacy read-outs," *Biotechnol. J.*, vol. 12, no. 1, 2017.

[84] T. R. Jones *et al.*, "CellProfiler Analyst: data exploration and analysis software for complex image-based screens," *BMC Bioinformatics*, vol. 9, no. 1, p. 482, 2008.

[85] C. M. Garvey *et al.*, "A high-content image-based method for quantitatively studying context-dependent cell population dynamics," *Sci. Rep.*, vol. 6, p. 29752, 2016.

[86] J. C. Caicedo *et al.*, "Data-analysis strategies for image-based cell profiling," *Nat. Methods*, vol. 14, no. 9, pp. 849–863, 2017.

[87] V. Härmä *et al.*, "Quantification of Dynamic Morphological Drug Responses in 3D Organotypic Cell Cultures by Automated Image Analysis," *PLoS One*, vol. 9, no. 5, p. e96426, 2014.

[88] R. Kilani *et al.*, "Selective cytotoxicity of gemcitabine in bladder cancer cell lines," *Anticancer. Drugs*, vol. 13, no. 6, pp. 557–566, 2002.

[89] I. Ahonen, M. Åkerfelt, M. Toriseva, E. Oswald, J. Schüler, and M. Nees, "A high-content image analysis approach for quantitative measurements of chemosensitivity in patient-derived tumor microtissues," *Sci. Rep.*, vol. 7, p. 6600, 2017.

[90] G. Mehta, A. Y. Hsiao, M. Ingram, G. D. Luker, and S. Takayama, "Opportunities and challenges for use of tumor spheroids as models to test drug delivery and efficacy," *J. Control. Release*, vol. 164, no. 2, pp. 192–204, 2012.

[91] E. Beem and M. S. Segal, "Evaluation of stability and sensitivity of cell fluorescent labels when used for cell migration," *J. Fluoresc.*, vol. 23, no. 5, pp. 975–987, 2013.

[92]   Y. Go *et al.*, "Inhibition of in vivo tumorigenicity and invasiveness of a human glioblastoma cell line transfected with antisense uPAR vectors," *Clin. Exp. Metastasis*, vol. 15, no. 4, pp. 440–446, 1997.

[93]   R. Y. Tsien, "The Green Fluorescent Protein," *Annu. Rev. Biochem.*, vol. 67, no. 1, pp. 509–544, 1998.

[94]   N. C. Shaner, P. A. Steinbach, and R. Y. Tsien, "A guide to choosing fluorescent proteins.," *Nat. Methods*, vol. 2, no. 12, pp. 905–909, 2005.

[95]   A. Y. Hsiao *et al.*, "Microfluidic system for formation of PC-3 prostate cancer co-culture spheroids," *Biomaterials*, vol. 30, no. 16, pp. 3020–3027, 2009.

[96]   A. Adan, G. Alizada, Y. Kiraz, Y. Baran, and A. Nalbant, "Flow cytometry: basic principles and applications," *Crit. Rev. Biotechnol.*, vol. 37, no. 2, pp. 163–176, 2017.

[97]   D. G. Buschke, A. Vivekanandan, J. M. Squirrell, C. T. Rueden, K. W. Eliceiri, and B. M. Ogle, "Large particle multiphoton flow cytometry to purify intact embryoid bodies exhibiting enhanced potential for cardiomyocyte differentiation," *Integr. Biol.*, vol. 5, no. 7, p. 993, 2013.

[98]   D. A. Watson, D. F. Gaskill, L. O. Brown, S. K. Doorn, and J. P. Nolan, "Spectral measurements of large particles by flow cytometry," *Cytom. Part A*, vol. 75A, no. 5, pp. 460–464, 2009.

[99]   D. Huh, W. Gu, Y. Kamotani, J. B. Grotberg, and S. Takayama, "Microfluidics for flow cytometric analysis of cells and particles," *Physiol. Meas.*, vol. 26, no. 3, pp. R73–R98, 2005.

[100]   Y. Zhao *et al.*, "Optofluidic imaging: now and beyond.," *Lab Chip*, vol. 13, no. 1, pp. 17–24, 2013.

[101]   S. Stavrakis, G. Holzner, J. Choo, and A. DeMello, "High-throughput microfluidic imaging flow cytometry," *Curr. Opin. Biotechnol.*, vol. 55, pp. 36–43, 2019.

[102]   J. P. Robinson, "Comparative Overview of Flow and Image Cytometry," in *Current Protocols in Cytometry*, Hoboken, NJ, USA: John Wiley & Sons, Inc., 2005.

[103]   S. Kessel *et al.*, "High-Throughput 3D Tumor Spheroid Screening Method for Cancer Drug

Discovery Using Celigo Image Cytometry," *SLAS Technol. Transl. Life Sci. Innov.*, vol. 22, no. 4, pp. 454–465, 2016.

[104] B. Patra, C.-C. Peng, W.-H. Liao, C.-H. Lee, and Y.-C. Tung, "Drug testing and flow cytometry analysis on a large number of uniform sized tumor spheroids using a microfluidic device," *Sci. Rep.*, vol. 6, no. 1, p. 21061, 2016.

[105] D. P. Ivanov *et al.*, "In vitro co-culture model of medulloblastoma and human neural stem cells for drug delivery assessment," *J. Biotechnol.*, vol. 205, pp. 3–13, 2015.

[106] D. P. Ivanov and A. M. Grabowska, "Spheroid arrays for high-throughput single-cell analysis of spatial patterns and biomarker expression in 3D," *Sci. Rep.*, vol. 7, no. 1, p. 41160, 2017.

[107] C. Fang, I. Avis, D. Salomon, and F. Cuttitta, "Novel phenotypic fluorescent three-dimensional platforms for high-throughput drug screening and personalized chemotherapy," *J. Cancer*, vol. 4, no. 5, pp. 401–415, 2013.

[108] N. Dorst, M. Oberringer, U. Grasser, T. Pohlemann, and W. Metzger, "Analysis of cellular composition of co-culture spheroids," *Ann. Anat.*, vol. 196, no. 5, pp. 303–311, 2014.

[109] L.-B. Weiswald, J.-M. Guinebretière, S. Richon, D. Bellet, B. Saubaméa, and V. Dangles-Marie, "In situ protein expression in tumour spheres: development of an immunostaining protocol for confocal microscopy," *BMC Cancer*, vol. 10, no. 1, p. 106, 2010.

[110] I. Smyrek and E. H. K. H. K. Stelzer, "Quantitative three-dimensional evaluation of immunofluorescence staining for large whole mount spheroids with light sheet microscopy," *Biomed. Opt. Express*, vol. 8, no. 2, p. 484, 2017.

[111] T.-M. Achilli, S. McCalla, A. Tripathi, and J. R. Morgan, "Quantification of the Kinetics and Extent of Self-Sorting in Three Dimensional Spheroids," *Tissue Eng. Part C Methods*, vol. 18, no. 4, pp. 302–309, 2012.

[112] J. C. Waters, "Accuracy and precision in quantitative fluorescence microscopy.," *J. Cell Biol.*, vol. 185, no. 7, pp. 1135–48, 2009.

[113] K. R. Spring and M. W. Davidson, "Depth of field and depth of focus." [Online]. Available: https://www.microscopyu.com/microscopy-basics/depth-of-field-and-depth-of-focus.

[Accessed: 03-Sep-2018].

[114] V. Ljosa and A. E. Carpenter, "Introduction to the Quantitative Analysis of Two-Dimensional Fluorescence Microscopy Images for Cell-Based Screening," *PLoS Comput. Biol.*, vol. 5, no. 12, p. e1000603, 2009.

[115] S.-H. Lu and H. Hua, "Imaging properties of extended depth of field microscopy through single-shot focus scanning," *Opt. Express*, vol. 23, no. 8, p. 10714, 2015.

[116] C. Ortiz de Solórzano, J. Uranga, A. Rodríguez-Pena, and D. Gahigiro, "Miniaturized microscope for high throughput screening of tumor spheroids in microfluidic devices," *Imaging, Manip. Anal. Biomol. Cells, Tissues XVI*, p. 9, 2018.

[117] A. Ozcan and E. McLeod, "Lensless Imaging and Sensing," *Annu. Rev. Biomed. Eng.*, vol. 18, pp. 77–102, 2016.

[118] L. V. Wang and H. Wu, *Biomedical Optics*. Hoboken: John Wiley & Sons, 2007.

[119] M. J. Stoddart, *Mammalian Cell Viability*. New York: Springer, 2011.

[120] M. Wartenberg and H. Acker, "Quantitative recording of vitality patterns in living multicellular spheroids by confocal microscopy.," *Micron*, vol. 26, no. 5, pp. 395–404, 1995.

[121] T. Das *et al.*, "Empirical chemosensitivity testing in a spheroid model of ovarian cancer using a microfluidics-based multiplex platform," *Biomicrofluidics*, vol. 7, no. 1, pp. 011805-1-011805-15, 2013.

[122] J. Kang, D. W. Lee, H. J. Hwang, S.-E. Yeon, M.-Y. Lee, and H.-J. Kuh, "Mini-pillar array for hydrogel-supported 3D culture and high-content histologic analysis of human tumor spheroids," *Lab Chip*, vol. 16, pp. 2265–2276, 2016.

[123] P. Indovina, M. Collini, G. Chirico, and M. T. Santini, "Three-dimensional cell organization leads to almost immediate HRE activity as demonstrated by molecular imaging of MG-63 spheroids using two-photon excitation microscopy," *FEBS Lett.*, vol. 581, no. 4, pp. 719–726, 2007.

[124] E. Leary, C. Rhee, B. T. Wilks, and J. R. Morgan, "Quantitative Live-Cell Confocal Imaging of 3D Spheroids in a High-Throughput Format," *SLAS Technol.*, vol. 23, no. 3, pp. 231–242, 2018.

[125] S.-B. Huang, S.-S. Wang, C.-H. Hsieh, Y. C. Lin, C.-S. Lai, and M.-H. Wu, "An integrated microfluidic cell culture system for high-throughput perfusion three-dimensional cell culture-based assays: effect of cell culture model on the results of chemosensitivity assays," *Lab Chip*, vol. 13, pp. 1133–43, 2013.

[126] S. Mohapatra, S. Nandi, R. Chowdhury, G. Das, S. Ghosh, and K. Bhattacharyya, "Spectral mapping of 3D multi-cellular tumor spheroids: Time-resolved confocal microscopy," *Phys. Chem. Chem. Phys.*, vol. 18, no. 27, pp. 18381–18390, 2016.

[127] M. Barbier *et al.*, "Ellipsoid Segmentation Model for Analyzing Light-Attenuated 3D Confocal Image Stacks of Fluorescent Multi-Cellular Spheroids," *PLoS One*, vol. 11, no. 6, p. e0156942, 2016.

[128] K. Olofsson *et al.*, "Acoustic formation of multicellular tumor spheroids enabling on-chip functional and structural imaging," *Lab Chip*, vol. 18, no. 16, pp. 2466–2476, 2018.

[129] C. Boudoux, *Fundamentals of Biomdecial Optics*. Montréal: Pollux Editions, 2017.

[130] A. H. Voie, D. H. Burns, and F. A. Spelman, "Orthogonal-plane fluorescence optical sectioning: Three-dimensional imaging of macroscopic biological specimens," *J. Microsc.*, vol. 170, no. 3, pp. 229–236, 1993.

[131] J. Huisken, J. Swoger, F. Del Bene, J. Wittbrodt, and E. H. K. Stelzer, "Optical Sectioning Deep Inside Live Embryos by Selective Plane Illumination Microscopy," *Science (80-.).*, vol. 305, no. 5686, pp. 1007–1009, 2004.

[132] F. Pampaloni, N. Ansari, and E. H. K. Stelzer, "High-resolution deep imaging of live cellular spheroids with light-sheet-based fluorescence microscopy," *Cell Tissue Res.*, vol. 352, no. 1, pp. 161–177, 2013.

[133] P. J. Verveer, J. Swoger, F. Pampaloni, K. Greger, M. Marcello, and E. H. K. Stelzer, "High-resolution three-dimensional imaging of large specimens with light sheet–based microscopy," *Nat. Methods*, vol. 4, no. 4, pp. 311–313, 2007.

[134] C. Lorenzo *et al.*, "Live cell division dynamics monitoring in 3D large spheroid tumor models using light sheet microscopy," *Cell Div.*, vol. 6, no. 1, p. 22, 2011.

[135] B. Patra *et al.*, "Migration and vascular lumen formation of endothelial cells in cancer cell

spheroids of various sizes," *Biomicrofluidics*, vol. 8, no. 5, p. 052109, 2014.

[136] A. F. H. Goetz, "Three decades of hyperspectral remote sensing of the Earth: A personal view," *Remote Sens. Environ.*, vol. 113, no. SUPPL. 1, pp. S5–S16, 2009.

[137] J. Qin, M. Kim, K. Chao, D. Chan, S. Delwiche, and B.-K. Cho, "Line-Scan Hyperspectral Imaging Techniques for Food Safety and Quality Applications," *Appl. Sci.*, vol. 7, no. 2, p. 125, 2017.

[138] J. M. Lerner, N. Gat, and E. Wachman, "Approaches to spectral imaging hardware," in *Current protocols in cytometry, Unit 12.20*, 2010.

[139] G. Lu and B. Fei, "Medical hyperspectral imaging: a review," *J. Biomed. Opt.*, vol. 19, no. 1, p. 10901, 2014.

[140] Y. W. Wang, N. P. Reder, S. Kang, A. K. Glaser, and J. T. C. Liu, "Multiplexed Optical Imaging of Tumor-Directed Nanoparticles: A Review of Imaging Systems and Approaches," *Nanotheranostics*, vol. 1, no. 4, pp. 369–388, 2017.

[141] J. Pichette *et al.*, "Intraoperative video-rate hemodynamic response assessment in human cortex using snapshot hyperspectral optical imaging," *Neurophotonics*, vol. 3, no. 4, p. 045003, 2016.

[142] T. E. Renkoski, K. D. Hatch, and U. Utzinger, "Wide-field spectral imaging of human ovary autofluorescence and oncologic diagnosis via previously collected probe data," *J. Biomed. Opt.*, vol. 17, no. 3, p. 036003, 2012.

[143] J. J. Bravo, J. D. Olson, S. C. Davis, D. W. Roberts, K. D. Paulsen, and S. C. Kanick, "Hyperspectral data processing improves PpIX contrast during fluorescence guided surgery of human brain tumors," *Sci. Rep.*, vol. 7, p. 9455, 2017.

[144] M. Huang, X. Wan, M. Zhang, and Q. Zhu, "Detection of insect-damaged vegetable soybeans using hyperspectral transmittance image," *J. Food Eng.*, vol. 116, no. 1, pp. 45–49, 2013.

[145] Y. Guan, "Pathological leucocyte segmentation algorithm based on hyperspectral imaging technique," *Opt. Eng.*, vol. 51, no. 5, p. 053202, 2012.

[146] P. A. Bautista and Y. Yagi, "Digital simulation of staining in histopathology multispectral

images: enhancement and linear transformation of spectral transmittance," *J. Biomed. Opt.*, vol. 17, no. 5, p. 056013, 2012.

[147] P. V. Jena, Y. Shamay, J. Shah, D. Roxbury, N. Paknejad, and D. A. Heller, "Photoluminescent carbon nanotubes interrogate the permeability of multicellular tumor spheroids," *Carbon N. Y.*, vol. 97, pp. 99–109, 2016.

[148] G. Di Caprio, D. Schaak, and E. Schonbrun, "Hyperspectral fluorescence microfluidic (HFM) microscopy.," *Biomed. Opt. Express*, vol. 4, no. 8, pp. 1486–93, 2013.

[149] A. P. Horton *et al.*, "Quantitative immunophenotyping of circulating tumor cells in blood using microfluidic screening chip integrated with hyperspectral microscope," in *TRANSDUCERS 2009 - 2009 International Solid-State Sensors, Actuators and Microsystems Conference*, 2009, pp. 77–80.

[150] W. Jahr, B. Schmid, C. Schmied, F. O. Fahrbach, and J. Huisken, "Hyperspectral light sheet microscopy," *Nat. Commun.*, vol. 6, p. 7990, 2015.

[151] R. B. Saager, D. J. Cuccia, S. Saggese, K. M. Kelly, and A. J. Durkin, "Quantitative fluorescence imaging of protoporphyrin IX through determination of tissue optical properties in the spatial frequency domain," *J. Biomed. Opt.*, vol. 16, no. 12, p. 126013, 2011.

[152] A. Kim, M. Khurana, Y. Moriyama, and B. C. Wilson, "Quantification of in vivo fluorescence decoupled from the effects of tissue optical properties using fiber-optic spectroscopy measurements," *J. Biomed. Opt.*, vol. 15, no. 6, p. 067006, 2010.

[153] B. W. Pogue and M. S. Patterson, "Review of tissue simulating phantoms for optical spectroscopy, imaging and dosimetry," *J. Biomed. Opt.*, vol. 11, no. 4, p. 041102, 2006.

[154] R. S. Bradley and M. S. Thorniley, "A review of attenuation correction techniques for tissue fluorescence.," *J. R. Soc. Interface*, vol. 3, no. 6, pp. 1–13, 2006.

[155] P. A. Valdés, F. Leblond, A. Kim, B. C. Wilson, K. D. Paulsen, and D. W. Roberts, "A spectrally constrained dual-band normalization technique for protoporphyrin IX quantification in fluorescence-guided surgery," *Opt. Lett.*, vol. 37, no. 11, pp. 1817–9, 2012.

[156] P. Hargrave, P. W. Nicholson, D. T. Delpy, and M. Firbank, "Optical properties of

multicellular tumour spheroids.," *Phys. Med. Biol.*, vol. 41, no. 6, pp. 1067–72, 1996.

[157] V. P. Wallace, A. K. Dunn, M. L. Coleno, and B. J. Tromberg, "Two-Photon Microscopy in Highly Scattering Tissue," in *Methods in Cellular Imaging,* New York, USA: Springer, 2001, pp. 180–199.

[158] S. T. Flock, S. L. Jacques, B. C. Wilson, W. M. Star, and M. J. van Gemert, "Optical properties of Intralipid: a phantom medium for light propagation studies.," *Lasers Surg. Med.*, vol. 12, no. 5, pp. 510–9, 1992.

[159] A. St-Georges-Robillard *et al.*, "Fluorescence hyperspectral imaging for live monitoring of multiple spheroids in microfluidic chips," *Analyst*, vol. 143, no. 16, pp. 3829–3840, 2018.

[160] A. Junaid, A. Mashaghi, T. Hankemeier, and P. Vulto, "An end-user perspective on Organ-on-a-Chip: Assays and usability aspects," *Curr. Opin. Biomed. Eng.*, vol. 1, pp. 15–22, 2017.

[161] K. Soderberg and R. J.-C. Hennet, "Uncertainty and Trend Analysis-Radium in Ground Water and Drinking Water," *Groundw. Monit. Remediat.*, vol. 27, no. 4, pp. 122–129, 2007.

[162] S. Jeong, J. Lee, Y. Shin, S. Chung, and H. Kuh, "Co-Culture of Tumor Spheroids and Fibroblasts in a Collagen Matrix-Incorporated Microfluidic Chip Mimics Reciprocal Activation in Solid Tumor Microenvironment," *PLoS One*, vol. 11, no. 7, p. e0159013, 2016.

[163] C. Y. Chan *et al.*, "Accelerating drug discovery via organs-on-chips," *Lab Chip*, vol. 13, no. 24, p. 4697, 2013.

[164] H. Hardelauf *et al.*, "Microarrays for the scalable production of metabolically relevant tumour spheroids: a tool for modulating chemosensitivity traits," *Lab Chip*, vol. 11, no. 3, pp. 419–428, 2011.

[165] L. E. Smith, R. O. D. Smallwood, and S. Macneil, "A Comparison of Imaging Methodologies for 3D Tissue Engineering," *Microsc. Reasearch Tech.*, vol. 73, pp. 1123–1133, 2010.

[166] N. J. Martinez, S. A. Titus, A. K. Wagner, and A. Simeonov, "High-throughput fluorescence imaging approaches for drug discovery using in vitro and in vivo three-dimensional models," *Expert Opin. Drug Discov.*, vol. 0441, no. October, pp. 1–15, 2015.

[167] J. P. Angelo, M. van de Giessen, and S. Gioux, "Real-time endoscopic optical properties

imaging," *Biomed. Opt. Express*, vol. 8, no. 11, pp. 5113–5126, 2017.

[168] M. Jermyn *et al.*, "Improved sensitivity to fluorescence for cancer detection in wide-field image-guided neurosurgery," *Biomed. Opt. Express*, vol. 6, no. 12, p. 5063, 2015.

[169] J. Chu *et al.*, "Non-invasive intravital imaging of cellular differentiation with a bright red-excitable fluorescent protein," *Nat. Methods*, vol. 11, no. 5, pp. 572–578, 2014.

[170] F. V. Subach, G. H. Patterson, S. Manley, J. M. Gillette, J. Lippincott-Schwartz, and V. V. Verkhusha, "Photoactivatable mCherry for high-resolution two-color fluorescence microscopy," *Nat. Methods*, vol. 6, no. 2, pp. 153–159, 2009.

[171] K. Chung, Y. Kim, J. S. Kanodia, E. Gong, S. Y. Shvartsman, and H. Lu, "A microfluidic array for large-scale ordering and orientation of embryos.," *Nat. Methods*, vol. 8, no. 2, pp. 171–6, 2011.

[172] A. St-Georges-Robillard *et al.*, "Long term fluorescence hyperspectral imaging of on-chip treated co-culture tumour spheroids to follow clonal evolution," *submitted to Integrative Biology*, 2018.

[173] P. M. Misun, A. K. Birchler, M. Lang, A. Hierlemann, and O. Frey, "Fabrication and Operation of Microfluidic Hanging-Drop Networks," 2018, pp. 183–202.

[174] M. Boutros, F. Heigwer, and C. Laufer, "Microscopy-Based High-Content Screening," *Cell*, vol. 163, no. 6, pp. 1314–1325, 2015.

[175] E. A. Susaki *et al.*, "Whole-brain imaging with single-cell resolution using chemical cocktails and computational analysis," *Cell*, vol. 157, no. 3, pp. 726–739, 2014.

[176] S. M. Grist, S. S. Nasseri, T. Poon, C. Roskelley, and K. C. Cheung, "On-chip clearing of arrays of 3-D cell cultures and micro-tissues," *Biomicrofluidics*, vol. 10, no. 4, pp. 1–15, 2016.

[177] S. P. Cavnar, E. Salomonsson, K. E. Luker, G. D. Luker, and S. Takayama, "Transfer, Imaging, and Analysis Plate for Facile Handling of 384 Hanging Drop 3D Tissue Spheroids," *J. Lab. Autom.*, vol. 19, no. 2, pp. 208–14, 2014.

[178] B. Patra *et al.*, "Are 3D spheroids always more resistant to chemotherapy than 2D cultures? A chip-based survey using ovarian cancer cell lines," in *Proceedings of MicroTAS 2016*,

2016, pp. 1555–1556.

[179] I. C. McLean, L. A. Schwerdtfeger, S. A. Tobet, and C. S. Henry, "Powering ex vivo tissue models in microfluidic systems," *Lab Chip*, vol. 18, no. 10, pp. 1399–1410, 2018.

[180] M. Fortin, A.-M. Steff, and P. Hugo, "High-Throughput Technology: Green Fluorescent Protein to Monitor Cell Death," in *Chemosensitivity*, vol. 110, New Jersey: Humana Press, 2005, pp. 121–138.

[181] A.-M. Steff, M. Fortin, C. Arguin, and P. Hugo, "Detection of a decrease in green fluorescent protein fluorescence for the monitoring of cell death: An assay amenable to high-throughput screening technologies," *Cytometry*, vol. 45, no. 4, pp. 237–243, 2001.

[182] T. C. Chang, A. M. Mikheev, W. Huynh, R. J. Monnat, R. C. Rostomily, and A. Folch, "Parallel microfluidic chemosensitivity testing on individual slice cultures," *Lab Chip*, vol. 14, no. 23, pp. 4540–4551, 2014.

[183] P. M. van Midwoud, M. T. Merema, E. Verpoorte, and G. M. M. Groothuis, "A microfluidic approach for in vitro assessment of interorgan interactions in drug metabolism using intestinal and liver slices.," *Lab Chip*, vol. 10, no. 20, pp. 2778–86, 2010.

[184] D. J. Collins, A. Neild, A. deMello, A.-Q. Q. Liu, and Y. Ai, "The Poisson distribution and beyond: Methods for microfluidic droplet production and single cell encapsulation," *Lab Chip*, vol. 15, no. 17, pp. 3439–3459, 2015.

[185] K. Y. Lee and D. J. Mooney, "Alginate: properties and biomedical applications.," *Prog. Polym. Sci.*, vol. 37, no. 1, pp. 106–126, 2012.

[186] V. Trivedi, A. Doshi, G. K. Kurup, E. Ereifej, P. J. Vandevord, and A. S. Basu, "A modular approach for the generation, storage, mixing, and detection of droplet libraries for high throughput screening.," *Lab Chip*, vol. 10, no. 18, pp. 2433–42, 2010.

[187] W. Chen *et al.*, "Microfluidic one-step synthesis of alginate microspheres immobilized with antibodies," *J. R. Soc. Interface*, vol. 10, no. 88, pp. 20130566–20130566, 2013.

[188] D. H. Lee, W. Lee, E. Um, and J. K. Park, "Microbridge structures for uniform interval control of flowing droplets in microfluidic networks," *Biomicrofluidics*, vol. 5, p. 034117, 2011.

[189] J. Lan, J. Chen, N. Li, X. Ji, M. Yu, and Z. He, "Microfluidic generation of magnetic-fluorescent Janus microparticles for biomolecular detection," *Talanta*, vol. 151, pp. 126–131, 2016.

[190] C. Kim *et al.*, "Generation of core-shell microcapsules with three-dimensional focusing device for efficient formation of cell spheroid," *Lab Chip*, vol. 11, no. 2, pp. 246–252, 2011.

[191] T. Lambert and K. Thorn, "Fluorescent proteins properties." [Online]. Available: http://www.fpvis.org/FP.html. [Accessed: 04-May-2018].

[192] H. B. Mann, "Nonparametric Tests Against Trend," *Econometrica*, vol. 13, no. 3, p. 245, 1945.

[193] M. G. Kendall, *Rank Correlation Methods*. London: Charles Griffin, 1975.

[194] J. Burkey, "A non-parametric monotonic trend test computing Mann-Kendall Tau, Tau-b, and Sens Slope written in Mathworks-MATLAB implemented using matrix rotations." King County, Department of Natural Resources and Parks, Science and Technical Services section, Seattle, Washington, USA, 2006.

[195] N. Otsu, "A Threshold Selection Method from Gray-Level Histograms," *IEEE Trans. Syst. Man. Cybern.*, vol. 9, no. 1, pp. 62–66, 1979.

APPENDIX A - ALGINATE BEADS MADE ON-CHIP AS OPTICAL PHANTOMS

This appendix presents the preliminary work on making spherical optical phantoms of spheroid-size. As described in section 2.4, the measured fluorescence intensity will depend on the geometry and optical properties of the imaged sample. Using a quantification algorithm considering the sample transmittance at specific wavelengths, these effects can be removed. The algorithm described by equation (4-1) was first validated for thin planar phantoms of optical properties similar to those of spheroids (see section 4.4.2). However, the optical phantoms used in this previous experiment do not replicate the geometry of a spheroid. All preliminary results shown in this appendix were obtained by Alexandre Chabot, a summer intern.

The microfluidic community has developed a range of techniques to form thousands of droplets of controlled size easily. Droplets are made using two immiscible phases, usually water-in-oil and gas-in-liquid. Droplets can be made using various techniques, including using a T-junction, flow-focusing, and co-flowing, as illustrated in Figure A-1. By varying the flow rate ratio between the oil and water, the droplet size can be controlled [79].
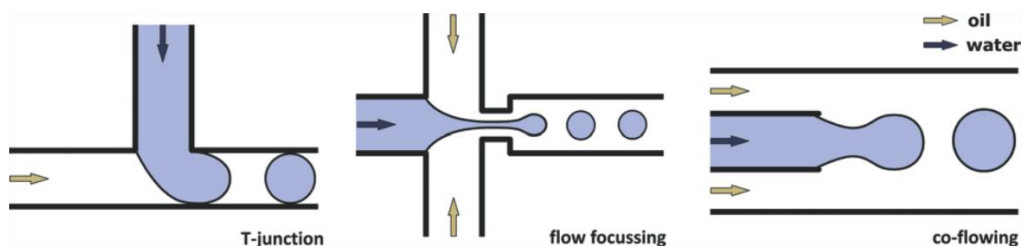

Figure A-1: Droplet generation methods. Reproduced from [184] with permission from The Royal Society of Chemistry.

By using a hydrophilic polymer and a cross-linker in the two immiscible phases, researchers have formed hydrogel beads on-chip using the different droplet formation methods. Sodium alginate and calcium chloride are commonly used to form alginate beads because of their biocompatibility with cell culture [185]. A few examples are summarized in Table A-1. In some examples, an alginate droplet is first made in an oil carrier using any of the three methods mentioned above, and the cross-linker is then added to the droplet using a second T-junction.

Table A-1: Alginate beads formation parameters

Droplet formation method	Polymer base	Oil carrier	Cross-linker	Bead diameter	Reference
Flow-focusing	Sodium alginate	Silicone oil	$BaCl_2$	0.15 to 1.5 mm	Trivedi *et al.* [186]
Co-flowing	Sodium alginate	Vegetable oil	$CaCl_2$	50 μm	Chen *et al.* [187]
T-junction	Sodium alginate	Oleic acid infused with $CaCl_2$	100 μm		Lee *et al.* [188]
Flow-focusing	Sodium alginate	Oleic acid infused with $CaCl_2$	100 μm		Lan *et al.* [189]
Flow focusing	Sodium alginate	Oleic acid infused with $CaCl_2$	130 μm		Kim *et al.* [190]

Preliminary results are shown in Figure A-2 and shows that water-in-oil droplets of approximately 300 μm in diameter can be made on-chip using the T-junction (Figure A-2A) and flow-focusing (Figure A-2B). Varying the water and oil flow rates lead to variations in droplet length, as the droplet width was limited by the channel width (Figure A-2E).

To form alginate beads on-chip, Alexandre used oleic acid as the lipid carrier and sodium alginate as the polymer. To form hydrogel beads in a single step, the oleic acid was infused with calcium using Kim *et al*. [190] explanations. Briefly, calcium chloride was dissolved in isobutanol using an ultrasonic bath. The oleic acid and the isobutanol mixture were then mixed at 50% and the isobutanol was evaporated overnight on a hotplate à 120 °C, resulting in calcium infused oleic acid. Figure A-2C shows alginate beads formed on-chip using the flow-focusing design (Figure A-2B) and harvested in a calcium infused oleic acid bath, to further complete the gelation process. Figure A-2D shows alginate and Intralipid®, also in a calcium infused oleic acid bath. In both cases, the bath was necessary to complete the gelation process, otherwise the beads fused together. More research will be necessary to optimize the bead size, as using alginate and Intralipid® yielded beads of very different sizes. Still, it is possible to form an alginate and Intralipid® hydrogel.
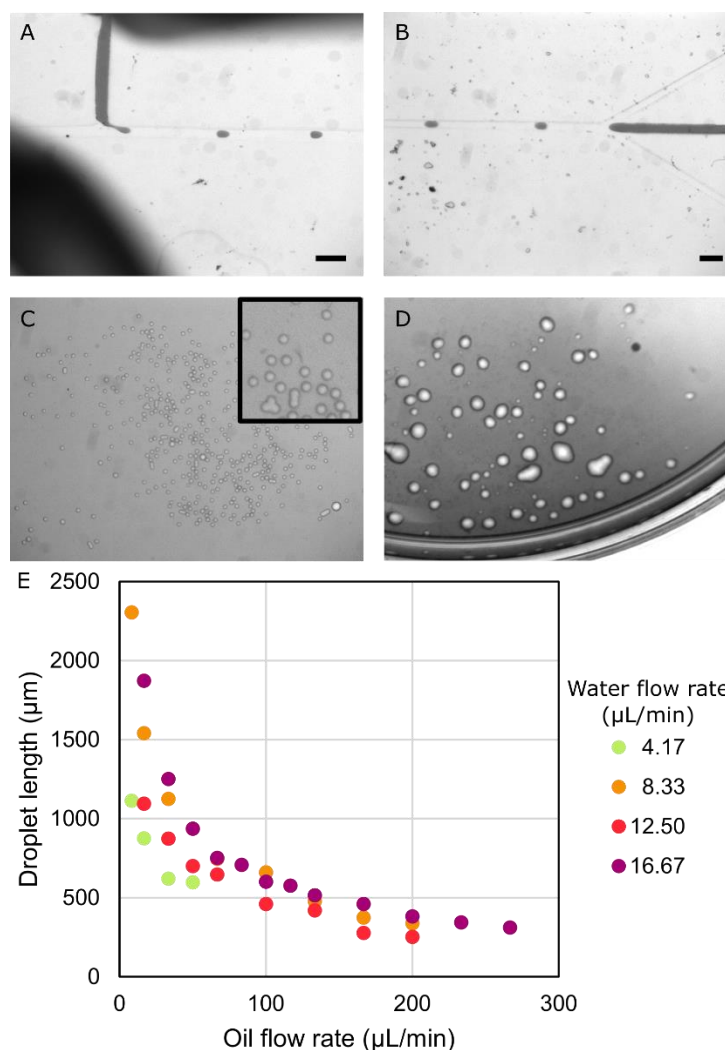
Figure A-2: Alginate and Intralipid® bead formation on-chip. A) Water-in-oil droplet formation using a T-junction. Scale bar = 1 mm. B) Water-in-oil droplet formation using flow-focusing. Scale bar = 1 mm. In A) and B), the water was coloured with food colouring to increase its visibility. C) Alginate beads in a calcium infused oleic acid bath. Inset shows an enlarged image of the beads. D) Intralipid® and alginate beads in a calcium infused oleic acid bath. E) Water-in-oil droplet length as a function of the oil and water flow rate. Results obtained using the flow-focusing design (B).

APPENDIX B - MONTE CARLO LIGHT PROPAGATION SIMULATIONS TO EVALUATE SPHEROID VOLUME SAMPLING

Ehsan Edjlali, post-doctoral researcher at the Laboratory for Radiological Optics, used a Monte Carlo light propagation simulation package first developed by Catherine St-Pierre [17] to simulate the trajectory of excitation and emission photons through a 300 μm-diameter spheroid. The goal was to estimate whether fluorescence photons are generated in the spheroid centre vicinity and if those photons are then detected by the HSI system camera, thereby evaluating the ability of the imaging system to sample the whole spheroid. A thin and long slab ($2 \times 2 \times 0.5$ cm^3) with the optical properties of air was first implemented. At the centre of the slab, a 300 μm-diameter sphere representing a spheroid was modelled and assumed to be homogeneous. Spheroid optical properties for eGFP fluorescence excitation (480 nm) and emission (515 nm) were estimated from Hargrave *et al*. [156] and Wallace *et al*. [157]. First, the wavelength dependency of the elastic scattering coefficient was modelled with a power-law approximation similar to that of Intralipid® [158] with an anisotropy factor (*g*) equal to 0.8. Since spheroids contain no strong absorber, the absorption in the sphere was hypothesized to only be due to eGFP fluorescence and the absorption coefficient set to 2.86 mm^{-1} (480 nm) and 0.348 mm^{-1} (515 nm) according to its absorption spectrum [191]. The quantum yield for eGFP was set at 0.6. For the simulations, a parallel light source was modelled with 2×10^6 excitation photons. Emitted fluorescence photons that crossed the detection plane were considered to be detected by the camera, resulting in 5 815 detected fluorescence photons.

Preliminary results are shown in Figure B-1. Positions in the spheroid where eGFP-fluorescence photons detected by the HSI system were generated are shown in Figure B-1A, indicating the HSI sampling volume. Figure B-1B shows that the density of fluorescence photons detected with the HSI system is similar at the spheroid centre compared to the outer layers. Finally, Figure B-1C-D shows the accumulative distribution of the generated fluorescence photons mapped on both *z* and *x* axes. The results show that the fluorescence emitted by cells located at the centre of a 300 μm-spheroid can be measured using the HSI system.
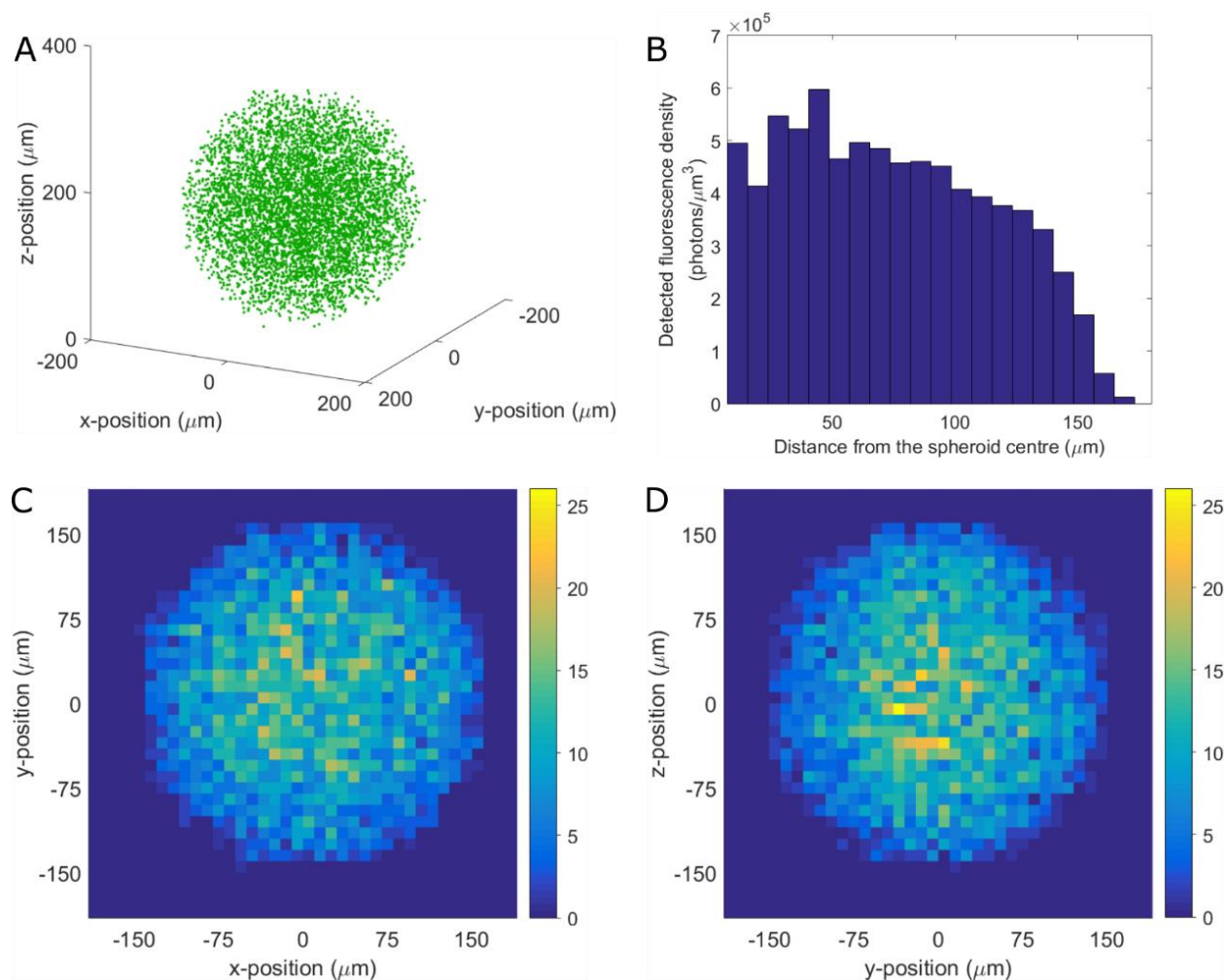
Figure B-1: Sampling volume in a spheroid in transillumination mode. A) Position in a 300 μm-diameter spheroid where eGFP photons detected by the HSI system's camera are generated. B) Detected photon density as a function of the distance from the spheroid centre. Top (C) and side (D) view of the accumulative distribution of the detected fluorescence photons in the spheroid.

APPENDIX C - STATISTICAL TEST MODIFICATION FOR MONOTONIC TREND DETECTION

During the course of my studies, I collaborated with Mohana Marimuthu, who did her post-doctoral fellowship in our laboratory, and developed an improved version of a statistical test, included in her work published in *Lab on a Chip* [78]. Her work focused on designing and validated a funnel-based microfluidic platform that could produce spheroids of different sizes using the same initial cell suspension. She designed the single inlet multi-size spheroid (SIMSS) chip where conical structures of varying apex angles funnel cells into a pinhole (Figure C-1). Due to the varying funnel sizes, different numbers of cells sediment into each pinhole. This is called the enrichment factor, or how many times the funnel will multiply the number of cells in the pinhole compared to a pinhole with no funnel on top.
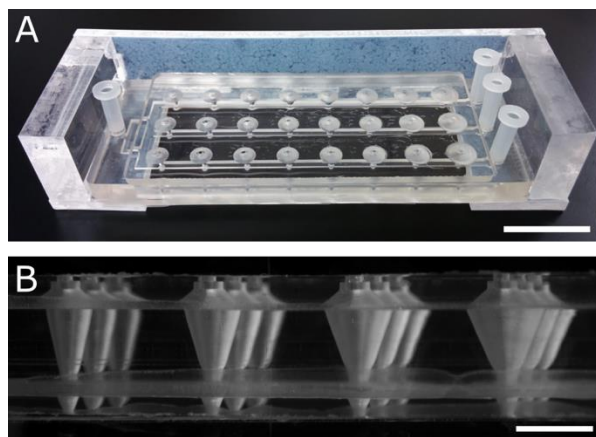

Figure C-1: Single inlet multi-size spheroid chip designed and fabricated by Mohana Marimuthu. A) Photograph of a 24 well-SIMSS chip. Scale bar = 2 cm. B) Side view of the four centre funnel structures with varying apex angles. Scale bar = 5 mm.

Photographs of OV90 (Figure C-2A) and TOV112D (Figure C-2B) spheroids show that the SIMSS chip can form spheroids of different sizes. The spheroid diameters were measured over three repetitions of the experiment and results are shown in Figure C-3. My role in this project was to identify a statistical test that can detect if the diameter increase as a function of enrichment factor is monotonic. The Mann-Kendall test [192], [193] is a non-parametric statistical test designed to detect a monotonic trend over time where the null hypothesis, H_0, is that no monotonic trend while the alternate hypothesis, H_A, is that the data contains a positive, a negative, or a non-null monotonic trend. However, only one data point per time period can be considered. The Mann-Kendall test

does not include the standard deviation of repeated measurements when determining the statistical significance of the trend detection.
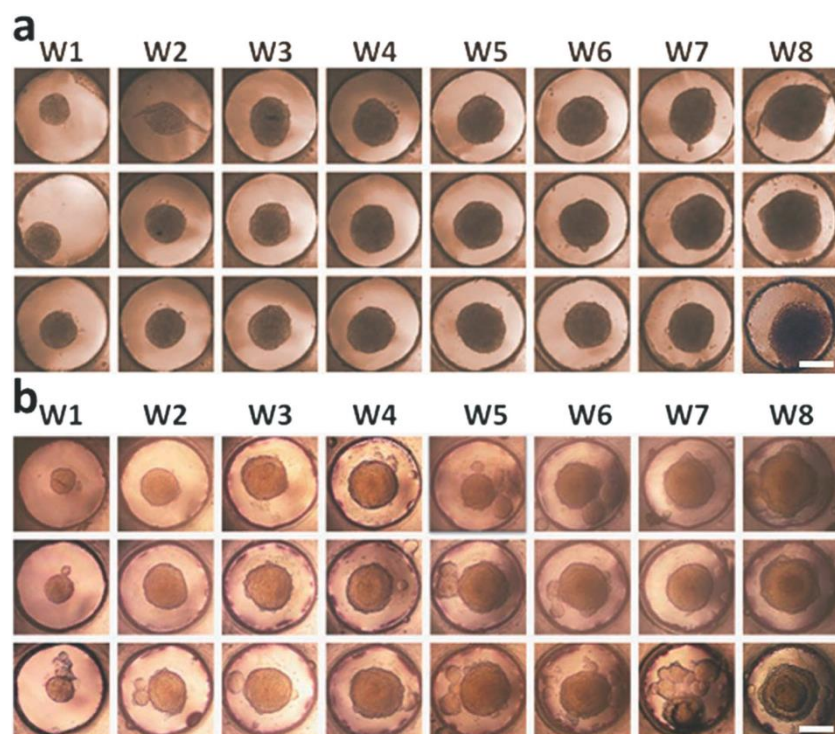

Figure C-2: Spheroid formation in a 24 well-SIMSS chip using OV90 (A) and TOV112D (B) ovarian cancer cell lines. Well 1 has an enrichment number of 7 and well 8, of 37. Reproduced from [78] with permission from The Royal Society of Chemistry.
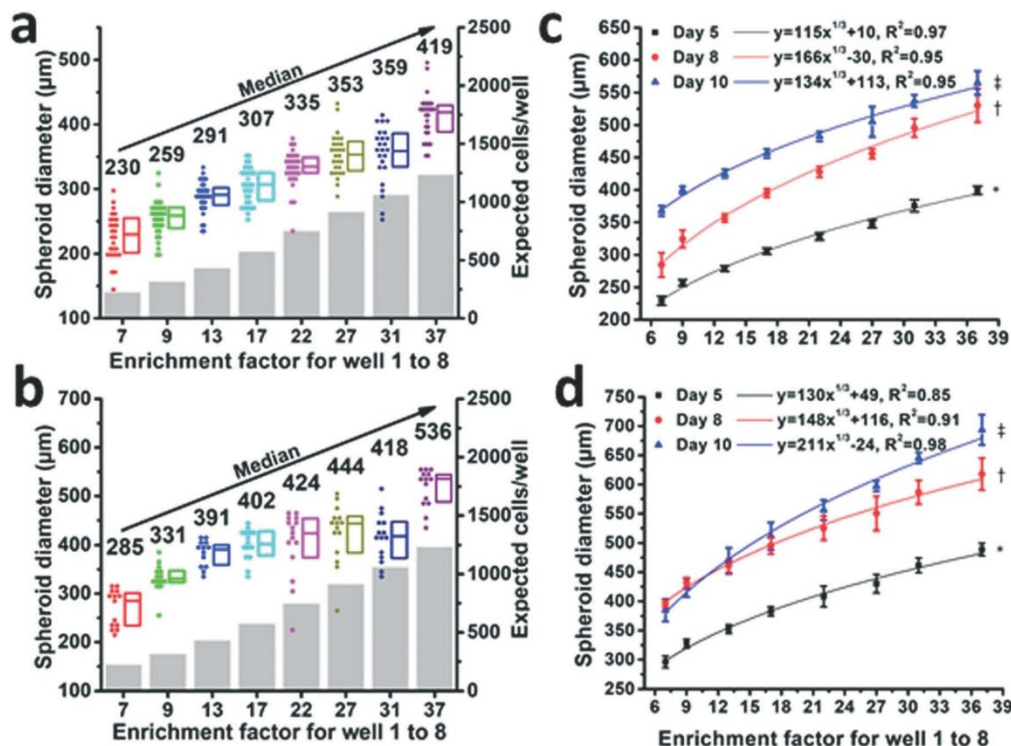
Figure C-3: Spheroid growth as a function of the initial enrichment factor. Box plot showing the spheroid diameter on day 5 for OV90 (A) and TOV112D (B). Grey bars represent the number of expected cells forming each spheroid due to the funnels. Spheroid diameter on day 5, 8 and 10 for OV90 (C) and TOV112D (D). Error bars represent the standard error of the mean. Paired two-tailed Student's t-tests between well 1 and 8: for (C) *p = 0.0002, †p = 0.0008, ‡p = 0.0002, and for (D) *p = 0.002, †p = 0.0008, ‡p = 0.0008. Reproduced from [78] with permission from The Royal Society of Chemistry.

I modified how the Mann-Kendall test is performed according to Soderberg and Hennet [161]. Their main approach was to create data scenarios based on the data points and their error bars. For each data points, a value was randomly selected in the range defined by the standard deviation around the average value according to a normal distribution. The standard Mann-Kendall test was then applied to this data point scenario and a *p-value* was calculated using the Matlab *ktaub* function [194]. This was then repeated multiple time to yield a distribution of p-values that can then be analyzed by observing what percentage of *p-values* are below 0.05 (% of significant *p-values*).

Table C-1 shows the optimization of the minimum number of scenarios to perform. The modified Mann-Kendall test was performed three times for each scenario number and the relative standard

122

deviation was calculated. From 10 to 5 000 scenarios, an improvement in the relative standard deviation can be seen, while minimal improvement is seen from 5 000 to 10 000, leading to the selection of 5 000 scenarios.

Table C-1: Number of scenarios optimization. Example using OV90 day 5 diameters

Number of randomized scenarios	% of significant *p*-values ($p < 0.05$)			Relative standard deviation (%)
	Run 1	Run 2	Run 3	
10	80.00	90.00	100.00	9.07
1 000	85.60	85.60	87.60	1.09
5 000	85.90	86.54	85.78	0.39
10 000	87.07	86.45	86.78	0.29

The modified Mann-Kendall test using 5 000 scenarios was applied to determine if both cell lines spheroid diameters presented a monotonic increase corresponding to the enrichment number and if that monotonic increase was present throughout their growth (day 5, 8, and 10 curves in Figure C-3C-D). The test yielded a p-value distribution for each day and cell line and the results are shown in Table C-2, where bold numbers indicate statistical significance. When the standard Mann-Kendall test is applied on average diameter, highly statistically significant p-values are found. However, when the standard deviation of each data point is considered, nuances can be made. For example, TOV112D spheroid diameters at day 5 are statistically significant (p = 0.002) when only the average diameter is tested. When 5 000 scenarios are tested, the median p-value is 0.035 and the average p-value of the resulting distribution is 0.060, which is not statistically significant. 63.8% of the scenarios' p-values are below 0.05. In this case, the modified Mann-Kendall test does not detect a monotonic trend. In summary, using the modified Mann-Kendall test, a monotonic trend is probable at days 5 and 8 (percentage of significant p-values is between 50% and 95%), and certain at day 10 (percentage of significant p-values above 95%). For both cell lines, spheroid growth in the first days seems to be more unpredictable and yield less monotonic trends according to the enrichment number while, as the spheroids grow, this trend stabilizes and becomes monotonic.

Table C-2: Modified Mann–Kendall test applied to OV90 and TOV112D spheroid diameters

		OV90			TOV112D		
		Day 5	Day 8	Day 10	Day 5	Day 8	Day 10
p-value using average diameter		**0.0002**	**0.0002**	**0.0002**	**0.002**	**0.0008**	**0.0008**
5 000 scenarios	Median *p*-value	**0.009**	**0.004**	**0.004**	**0.035**	**0.009**	**0.004**
	Average *p*-value	**0.026**	**0.014**	**0.006**	0.060	**0.028**	**0.006**
	% of significant *p*-values ($p < 0.05$)	86.5	94.2	**99.6**	63.8	83.4	**99.3**

APPENDIX D - DESCRIPTION OF THE MATLAB ALGORITHMS

This appendix describes the image analysis algorithm developed to analyze hyperspectral images of co-culture spheroids. The algorithms are designed to first performed the image analysis steps described in Figure 4-2 on the fluorescence and brightfield hyperspectral datacubes, namely, acquisition time and gain normalization, dark noise subtraction, shading correction, and ROI selections. A further step is performed on each fluorescence ROI quantify fluorescence, if wanted, and to spectrally unmix the various spectral entities. At the end of these steps, a formatted data .mat file is created for each sample, containing the evolution of the fluorescence of each individual spheroid over time. Other metrics such as the number of fluorescent pixels (or the spheroid area) are also saved in these files. A final Matlab script reads the individual .mat files corresponding to each analyzed sample, removes any empty well, calculates their fluorescence intensity averages and standard deviations, and interpret these results in graphs according to the studied conditions.

D.1 Matlab scripts and functions

The following section will detail the various Matlab scripts and functions that were developed and used throughout this dissertation.

D.1.1 Script SystemX.m

This Matlab script is designed to extract the fluorescence intensity of each of the 24 spheroids imaged in a single acquisition. "SystemX" refers to the name of the microfluidic chip studied. The script calls analysisFunction7.m, described in the next section, for each day of the experiment. One script must be run for each analyzed microfluidic chip.

D.1.2 Function analysisFunction7.m

The Matlab function analysisFunction7.m performs all the steps necessary to correct and quantify each spheroid fluorescence, as listed in Figure 4-2. After all steps are performed, the function saves a matrix in a .mat file with the fluorescence intensities over time of all 24 spheroids of one microfluidic chip.

D.1.3 Function CreateStackFromImages.m

The Labview program used to acquire the hyperspectral images produces one .tiff file per wavelength acquired. The images corresponding to one hyperspectral acquisition are placed in the

same folder. The function createStackFromImages.m automatically reads all images in each folder and sub-folder and create a 3D matrix corresponding to each acquired hyperspectral datacube. The matrix dimensions are *x* x *y* x wavelengths.

D.1.4 Function StackDarkNoiseRemoval.m

This function removes the dark noise from the brightfield and the fluorescence datacubes using the "Dark noise (fluorescence)" and the "Dark noise (brightfield)" acquisition describes in Table 4-1. The function also produces the graphs presented in Figure D-1. These graphs are used as check-points to verify that the acquired fluorescence and brightfield spectra are visually correct.
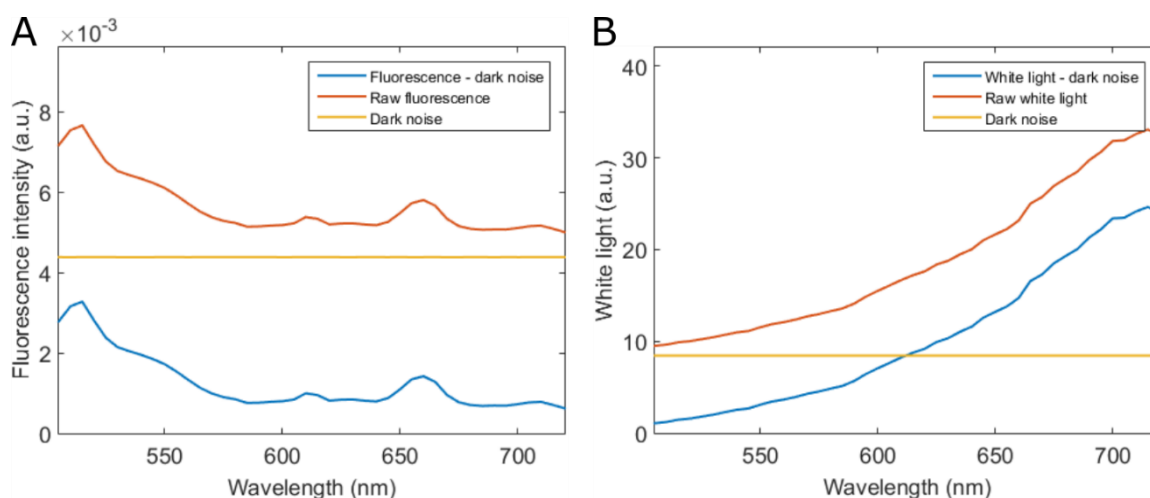

Figure D-1: Dark noise removal for fluorescence (A) and brightfield (B) images. Here, the average spectra of the pixels corresponding to one spheroid are represented.

D.1.5 Function UniformizeStack.m

The shading correction for fluorescence and brightfield datacubes is applied by the uniformizeStack.m function using the "Laser bleed-through" and the "System transmission" acquisitions of Table 4-1. Check-point figures of the shading correction are presented in Figure D-2.
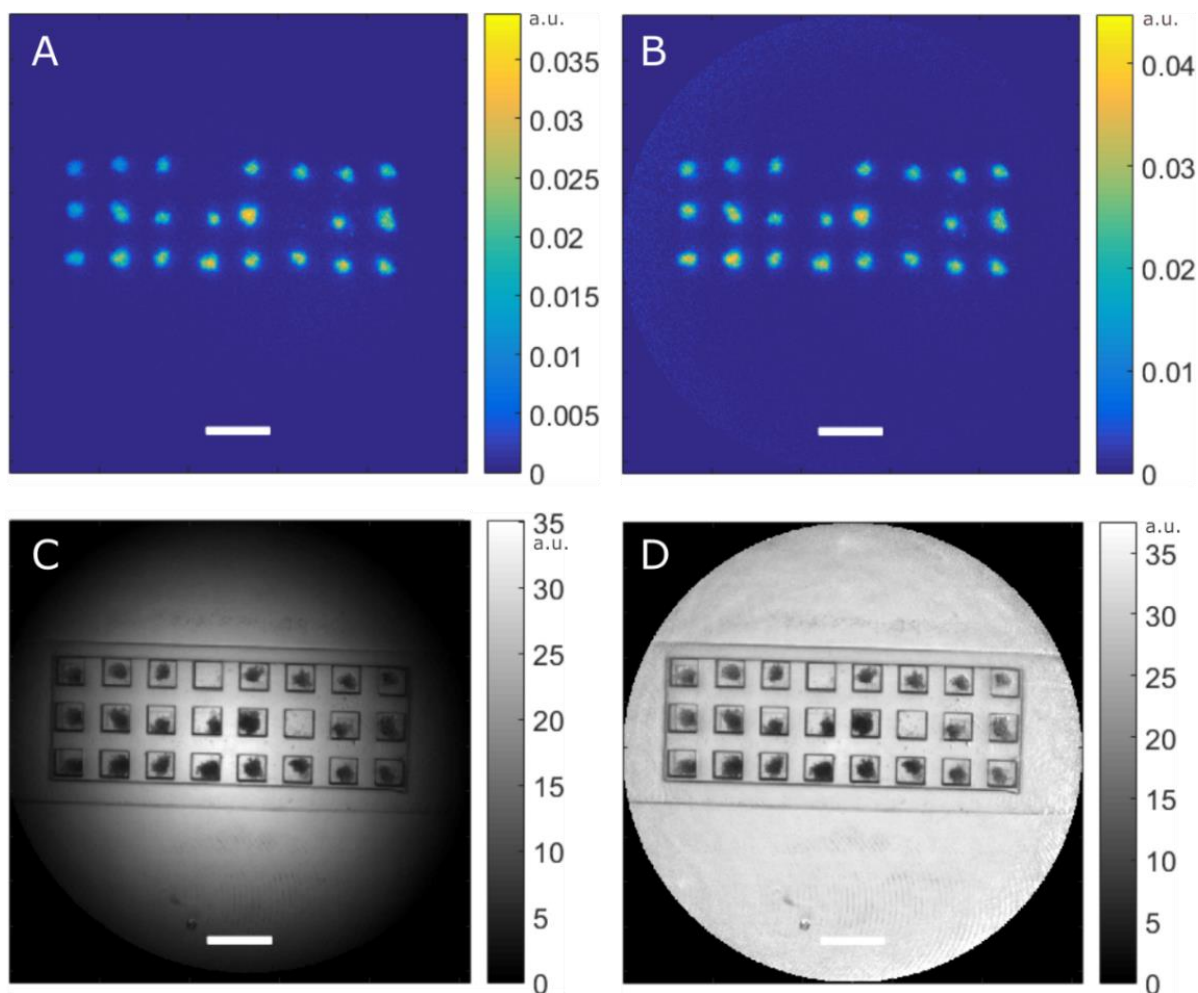
Figure D-2: Fluorescence images (at 515 nm) before (A) and after (B) shading correction. Brightfield images (at 720 nm) before (C) and after (D) shading correction. Scale bars = 1 mm.

D.1.6 Function automaticSaveWellImagesExtraction.m

To extract the fluorescence of each individual spheroid, regions of interest (ROI) corresponding to each spheroid needs to be determined. To do so, a semi-automatic image registration algorithm was implemented in function automaticSaveWellImagesExtraction.m. Briefly, brightfield images of each microfluidic chip, at each imaged day, are presented to the user side-by-side with a reference image of a microfluidic where well positions are known. The user then points four corresponding locations on each image and the algorithm calculates the geometric conversion to be applied to the sample image so that it superimposes the reference image.
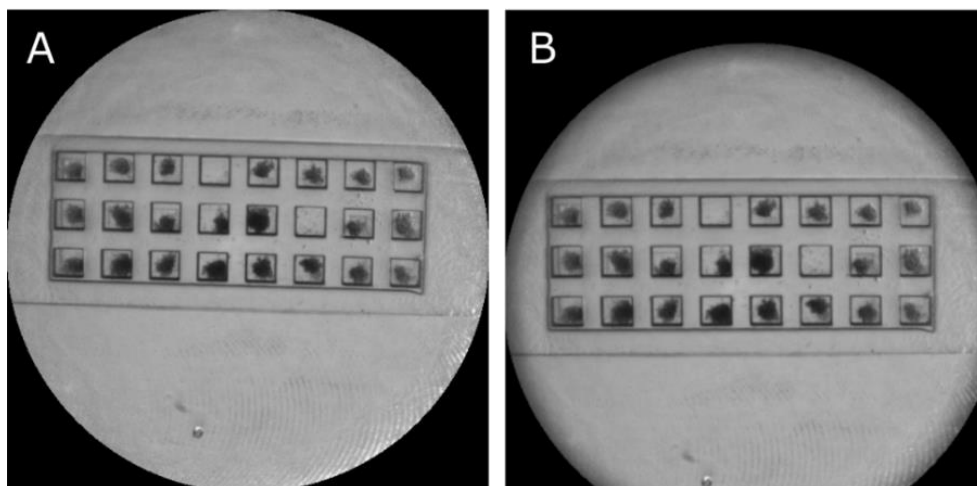
Figure D-3: Before (A) and after (B) the image registration.

D.1.7 Function spectralUnmixingParfor.m

For every ROI determined previously, the spectrum at each pixel is analyzed using a spectral unmixing algorithm implemented in the spectralUnmixingParfor.m function. The goal of the unmixing is to evaluate what and how many reference spectra are present in the measured fluorescence spectrum. The implemented unmixing is based on solving a non-negative linear least-square problem where the basis vectors are reference spectra of each spectral entity in the spheroid. The algorithm is designed to find the coefficients to multiply each basis vectors that best minimize the residuals between the experimental spectra and the calculated spectra. As the coefficients represent the number of times the basis vectors are included in the experiment spectra, they cannot be a negative value and are forced to be positive. The function output images corresponding to the calculated coefficient of each reference spectrum. Figure D-4 illustrate the spectral unmixing of eGFP (A) and mCherry (B) from the bleed-through. The normalized root mean square error is also calculated to evaluate the goodness of the fit. To optimize the computation time of this function, parallelization on multiple computer cores was implemented in the Matlab function, as each analyzed spectrum are independent.
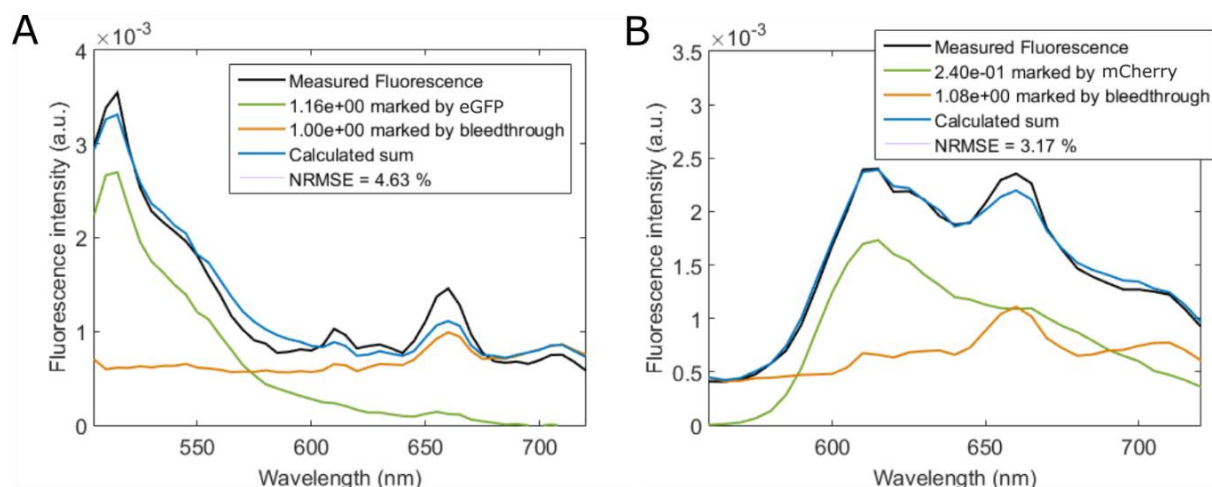
Figure D-4: Spectral unmixing of eGFP (A) and mCherry (B).

D.1.9 Function createMask.m

Once the regions of interest corresponding to each spheroid in the acquisition are calculated, the function createMask.m is used to perform an automatic thresholding based on Otsu's method [195] and calculate a mask where background pixels are forced to 0. This thresholding was performed on the x-*y* image of the summed fluorescence from 500 to 720 nm to improve accuracy. This mask is then applied to the resulting coefficient image obtained from function spectralUnmixingParfor.m to set the background pixels to zero. Finally, the total fluorescence intensity for that spheroid is calculated by summing this masked coefficient image.
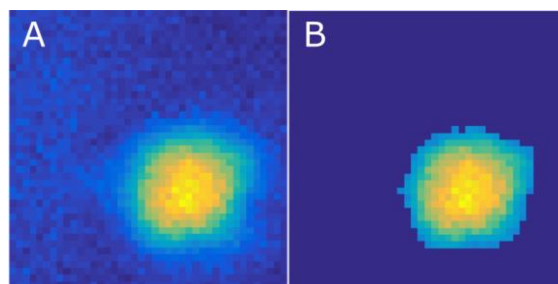

Figure D-5: Region of interest for one spheroid before (A) thresholding, and after (B).

D.1.10 Function graphFluorescence.m/graphSummedFluorescence.m

Two functions called graphFluorescence.m and graphSummedFluorescence.m are also used throughout the algorithm to create a figure containing the wanted fluorescence image, a scale bar and a colour scale. Figure D-6 shows an example figure representing the spheroid transmittance at 720 nm.
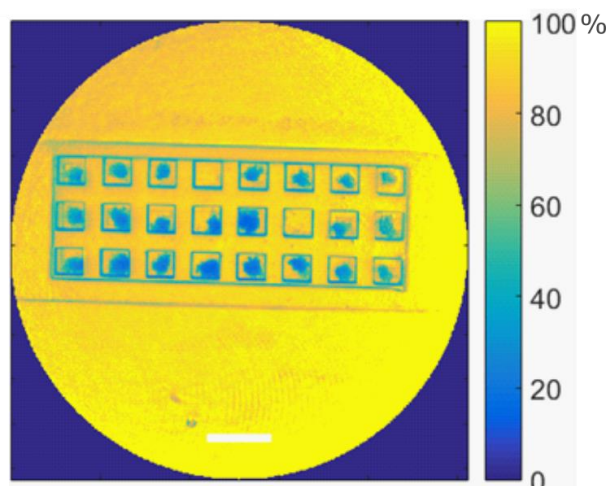
Figure D-6: Spheroid transmittance at 720 nm. Scale bar = 1 mm.

D.1.11 Function Interpretation.m

A final script is used to interpret the fluorescence intensity measurements of each sample according to their conditions, such as drug concentration and ratio of cell populations. The script can also calculate the standard error of the mean and represent it as a shaded area around the curves. Figure D-7 shows selected examples of the figures produced by this script.
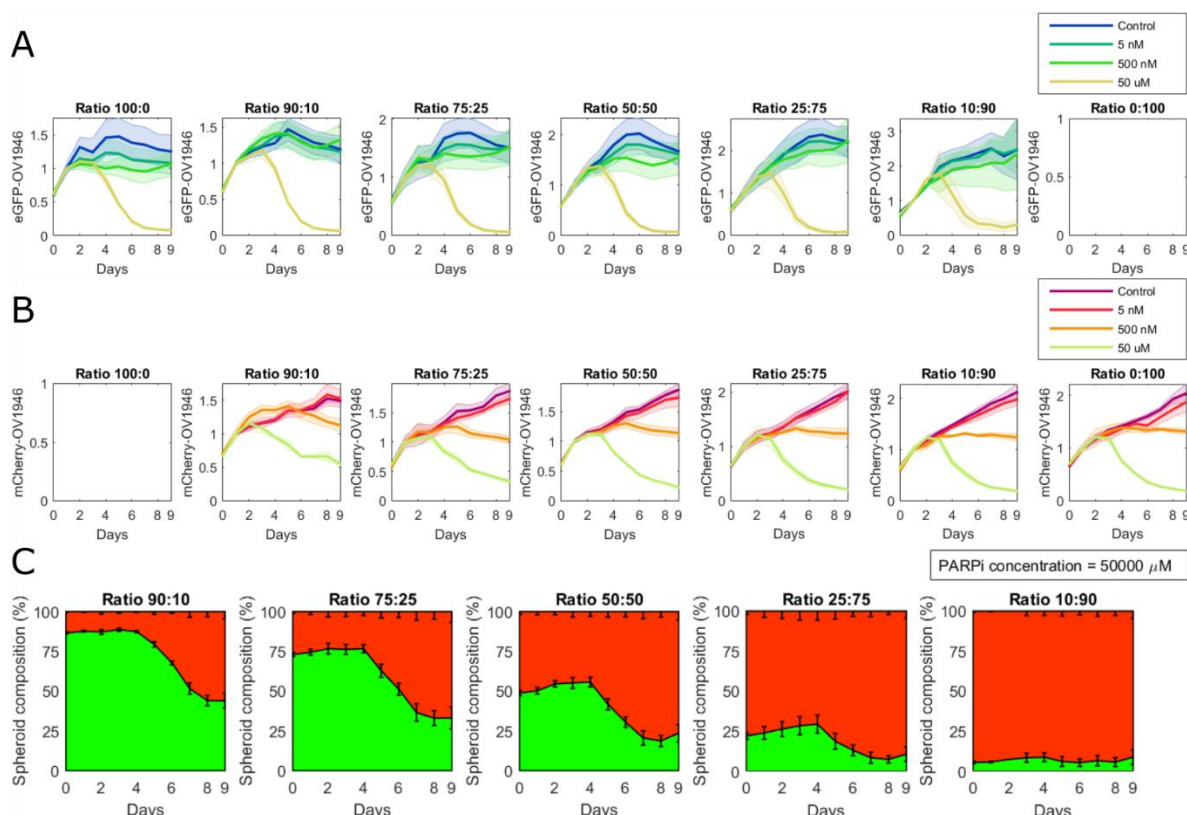
Figure D-7: Treatment response to talazoparib. A) eGFP fluorescence intensity over time as a function of talazoparib concentration. The different graphs show different initial cell seeding ratio. B) Similar graphs as in A) but following mCherry fluorescence over time. C) One example of the spheroid composition graphs produced by the script. Here, the evolution of the spheroid composition as a response to 50 nM of talazoparib is shown.

D.2 User interface overhaul

As a summer intern, Didier Black-Laflèche worked on a user interface to the Matlab algorithms, in order to facilitate their use by non-technical users. While the interface is not yet fully functional, some steps can be done, such as identifying the wells where spheroids were ejected and that should be removed from further analysis.
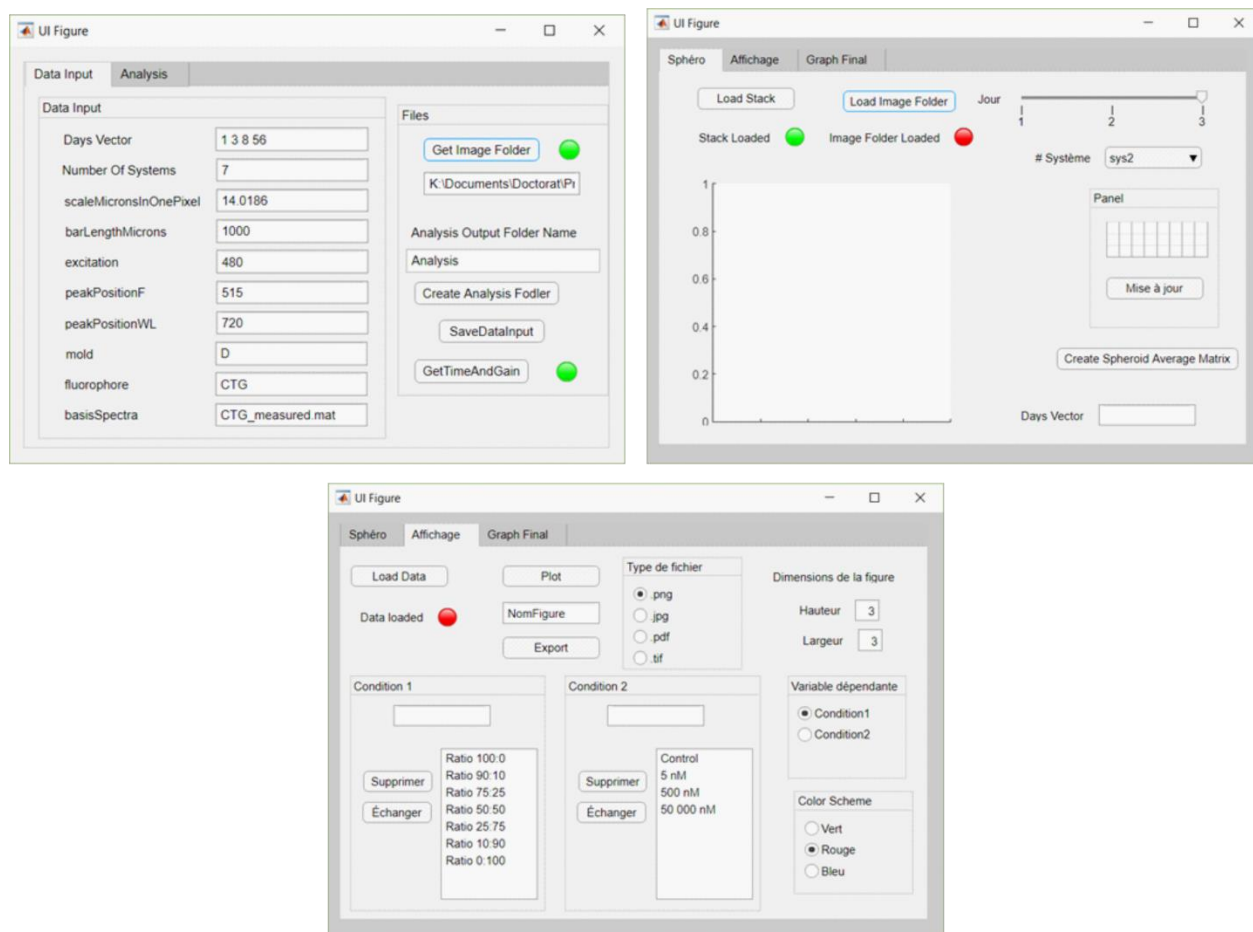
Figure D-8: Prototype of the new user interface to facilitate the analysis of complex hyperspectral imaging-based experiments.

APPENDIX E - LIST OF CONTRIBUTIONS

Articles

1. **A. St-Georges-Robillard**, M. Cahuzac, B. Péant, M. A. Lateef, H. Fleury, A. Ricard, A. Sauriol, F. Leblond, A.-M. Mes-Masson, & T. Gervais, "Long term fluorescence hyperspectral imaging of on-chip treated co-culture tumour spheroids to follow clonal evolution," submitted to *Integrative Biology,* 2018.

2. **A. St-Georges-Robillard**, M. Masse, M. Strupler, B. Patra, A. M. Orimoto, J. Kendall-Dupont, B. Péant, A.-M. Mes-Masson, F. Leblond, & T. Gervais, "Fluorescence hyperspectral imaging for live monitoring of multiple spheroids in microfluidic chips," *Analyst*, 143(16), 3829–3840, 2018.

3. M. Marimuthu, N. Rousset, **A. St-Georges-Robillard**, M. A. Lateef, M. Ferland, A.-M. Mes-Masson, & T. Gervais, "Multi-size spheroid formation using microfluidic funnels," *Lab on a chip*, 18, 304-314, 2018.

4. M. Astolfi, **A. St-Georges-Robillard**, F. Leblond, A.-M. Mes-Masson, & T. Gervais, "Microfluidics and spectroscopic imaging for personalized medicine in ovarian cancer," *popular science paper for SPIE Newsroom*, 1-3, 2016.

Oral presentations

1. **A. St-Georges-Robillard**, M. Masse, R. Guay-Lord, B. Patra, A. Orimoto, M. Strupler, A.-M. Mes-Masson, T. Gervais, & F. Leblond, "Chemoresistance assessment of ovarian cancer microtumors trapped in a microfluidic chip using a spectroscopic imaging system," *Photonics West*, San Francisco, 2017.

2. **A. St-Georges-Robillard**, M. Masse, M. Strupler, B. Patra, A. M. Orimoto, A.-M. Mes-Masson, F. Leblond, & T. Gervais, "Imagerie spectroscopique pour l'analyse de sphéroïdes fluorescents piégés dans une puce microfluidique," 2*6e Journée annuelle scientifique de l'Institut du cancer de Montréal,* Montréal, 2016.

Scientific posters

1. **A. St-Georges-Robillard**, M. Cahuzac, A. Sauriol, B. Péant, A.-M. Mes-Masson, F. Leblond, & T. Gervais, "Quantifying PARPi-resistant subpopulations after treatment in co-culture spheroids using hyperspectral imaging," *MicroTAS 2018,* Kaohsiung, Taiwan, 1439-1441 2018.

2. **A. St-Georges-Robillard**, M. Masse, B. Patra, A. M. Orimoto, M. Strupler, A.-M. Mes-Masson, F. Leblond, & T. Gervais, "Chemosensitivity analysis of co-culture tumor spheroids on-chip using hyperspectral fluorescence imaging," *Journée de l'innovation en génie physique*, Montréal, 2018.

3. **A. St-Georges-Robillard**, M. Masse, B. Patra, A. M. Orimoto, M. Strupler, A.-M. Mes-Masson, F. Leblond, & T. Gervais, "Chemosensitivity analysis of co-culture tumor spheroids on-chip using hyperspectral fluorescence imaging," *27e Journée annuelle scientifique de l'Institut du cancer de Montréal*, Montréal, 2018.

4. **A. St-Georges-Robillard**, M. Masse, B. Patra, A. M. Orimoto, M. Strupler, A.-M. Mes-Masson, F. Leblond, & T. Gervais, "Chemosensitivity analysis of co-culture tumor spheroids on-chip using hyperspectral fluorescence imaging," *MicroTAS 2017*, Savannah, 545-546, 2017.

5. **A. St-Georges-Robillard**, M. Masse, J. Kendall-Dupont, M. Strupler, B. Patra, M. Jermyn, A.-M. Mes-Masson, F. Leblond, & T. Gervais, "Système d'imagerie spectroscopique pour évaluer la viabilité de microtumeurs piégées dans un système microfluidique," *18e congrès des étudiants du CRCHUM*, Montréal, 2016.

6. **A. St-Georges-Robillard**, M. Masse, J. Kendall-Dupont, M. Strupler, B. Patra, M. Jermyn, A.-M. Mes-Masson, F. Leblond, & T. Gervais, "Spectroscopic imaging system for high-throughput viability assessment of ovarian spheroids or microdissected tumor tissues (MDTs) in a microfluidic chip," *Photonics West*, San Francisco, 2016.

7. **A. St-Georges-Robillard**, M. Masse, J. Kendall-Dupont, M. Strupler, B. Patra, M. Jermyn, A.-M. Mes-Masson, F. Leblond, & T. Gervais, "Spectroscopic Imaging System for High-Throughput Viability Assessment of Ovarian Microtumors in a Microfluidic System," *Forum MEDTEQ*, Montréal, 2015.

8. S. Bolduc-Beaudoin, M. Leroux, J. Brodeur, **A. St-Georges-Robillard**, A.-M. Mes-Masson, F. Leblond, & T. Gervais, "Bio-micro-opto-mechanical system for ovarian cancer spheroids analysis," *ISS CREATE*, 2013.

Indexed conference proceedings

1. **A. St-Georges-Robillard**, M. Masse, J. Kendall-Dupont, M. Strupler, B. Patra, M. Jermyn, A.-M. Mes-Masson, F. Leblond, & T. Gervais, "Spectroscopic imaging system for high-throughput viability assessment of ovarian spheroids or microdissected tumor tissues (MDTs) in a microfluidic chip," *Proceedings of SPIE; Photonic Therapeutics and Diagnostics XII*, 9689, 96894E, 2016.